Channeling effect in the CsI(Tl) used for a WIMP search

Ju-hee Lee

Under the supervision of
Professor Sun Kee Kim

A dissertation submitted to the Graduate Faculty of
Seoul National University in partial fulfillment of
the requirements for the degree of Doctor of Philosophy

Department of Physics and Astronomy
The Graduate School of Natural Sciences
Seoul National University
Seoul, KOREA

August, 2012

Abstract

The KIMS collaboration published a recent measurement of the WIMP-nucleon scattering with 27287.9 kg·days data. For further increases in the detector sensitivity, we study possible channeling effects in the crystal detector which are relevant to the various ions' ranges according to initial propagation directions in the crystal, and result in the modulation of light yields in the detector. From the simulation, we find that $\sim 3\%$ of all recoil ions in isotropic motions have ranges and light yields larger than those in amorphous CsI crystals. We measure this effect with a setup, that is composed of a neutron generator, six neutron detectors, and a well characterized CsI(Tl) detector. By comparing the light yields of recoil ions moving along a symmetry axis, [110], with that from recoils moving along a random direction, we find a clue for the blocking effect which are expected to result in less light yields. Though this measurement can not determine the pulse shapes of the channeling events due to the small statistics, with a hypothesis that these events are similar to random nuclear recoil events, we reanalyze the KIMS data and conclude that the channeling effect has the effect of increasing detection sensitivity by $50 \sim 0$ % for nuclear recoils from WIMPs with masses of $20 \sim 50\mathrm{GeV/c^2}$.

Keywords: Channeling effect, CsI(Tl) , Dark Matter, KIMS, Pulse shape discrimination, Scintillation, Quenching, WIMPs

Student Number: **2006-30772**

Contents

List of Figures

List of Tables

1 Introduction

1.1 Dark Matter

1.1.1 What is Dark Matter(DM) and WIMPs?

The existence of Dark Matter (DM) was first predicted by F. Zwicky in 1933 [7]. He measured the average velocity of the Coma cluster and those of its eight member nebulae by their redshifts and found that the velocity dispersions are larger than that which can be estimated by the mass and distance from the luminosity of the cluster. According to the Virial theorem, there had to be 400 times more mass in the cluster to explain the velocity dispersion. So he postulated the presence of dark matter which is not seen has gravitational effects on the motion of the luminous matter. A few years later, in 1937, V. C. Rubin *et al.* measured the rotational velocity distribution in a spiral galaxy, M31 or the Andromeda Galaxy, with the precise measurements of H_{II} regions at sixty-seven different positions from 3 to 24 kpc from its core [8]. They assumed a disk model based on their measurement that the maximum of mass density is inside the disk except the core, and above that it is slowly decreasing as shown Fig. 1.1. In 1990, K. G. Begeman *et al.* [9] tested two kinds of models to explain the measured rotation curves of ten galaxies, one is a three parameter dark halo model composed of a gas, a luminous matter and a dark halo and the other is the modified Newtonian dynamics(MOND) of one parameter M/L, the ratio of mass and luminosity, with a fluctuating distance within the observation error. Both of the models explain the measurement well as shown Fig. 1.2. However, M. J. Jee *et al.* [10] found that when they reconstruct the mass structure from strong and weak lensing effects on the galaxy in Fig. 1.3, inside the Cl 0024 + 17, there is a substructure of mass

which is inferred to be dark matter. And they describe that the morphology of that structure cannot be traced to the intracluster medium, thereby the MOND, but by the collision of two massive core composed of two clusters with noninteracting particles along the line of sight and then, by the radially expansion and deceleration of particles. Recently, there is another work to reconstruct the mass structure by weak lensing for two merging clusters, the so-called bullet clusters, for which direction is perpendicular to the line of sight [11], When they overlap the X-ray images around them, the centroids of mass are not on the hot region, but behind them. This is also evidence for dark matter.

Among the candidates for dark matter, Weakly Interacting Massive Particles(WIMPs) are the best motivated one. According to the supersymmetry extension of the standard model, WIMP is the lightest supersymmetry particle called the neutralino [12][13]. Since it is massive due to the superposition of supersymmetry partners of the photon, Z^0 and higgs, named photino, Zino, and higgsino, thereby nonrelativistic, and its annihilation cross-section is on the weak scale, it explains the relic density of dark matter, which is estimated to be 0.22 when the total density of Universe is 1 by WMAP [14]. In the next section, we will discuss how to detect WIMPs and current experiments attempting to do it.

1.1.2 Direct detection of WIMPs

A WIMP can be detected if it interacts with ordinary nuclei in the detector material and the material emits the absorbed energy by ionization, scintillation or phonon. The differential event rate of the WIMP–nucleus scattering for a target mass and a recoil energy is represented as [15]:

$$\frac{dR}{dE_R} = \frac{R_0}{E_0 r}\frac{k_0}{k}\frac{1}{2\pi v_0^2}\int_{v_{min}}^{v_{max}}\frac{1}{v}f(v, v_E)d^3v, \tag{1.1}$$

where E_R is a recoil energy which is transferred from WIMP to a nucleus; E_0 is the WIMP average kinetic energy, $\frac{1}{2}M_D v_0^2$; M_D is a WIMP mass; v_0 is the WIMP average velocity; v_{max} and v_{min} represents each the velocity of escaping

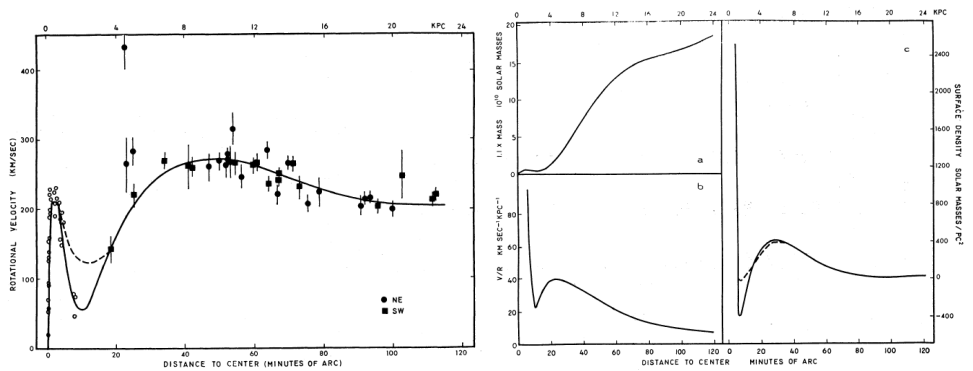

Figure 1.1: The rotational velocity measurement in M31 and the estimation of its mass distribution(c on the right figure) [8].

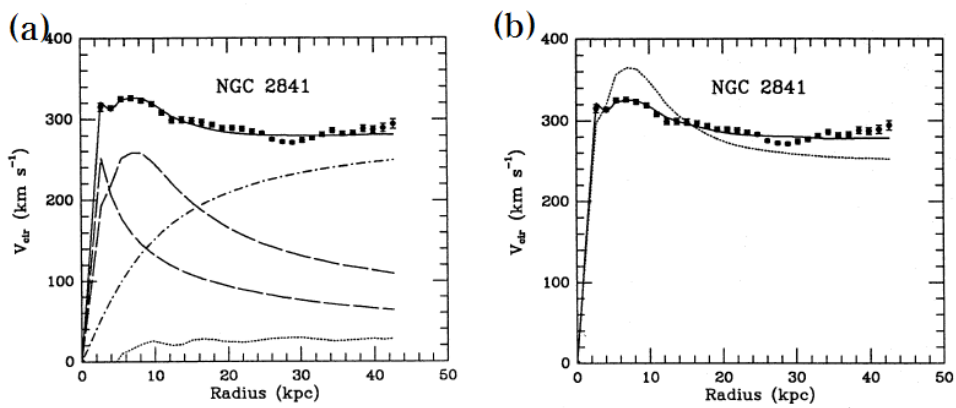

Figure 1.2: The rotation velocity curve of NGC2841 and two fitting models of the dark halo and the MOND [9]. The solid curves are the fitting function. For (a), the dashed lines are the visible components, the dotted line is the gas component and the dotted-dashed line is the dark halo. For (b), the dotted line is the one parameter M/L fit.

WIMP, v_{esc}, and Earth, v_E; $f(v, v_E)$ is the velocity distribution function of WIMP, $exp^{-(v-v_E)^2/v_0^2}$; k is the integral of $f(v, v_E)$ for d^3v and k_0 is k for the case that $v_{max} = \infty$; and R_0 is represented in the unit of tru or $kg^{-1}day^{-1}$ as

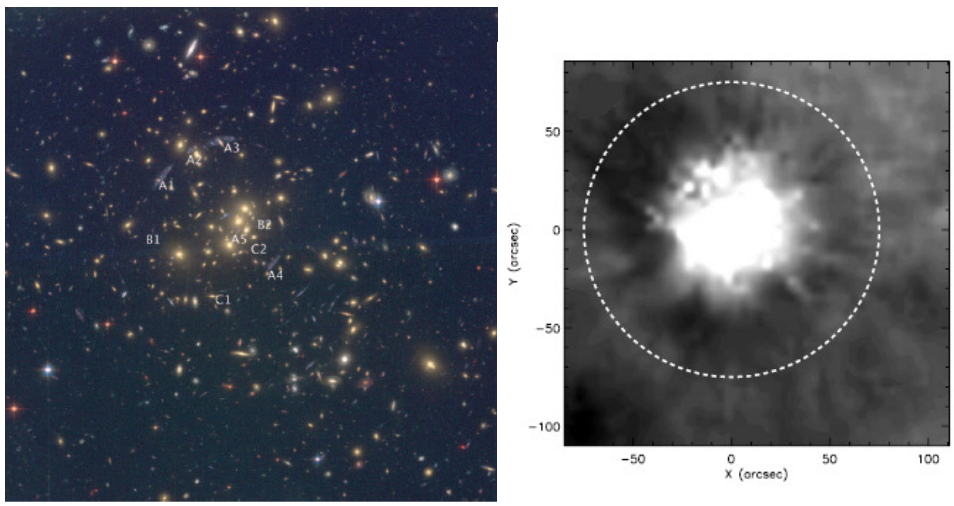

Figure 1.3: Cl 0024 + 17 cluster (left) and Its mass reconstruction (right). In the left figure, A1 $\sim$ A5 are the images which are originated from one source and created by the strong(multiple images) and weak(elliptical shape) lensings. B1-2 and C1-2 are also same images. In the right figure, the white dashed line represents the dark matter substructure [10].

follows :

$$\frac{540}{AM_D}(\frac{\sigma_0}{1\ pb})(\frac{\rho_D}{0.4\ GeVc^{-2}cm^{-3}})(\frac{v_0}{230kms^{-1}})\ kg^{-1}d^{-1}, \tag{1.2}$$

where A is the target atomic mass in AMU; M_T is the mass of a target nucleus; σ_0 is the WIMP-nucleus cross-section at zero momentum transfer; ρ_D is the WIMP average density. From the integral of Eq. 1.1, we get

$$\frac{dR(v_E, v_{esc})}{dE_R} = \frac{k_0}{k_1}[\frac{dR(v_E,\infty)}{dE_R} - \frac{R_0}{E_0 r}exp^{-v_{esc}^2/v_0^2}]\ keV^{-1}kg^{-1}d^{-1}, \tag{1.3}$$

where k_1 is k for the case that $|v + v_E| = v_{esc}$ and for practical purposes, the first term in the right side is approximated as:

$$\frac{dR(v_E,\infty)}{dE_R} = c1\frac{R_0}{E_0 r}exp^{-c_2 E_R/E_0 r}, \tag{1.4}$$

where c_1 and c_2 are fit parameters, usually 0.751 and 0.561 respectively. From Eq. 1.3, we can estimate the recoil energy spectrum for WIMPs of a given mass

with considering only elastic scattering at the zero momentum transfer in unit of dru or $keV^{-1}kg^{-1}d^{-1}$, however, in order to obtain the realistic one, we add a factor of a square of the form factor, $F^2(qr_n)$, where q is the transferred momentum to a nucleus and r_n is the effective nuclear radius. The detail expression can be found in [15]. By applying the quenching factor, which will be explained in section 1.4.3, and the energy resolution of the detector, we can reproduce the expected measured energy spectrum for WIMP-nucleus scattering. By converting σ_0 to Eq. 1.5 and comparing the expected events with data in the unit of dru for an energy bin, we get the WIMP-proton cross-section for one species in the material. In this case, the spin independent elastic scattering, the cross-section for a proton and a neutron are same. And then through the summation as Eq. 1.6 for all species, we get the WIMP-proton cross-section, σ_p, in the detector.

$$\sigma_0 \;=\; \frac{\mu_n^2}{\mu_p^2} A^2 \sigma_p \; f_n, \tag{1.5}$$

where μ_n and μ_p is each the reduced mass for a nucleus and a proton about a WIMP mass, $\frac{M_D m_n}{(M_D+m_n)}$ and $\frac{M_D m_p}{(M_D+m_p)}$, and f_n is the mass fraction of one species nucleus in the material.

$$\frac{1}{\sigma_p} \;=\; \sum_n \frac{1}{\sigma_{p,n}} \tag{1.6}$$

There are many WIMP search groups as Table 1.1. They are located in deep underground laboratories to avoid the cosmic ray background and set enough shielding materials to surround their detectors to reduce the external backgrounds from rocks and the air. After appropriate event selection cuts, they obtain the number of events that can be originated from WIMP-nucleus scattering. As shown in Table 1.1, the current results are not consistent. It is explained that since they are using different materials and experimental setups for the WIMP search, the mass and state of WIMPs which they are intend to search are different. Figure 1.4 shows the current results of the regions that some experiments exclude for the WIMP–nucleon cross-section

of the spin independent scattering and that some experiments found for the WIMP signatures(closed circles). DAMA/LIBRA and CoGeNT argue that their observed events are modulating with the period of one year, and these are originated from the flux modulation of WIMPs due to the Earth revolution around the Sun. In the dark halo model, the WIMPs distribute around the cluster with being stationary, however, since our galaxy moves around the centroid of the cluster, the Sun around our galaxy and the Earth around the Sun, WIMPs move to the Earth relatively. Some researchers expect the diurnal modulation of WIMPs due to the Earth rotation [16][17]. XENON100, CDMS II and EDELWEISS II observed several events in the nuclear recoil region, but due to the nonnegligible backgrounds, they cannot confirm that they observed WIMPs signatures or not. Due to enough signal events, CRESST II also can test the annual modulation.

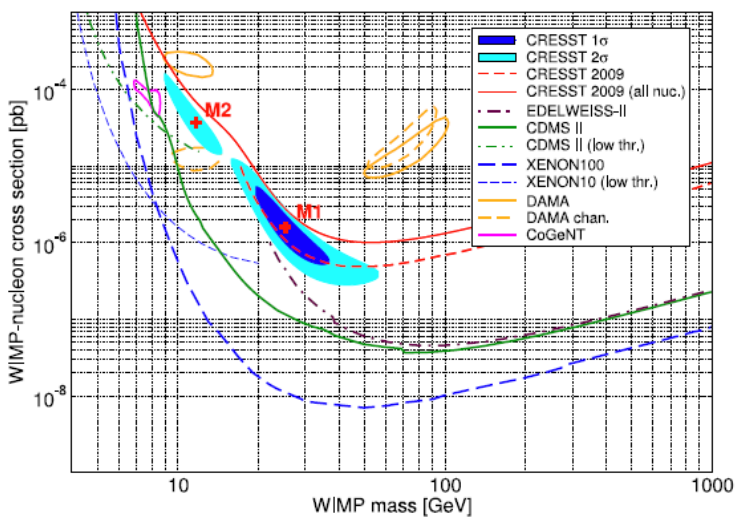

Figure 1.4: The WIMP search results concentrating on the experiment to argue that they observed the evidence of WIMPs [23].

Table 1.1: Direct detection experiments for WIMP[a]

Exp.	Target	Detection	The latest results	E^b_{window}
XENON100	two phase Xe	Ionization	3[c]	8.4
[18]	62 kg	+ scintillation	in signal region	∼44.6 keVnr
CDMS II	Ge 230g*19	Ionization	2[d]	10
[19]	Si 105g*11	+ Phonon	in signal region	∼ 100 keVnr
DAMA/LIBRA[e]	Na, I	Scintillation	0.0116 ± 0.0013	2
[20]	9.7kg * 25		annual modulation	∼ 6 keVee
CoGeNT	Ge	Ionization	16.6 ± 3.8 %	0.5
[21]	440 g		annual modulation	∼ 3 keVee
EDELWEISS II	Ge	Ionizatoin	5[f]	20
[22]	400 g *10	+ Phonon	in signal region	∼ 200 keVnr
CRESST II	Ca, W, O	Scintillation	67	12
[23]	300 g * 8	+ Phonon	w/ some BG[g]	∼ 40 keVnr

[a] KIMS will be introduced in the next section.

[b] E_{window} means the energy window for WIMP search.

[c] The expected background(BG) rate is 1.8 ± 0.6, so the probability for 3 to be WIMP events is 28 %.

[d] The expected background rate is 0.9 ± 0.2, so the probability for BG to access two events is 23 %.

[e] For the accumulated events with DAMA/NaI.

[f] with three events of background.

[g] Background sources are e/γ leakage and events from alpha, neutron and recoiling nuclei from alpha decay. But they are not enough for 67 events.

1.2 KIMS experiment

The Korea Invisible Mass Search(KIMS) collaboration is searching for evidence of WIMPs at Yang Yang Laboratory(Y2L) in Kangwon province in South Korea. It is located in a deep underground cavern that was donated

by the YangYang Pumped Storage Power Plant of Korea Midland Power Co. in order to attenuate cosmic ray, especially muon, backgrounds. The muon flux in Y2L is $2.7 \times 10^{-7}/\mathrm{cm}^2/\mathrm{s}$, which is measured by the liquid scintillator detector that surrounds the shielding box of the CsI(Tl) detector. The KIMS collaboration is composed of five universities in Korea: Seoul National Univ., Kyungpook National Univ., Sejong Univ., Ewha womans Univ. and Yonsei Univ, plus two groups in China: Tsinghua Univ. and the Institute of High Energy Physics(IHEP). The experiment was started in late 1997 [12] with the carrying out of a feasibility test for the energy threshold and the pulse shape discrimination(PSD) of a CsI(Tl) crystal as a WIMPs detector. Results were reported at the 1998 International Conference on High Energy Physics(ICHEP98) [24][25]. Since 2000, we had been selected as a creative research center from the Creative Research Promotion Project implemented jointly by the Ministry of Education, Science and Technology (MEST) and the National Research Foundation of Korea (NRF). We performed the first complete WIMP search over the next six years [12], with results published in the journal of Physics Letter B in 2006 [26]. During the time, the KIMS team concentrated on the identification of the internal background sources[27][28], the purification of the powder of CsI to reduce ^{134}Cs and ^{137}Cs contamination [29][30] and the recrystallization [28],ultimately achieving a count rate of $\sim$5.5 /keV/kg/day in CsI(Tl) crystals which is acceptable for a rare event detector. A stringent limit on the cross-section between WIMPs and nuclei, that rejects a possible region of WIMP parameter that was favored by another group, DAMA [31], was published in Physical Review Letter, in 2007 [32] based on results from four low-background crystals. Since 2008, using funds from the World Class University (WCU) project of MEST and NRF, a larger group was formed that brings together particle and nuclear experiments and has the name of Q2C, Quark to Cosmos. This group, composed of 7 professors, 7 associate researchers, 4 staffs and 26 graduate students, is performing a variety of experiments including: a WIMP dark matter search with CsI(Tl) crystals; a neutrinoless double beta decay search with $CaMoO_4$ crystals; studies of

rare decays of B-mesons, charm mesons and tau leptons; strangeness nuclear physics; and studies of dense nuclear matter and the nucleosynthesis of heavy elements [33]. Members of the Q2C team have many collaborations and discussions with foreign researchers from China, Japan, USA, Ukraine, Germany etc. Recently we published results that have better sensitivity, a 10 times larger data exposure, and an improved analysis [13]. We are currently analyzing our data to see whether or not WIMPs signals with an annual modulation are present [34], using the method to study the WIMP-nucleon interaction signal reported by the DAMA collaboration. This section presents the current results and the future plan.

1.2.1 Current results of WIMPs detection

The recent KIMS result is based on a 32793 kg·days data exposure that was accumulated between Sep. 2009 and Aug. 2010 with a 12 CsI(Tl) crystal array, each with mass 8.7 kg. During this time, we monitored the stability of all environmental conditions: the temperature; the humidity; the electric power; and the data acquisition rate on-line. Once each week, a collaborator performs a shift that includes an overall system check. The crystal array is surrounded by a four-layer shield, comprised of 30 cm of mineral oil, 15 cm of lead, 5 cm of polyethylene(PE) and 10 cm of Oxygen Free High Conductivity(OFHC) copper (from outside to inside) as depicted in Fig. 1.5. The layer thicknesses were optimized using a simulation for the effective reduction of external backgrounds.

In order to prevent contamination from ^{222}Rn , decays of which can increase the external backgrounds of our detector, the setup is continuously purged with N_2 gas. The radon contamination measurements in the air inside the Y2L experimental chamber was measured to be 1.2 ± 0.49 pCi/l, which is lower than that at other dark matter experiments [35]. The mineral oil shield contains liquid paraffin with 5 % pseudocumene, and is read out with Photo-Multiplier Tubes(PMTs) for monitoring muons. Due to the large proportion of protons in its material, it is also a neutron shielding material. The

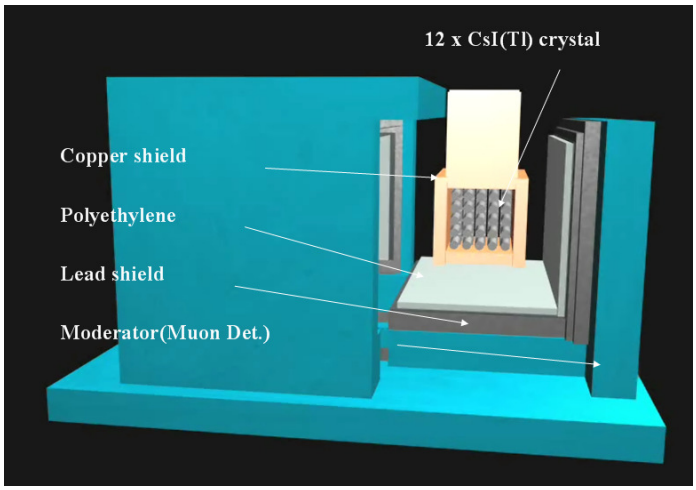

Figure 1.5: Scheme of the shielding structure of KIMS detector. Since 2008, we have had 12 crystals inside the copper box. Outside of the copper box, two neutron monitoring detectors are placed.

measured rate of external γ-rays inside the shielding setup measured with a 100 % High-Purity Germanium(HPGe) detector is negligible compared to the internal background rate of $\sim$5.5 /keV/kg/day. The γ reduction effectiveness of the shielding materials is illustrated in Fig. 1.6.

In the empty space between the copper box and the PE shield, there are two neutron monitoring detectors made of $\sim$1 l BC501A, which, with the application of the pulse shape discrimination, can select neutron-induced scintillation events. These have been used for data-taking since July 2004. From the analysis of data for one of the detectors taken between July and October 2004, a measured rate of 33.65 counts/l/day and a total of 2272 neutrons and a rate of 8611 counts/l/day of gammas were determined. However, due to similar shapes of neutron and alpha induced signals, we checked their times for correlations between neutron-neutron events and gamma-neutron events. Time correlations are indications of life times of α-α and β-α decays in ^{238}U or ^{232}Th decay chains shown in Fig. 1.7. Y. F. Zhu *et al.* [36] reports the measured intrinsic radiopurity levels of ^{235}U,U and ^{232}Th in the CsI(Tl) crystal

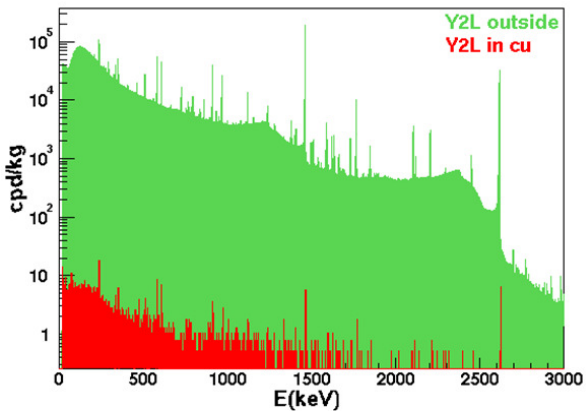

Figure 1.6: The measured value of γ backgrounds at Y2L by using the HPGe detector. The top histogram is obtained inside Y2L without any shielding materials, and the bottom with the full shielding setup.

detectors, based on the analysis of such time correlations. These levels are also inferred from a secular equilibrium study, in which the contamination is determined from the estimated levels of the long-lived ^{226}Ra and ^{228}Th parents in the decay chains. Using these methods, we could attribute the number of neutron-tagged events that are due to alphas in the ^{238}U and ^{232}Th decay chains to be 2823±137, and conclude the neutron flux inside of the shield is -1.25±1.82 neutrons/l/day, and consistent with zero. In addition, we measured the flux of muon-induced neutrons inside the shielding setup using coincidences between neutron monitoring detectors and the muon monitoring detectors, and the value was 0.0035 counts/keV/kg/day. Therefore, the nuclear recoil backgrounds that could produce misleading WIMP signals is negligible with our shielding setup [12].

However, during actual data taking with CsI(Tl) crystals, each with a PMT at each end, the most serious backgrounds that are observed are caused by surface alpha decays and PMT noise. Surface Alpha(SA) signals are decays produced by ^{210}Po contamination on the crystal surface decays into ^{206}Pb by emitting an alpha. ^{210}Po is one of the progenies of ^{222}Rn . ^{222}Rn exists in the

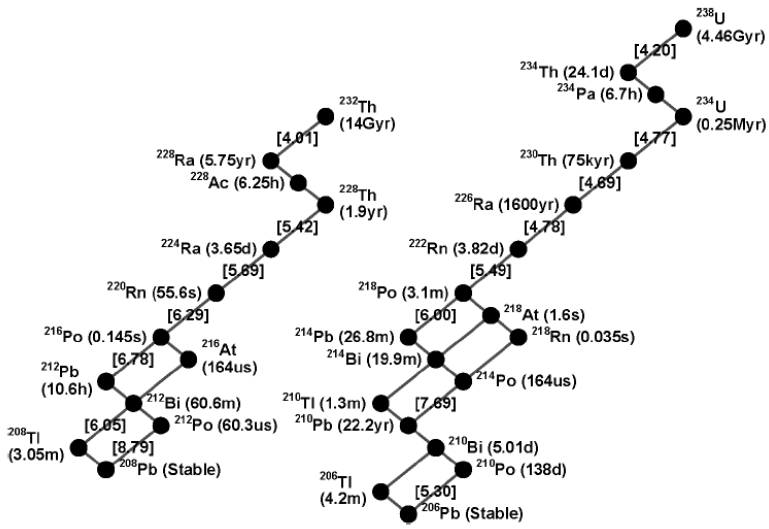

Figure 1.7: ^{232}Th (left) and ^{238}U (right) decay chains.

air and produces surface contaminated CsI(Tl) by the adsorption of ^{218}Po , which is a reactive metal element produced in ^{222}Rn decay. After several α and β-decays, ^{210}Po is formed as depicted in Fig. 1.7. ^{210}Po decays in which only the recoiling ^{206}Pb daughter is seen in the crystal produce fast, low-energy signals that are a troublesome background. A dedicated experiment using alpha-coincidence detections between a ^{222}Rn contaminated and a clean CsI(Tl) crystal was used to characterize SA signals [37]. These signals have very fast scintillation-decay time, and survive the application of all event selection cuts of KIMS except PSD. Figure 1.8 shows the different PSDs for SA, neutron scattering, and gamma scattering events. Here LMT10 means Log Mean Time within 10 μs after a trigger signal in the data-taking time window, which is used for PSD in the KIMS experiment. From this study, we infer that when a ^{210}Po undergoes an α-decay, the signals with lower LMT10 than those for neutron scattering events are produced. This information is used to fit the LMT10 data for each measured energy bin with Gaussian distributions using three components: the PSDs for SA, neutron and gamma induced events.

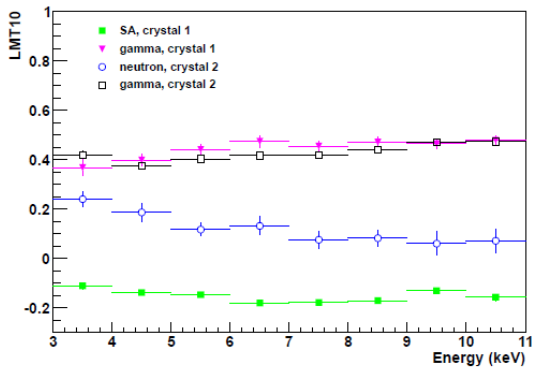

Figure 1.8: Pulse shape discrimination values(LMT10) for the interested recoil energy region. These are peak positions of each LMT10 distribution at each measured energy bin for SA, neutron scattering, and gamma scattering events. Crystal 1 was used for the SA study and crystal 2 was used for neutron scattering experiment [37].

From this analysis, we can statistically separate SA and gamma induced events from nuclear recoil events, which are the conjectured WIMP signatures.

The photomultiplier tubes(PMTs) also produce significant signal-like noises during the Data AcQuisition(DAQ). The main sources are the spontaneous emission of electrons from the photo-cathode, residual ions inside the glass vacuum tube, and Cherenkov radiation or scintillation in the window glass. The last source is studied by introducing a ^{90}Sr radioactive β source and measuring coincident signals from the two PMTs, both of which face each other. These signals have different characteristics from normal signals that are induced by scintillations in the CsI(Tl) crystal. We study PMT noise signals produced by a PMT-dummy-crystal setup located inside the shield in Y2L, that is comprised of two PMTs on opposite ends of an empty acryl box that is wrapped in a teflon sheet, with comparing them to neutron induced signals and multiple-hit gamma signals, which occur mostly by Compton scattering. The PMT noise signals can be distinguished statistically using variables (1)

through (4) listed in Table 1.2. In the table, pmt00 and pmt01 designate the PMTs of the detector number 0, qc is the charge sum of whole clusters in an event, and qc1 and qc10 is the charge sum for the first 1μs and 10μs after the first cluster appears, respectively, where cluster means a discriminated signal produced by a photo-electron. After applying PMT noise cuts, the remaining background level was 0.005 counts/day/kg/keV in the 3 keV bin in the measured energy spectrum, which is negligible compared with the rates from other backgrounds, and the reduction efficiency in the neutron calibration data in that bin, considering all of the cuts in the table, range from 0.207 to 0.399 for all detectors [13]. Since an acceptable cut is one that rejects a large fraction of background events than signal events, these cuts are efficient. In addition to PMT noise cuts, a Fit Quality cut is applied for high-energy tail events, which follow a high energy signals for some time and for which clusters are evenly distributed across the DAQ time window. This variable is obtained from a maximum likelihood fit to the signal shape using an exponential decay function. Tail events have bad fit qualities. This cut is important in our channeling experiment as is explained in detail in section. 3.3.

The Bayesian Analysis Toolkits (BAT) [38] was used to find the most probable ratio of nuclear recoil events in KIMS data after all the event selection was applied. In order to apply BAT, we need the maximum likelihood(L) probability density function(PDF) with certain parameters for each event category: surface alphas, gammas and WIMPs. These are obtained from the maximum likelihood fits to each control sample events separately. We use an asymmetry Gaussian function PDF given by:

$$\begin{aligned} PDF(x) \;=\; & \frac{1}{1/2(\sigma_L+\sigma_R)} e^{\frac{1}{2}(\frac{x-m}{\sigma_L})^2}, x \;<\; m \\ & \frac{1}{1/2(\sigma_L+\sigma_R)} e^{\frac{1}{2}(\frac{x-m}{\sigma_R})^2}, x \;\geq\; m. \end{aligned} \tag{1.7}$$

The parameters of m, σ_L and σ_R are determined from fits from using Roofit package in ROOT [39]. Equation 1.7 gives the log-likelihood function used for obtaining the event fractions of $f_{NR,i}$ and $f_{SA,i}$ that are induced by nuclear

Table 1.2: Event selection cuts[a]

	Name	Example
(1)	Biggest cluster cut	$\frac{pmt00.qc}{pmt00.bclust} > 3$ && $\frac{pmt01.qc}{pmt01.bclust} > 3$
(2)	Charge asymmetry cut	(pmt00.qc - pmt01.qc) $> C_1^a$ && (pmt01.qc - pmt00.qc) $> C_2^a$
(3)	Start time difference cut	– 0.3 μs < pmt00.t0 - pmt01.t0 < 0.3 μs
(4)	Short tail rejection cut	$\frac{pmt00.qc - pmt00.qc10}{pmt00.qc} > 0.0002$
(5)	Fit Quality(FQ) cut	FQ < 2.5
(6)	Muon coincidence cut	the elapsed time since the coincidence > 50 ms
(7)	The qc1ovqc cut	$\frac{pmt00.qc1}{pmt00.qc}$ >0.25
(8)	Second time(t1) cut	det0.t1 > 2.5
(9)	Single hit cut	Only 1 detector has the signal.

[a] When all cuts are satisfied, an event is accepted as a candidate of nuclear recoils. After these cut, PSD cut is applied to discriminate events as SA, neutron and gamma induced ones. [b]C_1 and C_2 are characteristic values of each PMT, which are due to its electric gain and quantum efficiency.

recoils and surface alphas and determined by minimizing the expression. We assume that the last event category arises only from electron recoils(ER).

$$F = \sum_{k=1}^{n} -Log(f_{NR,i}PDF_{NR,i}(x_k) + f_{SA,i}PDF_{SA,i}(x_k) + (1 - f_{NR} - f_{SA,i})PDF_{ER,i}(x_k)) \quad (1.8)$$

Figure 1.9 shows an example of a two dimensional plot of $f_{NR,i}$ and $f_{SA,i}$ and a fit function with most probable parameters obtained by BAT [40]. From this, we obtain the most probable value(mode) and the confidence levels, and finally, we adjust those values by the cut efficiency to recover the measured event rates. In order to estimate the WIMP-nucleon cross-section, we compare the event rates of simulated with an assumption of 1 pb of the cross-section and measured with the 90 % confidence level. The reason that we use the confidence level is due to near-zero rate of the nuclear recoil events in each

energy bin. Figure 1.10 shows the recent KIMS result that was published on the Physical Review Letter in April, 2012. The sensitivity of this recent KIMS experiment increased by about one order-of-magnitude with 10 times more data than that used for the 2007 published results; now KIMS is the most sensitive experiments for the detection of spin-dependent WIMP-nucleus scatterings. Since it is largely comprised of iodine, KIMS excludes 0.02 CPD amplitude of annual modulation of DAMA, which uses the same detector by setting up an upper limit of 0.01 CPD for nuclear recoils in the same recoil energy region of iodine. KIMS continues to provide important and unique constraints to the search for WIMPs.

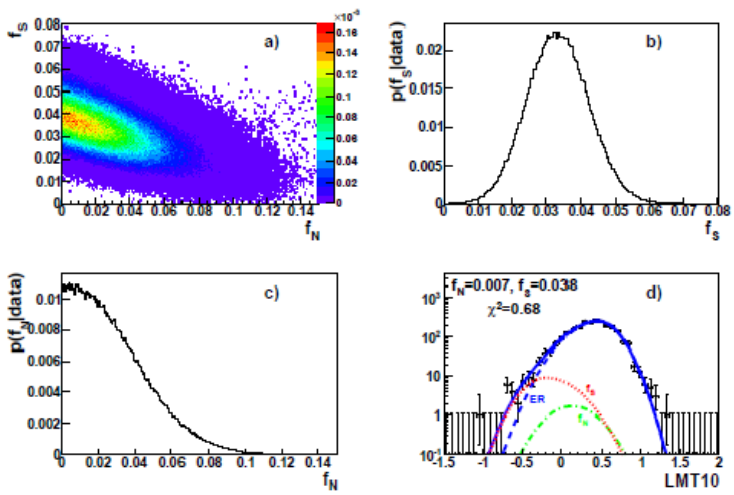

Figure 1.9: a) 2D plot for f_N and f_S, which are event fractions of nuclear recoils and surface alphas. b) The probability function of f_S. c) the probability function of f_N. d) The fit function with KIMS data at 6 keV bin. [40]

1.2.2 Future plan

KIMS has an upgrade plan. In order to reduce the average background level from 3 CPD to 1 CPD, we will change the current glass PMTs to the improved ones with high quantum efficiency and low radioactive backgrounds due to

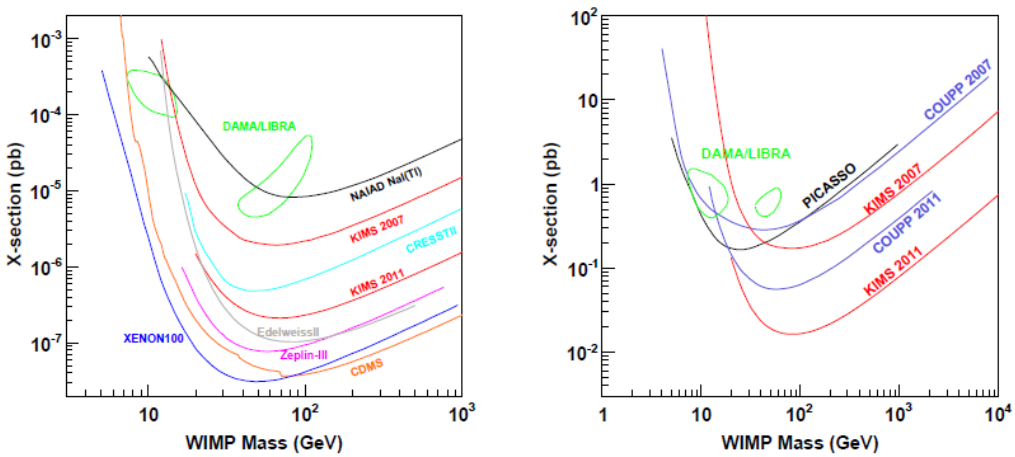

Figure 1.10: Spin independent cross-section limit (left) Spin dependent cross-section limit (right) of WIMP and a nucleon [40]

their metal bodies. We continue to study the surface alpha contamination in order to understand their origins and learn how to remove them, because these are a primary background source. Study with GEANT4 [41] simulations of radioactive contaminations in the KIMS experimental setup will identify the dominant sources contributing to the low energy region and give a better understanding of the source correlating with the surface alpha events [42]. The improved determinations of contaminations from the U_Th chains in t he KIMS detectors, not only with the assumption of secular equilibrium but also with individual fits for each nuclides will also give information on how the radioactive contaminations contribute to the low energy bins and how they might be removed from the detectors [43]. With this upgrade, we will have improved sensitivity and with another two years of data taking, be able to confirm or deny the annual modulation claim by DAMA. The first result will be published in this year [34].

1.3 Channeling effect

The theme of this study, the channeling effect, has been studied and measured since 1933 and very actively in the 1960s and 1970s [1]. The channeling effect is characterized as the maximum range, the maximum scintillation/ionization yield and the minimum scattering yield of incident ions in a monocrystalline target, when the ions move through the empty space between symmetry axes or planes. Ions in a target material transfer their energies to the target nuclei by the screened Coulomb interaction and to the electrons around those nuclei by the plasma-electron and the core electron-electron interactions. For the channeling case, ions usually lose their energies by the latter interactions, so the stopping power, the energy lose per a unit depth, drastically decreases and thereby the ion range increases. This effect has been applied for the crystallography, ion implantation, measurement of the lattice disorder, production of the polarized beam and measurement of nuclear life times [1]. In the production of polarized beams, positive charged particles, which enter an electron donor material with directions aligned along a symmetry plane of the material and being influenced a vertical magnetic field, each obtain an electron and go through the material with helps of the channeling effect. In this experiment, it was found that the escaping neutral particle by the channeling has a high probability to capture a electron of certain spin in the magnetic field and thereby can be polarized. For the measurement of the nuclear life time, particles are implanted in the target material to be a compound nucleus, and a decaying particle or the fission fragments from the compound nucleus is measured with a detector aligned parallel to the symmetry plane. The life time of the decay or fission which can be measured is in the range of $10^{-18} \sim 10^{-17}$. The scheme of this experiment is depicted in Fig. 1.11. In this experiment, the decaying particles or the fragments undergo large angle scatterings if they are next to target atoms, so can not be detected. But when they are generated after the compound nuclei go to some distance from their lattices, they undergo the weaker scattering yields and are detected more by the channeling effect. The

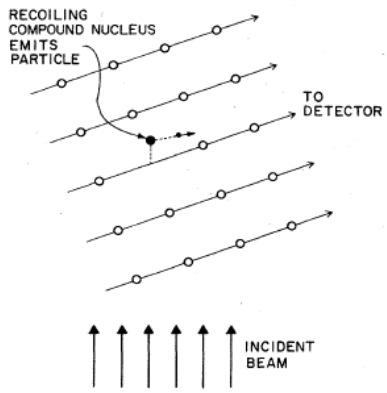

Figure 1.11: Illustration of the measurement of the short nuclear life time by using blocking effect [1]

effect that this experiment are using is referred to as the blocking effect. The blocking effect is that ions which start to move from their lattice sites undergo large angle scatterings when their directions are along the symmetry axis or plane. However, above some distance from the lattice, they can be channeled like incident ions mentioned above. In other words, the channeling effect is reduced by the blocking effect for recoil ions. The blocking effect is a main issue, together with the channeling effect, in this study, because the goal of this study is to measure the channeling effect of recoil ions in CsI(Tl) induced by neutrons or WIMPs, which is extricable with the blocking effect. The next section, we will present the principle of the channeling effect and the previous work of the estimation of the channeling fraction in CsI(Tl) .

1.3.1 Principle of the channeling effect [1]

An ion entering a monocrystalline target along the direction of a symmetry axis or plane of the crystal experiences a screened Coulomb potential, of which formula for a target is in Eq. 1.9.

$$V(r) \;=\; \frac{Z_1 Z_2 e^2}{r}\phi(r/a), \tag{1.9}$$

where Z_1 and Z_2 are atomic numbers of a projectile ion and a target atom; e is the charge of an electron,; r is the distance between them; ϕ is the screening function; a is the screening length to play a role to determine how large the potential affect to a projectile ion effectively. For ϕ, there were many functions proposed by theorists, for example, Lindhard used the form $\phi(r/a) = 1 - [1 + (\sqrt{3}a/r)^2]^{1/2}$. Among the many functions, one, which is obtained empirically by comparing the measured stopping powers and used in SRIM, is well matched with the measurements [3]. a is also represented with different formulae, and $a_{TF} = 0.4685(Z_1^{1/2} + Z_2^{1/2})^{-2/3}$ and $a_u = 0.4685/(Z_1^{0.23} + Z_2^{0.23})$ are frequently used among them. For a string of atomic arrays or a two dimensional atomic plane of ions to be channeled as shown Fig. 1.12, the screened Coulomb potentials are represented as Eq. 1.11.

$$V_{RS}(\rho) = \frac{1}{d}\int_{-\infty}^{\infty} V[(\rho^2 + x^2)^{1/2}]dx = (2Z_1Z_2e^2/d)f_{RS}(\rho/a)$$
$$= E\psi_1^2 f_{RS}(\rho/a) \; for\; a\; static\; row \quad (1.10)$$

$$V_{PS}(\rho) = n\int_0^{\infty} 2\pi R\; dR\; V[(\rho^2 + R^2)^{1/2}] = 2\pi n Z_1 Z_2 e^2 a f_{PS}(\rho/a)$$
$$= E\psi_a^2 f_{PS}(\rho/a) \; for\; a\; static\; plane, \quad (1.11)$$

where d is the atomic distance in an array; $f_{RS\ or PS}$ comes from the integral of $V(\rho)$ for each target atom; n is the areal density of atoms in a plane; E is the kinetic energy of a projectile ion; ψ is the characteristic angle which is relevant for the channeling criteria. Lindhard found the high energy condition, ψ_1, and low energy condition, ψ_2, for the axial channeling as follows:

$$\psi < \psi_1 = (2Z_1Z_2e^2/dE)^{1/2} \quad (1.12)$$

$$\psi < \psi_2 = [Ca\psi_1/(d\sqrt{2})]^{1/2}, \quad (1.13)$$

where C is a constant, usually is set to be $\sqrt{3}$. For the planar channeling, the characteristic angles are

$$\psi < \psi_a = (2\pi n Z_1 Z_2 e^2 a/E)^{1/2} \quad (1.14)$$

$$\psi < \psi_{a2} = a\sqrt{n}(Z_1Z_2e^2/Ea)^{1/3}. \text{ [5]} \quad (1.15)$$

With considering whole atoms in a target material and the temperature effect (non-static atoms), the half angle of each axial and planar channeling for the high energy condition are written as follows:

$$\psi_{1/2} = 0.8F_{RS}(1.2u_1/a)\psi_1 deg. \quad (1.16)$$

$$\psi_{1/2a} = 0.72F_{PS}(1.6u_1/a, d_p/a)\psi_a deg., \quad (1.17)$$

where $F_{RS\ or\ PS}$ represents the funcion from the integral for whole atoms; u_1 is the thermal vibration amplitude [1]. In summary, ions entering a monocrystalline target from outside should have a moving direction which makes an angle with a symmetry axis or plane less than the half angle will be channeled.

For the estimation of the blocking effect, the half angles can be applied to estimate whether the recoil ion is channeled or not, and simultaneously the thermal vibration amplitude and the critical distance should be considered. In next section, the critical distance is explained in detail. Fig. 1.13 shows an illustration of the channeling trajectories for an ion from outside and a recoil ion. An ion from outside can be channeled if the closest distance to a symmetry axis or a plane, which is calculated by Eq. 1.18, is larger than the critical distance, which has the same meaning to the statement with comparing of the moving angle and the half angle. However, a recoil ion should be apart from a critical distance and have an angle under the half angle to be channeled. Otherwise, it would be in blocking or random scattering. Here, the critical distances for an ion from outside and a recoil ion are different, because at the position with the critical distance, an ion from outside has zero kinetic energy, while a recoil ion has the minimum kinetic energy. Fig. 1.14 depicts schemes of experimental setups for the channeling and blocking effect. The difference between them depends on which direction the symmetry axis or plane of a target is aligned, an ion beam or a detector. Fig. 1.15 shows the results for two effects. The reason that at zero degree alignment the scattering yields are minimum is that for the channeling setup, ion beams penetrate through the channel and for the blocking setup, ions undergo the close encounter, which

means large angle scatterings, and are scattered to other directions.

$$1 - (b/\rho)^2 - V_{RS\ or PS}/(E\psi^2) = 0 \tag{1.18}$$

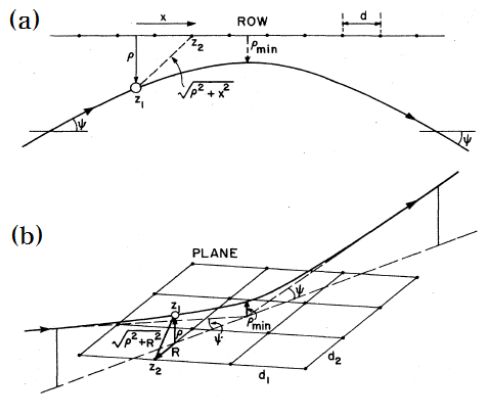

Figure 1.12: Ion trajectories in an static atomic array (a) and a static atomic plane (b) [1]

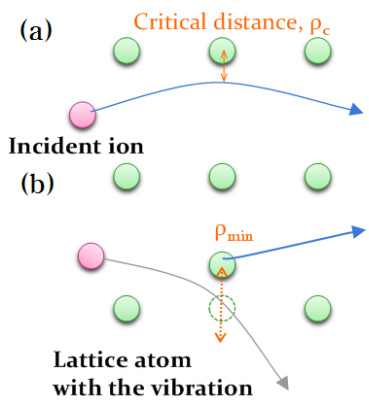

Figure 1.13: Illustration of trajectories for the channeling ions from outside (a) and from a lattice site (b)

1.3.2 Channeling fraction of CsI(Tl) [2]

DAMA suggested a method to estimate the channeling fraction for a recoil ion in the crystal [5], however, in their calculation, the blocking effect was

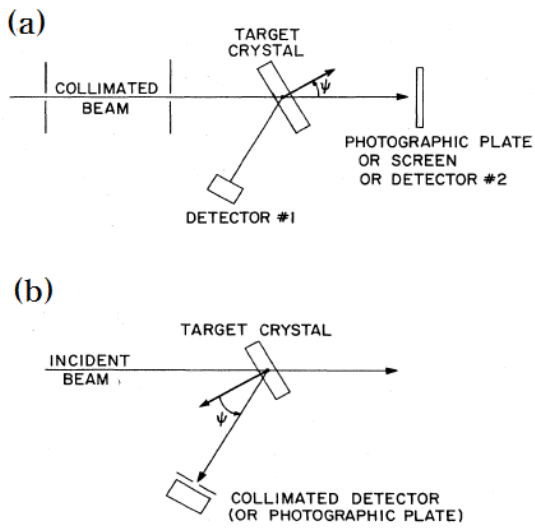

Figure 1.14: Scheme of the channeling (a) and blocking (b) experimental setup [1]

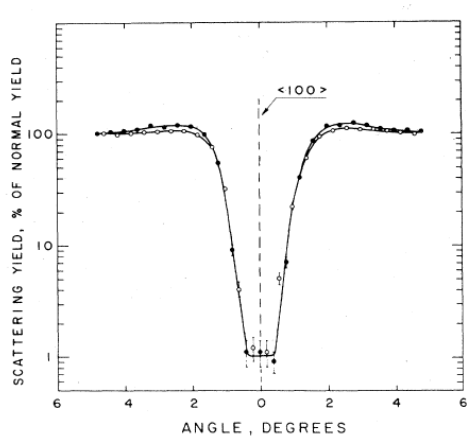

Figure 1.15: Comparison of the channeling effect and the blocking effect [1]

not included. N. Bozorgnia *et al.* [44][2] estimated the channeling fraction in NaI(Tl) , CsI(Tl) , Ge and Si detectors from an analytical calculation that considers blocking and thermal effects. They used Lindhard's screened Coulomb potential, mentioned in section 1.3.1, but in an averaged form for all atoms of a string, $U_a(\rho) = E\psi_1^2 \frac{1}{2} ln(\frac{C^2a^2}{\rho^2} + 1)$, and a plane, $U_p(\rho) = E\psi_a^2 [(\frac{x^2}{a^2} + C^2)^{1/2} - \frac{x}{a}]$. For the determination of the channeling criteria, they assumed a continuum model with the conservation of the transverse kinetic energy of an ion undergoing successive deflections in the symmetry axis or plane as Eq. 1.19

$$E_\perp = U(\rho_{min}) = E(\psi)^2 + U(d_{ch}/2), \tag{1.19}$$

where $E_\perp$ is the initial transverse kinetic energy of an ion; ρ_{min} is the closest approach distance in a collision between an ion and a target atom, which is calculated by Eq. 1.18; d_{ch} is the half width between symmetry axes or planes. In Eq. 1.19, the ions are assumed to be injected from outside and started to move at the center position between the symmetry axes or planes inside a crystal. These ions can be channeled if their closest approach distances are larger than the critical distance, and the blocking effect is not needed to be considered in this case. For the calculation of the critical distance they used the Lindhard's argument that when Eq. 1.20 is satisfied, Eq. 1.19 is conserved.

$$U'' < \frac{8}{d^2}E, \tag{1.20}$$

where U'' is the second derivative of the averaged screened potential and d is the interatomic spacing. When the inequality is changed into an equality, the critical distance can be derived from the above equation. However, there are also thermal effects. They included a thermal vibration term at the critical distance, ρ_c as Eq. 1.21

$$\rho_c(T) = \sqrt{\rho_c^2 + [c_1 u_1(T)]^2}, \tag{1.21}$$

where $u_1(T)$ is the one dimensional rms vibration amplitude, which is perpendicular to a symmetry axis or plane and determined by the Debye temperature,

the recoil atom mass, and the temperature,T; c_1 is a constant which can be from 1 to 2. For planar channeling, they substituted a plane with a fictitious string and used similar equations of axial channeling case. And with Eq. 1.22 including thermal effect and the second one of Eq. 1.13, the channeling criteria is

$$\psi \ < \psi_c(E) \ = \ \sqrt{\frac{U(\rho_c(E)) - U(d_{ch}/2)}{E}}. \tag{1.22}$$

The channeling fraction in the case of incident ions is obtained by the integral of the channeling probabilities, 0 for $\phi > \psi_c$ or 1 for $\phi <= \psi_c$, for all isotropic directions. By the way, a recoil ion which was scattered by a particle with a mass has some different relation for the transverse energy conservation, expressed in Eq. 1.23, because its initial position is not a center of an open space made of symmetry axes or plane, but around a lattice site. The former ion must arrive at the center again after the scattering but, the scattering position varies according to the incident angle. The latter ion starts from a lattice position, and the arrival position is varied according to the initial moving angle :

$$Esin^2\phi + U(\rho_i + d\ tan\phi) \ = \ U(\rho_{min}) < U(\rho_c(E)). \tag{1.23}$$

From this equation, one can calculate the minimum initial distance of the recoiling lattice ion with changing the inequality to the equality. After applying the distance to the integral of Eq. 1.25 to obtain the channeling probability for a (E, ϕ), summing for all symmetry axes or planes of interest as Eq. 1.26, and performing an integral of the probability for all isotropic directions as Eq. 1.27, the channeling fraction for recoil ions in a crystal is obtained. Please refer to [44] for the detail description.

$$\chi_{axial}(E, \phi) \ = \ \int_{\rho_{i,min}}^{\infty} d\rho g(\rho) \tag{1.24}$$

$$\chi_{planar}(E, \phi) \ = \ \int_{x_{i,min}}^{\infty} 2g(x)dx, \tag{1.25}$$

where g is a two dimensional vibration probability function for the axial channeling, $\frac{\rho}{u_1^2 exp(\rho^2/2u_1^2)}$, or a one dimensional vibration probability function for

the planar channeling, $(2\pi u_1^2)^{-1/2} exp(-x^2/2u_1^2)$.

$$\chi_{rec}(E,\phi) \;=\; P(A_1 or A_2 or ... or A_{26}), \tag{1.26}$$

where A_i represents the i th symmetry axis or plane, and $P(A_i)$ means the channeling probability for a symmetry axis or a plane, which is a multiplication of one of 0 or 1 and Eq. 1.26. For the multiplication of 1, each ϕ_i should be lower than $\phi_{c,i}$.

$$P_{rec} \;=\; \frac{1}{4\pi}\int \chi(E,\mathbf{q}) d\Omega_q \tag{1.27}$$

With this calculation, N. Bozorgnia *et al.* obtained the channeling fractions in the crystal scintillators and Fig. 1.16 depicts the results. In this figure, the recoil ions have a 2 % of the channeling probability at most at 100 keV energy and at lower energies, due to the similar distance of $\rho_c or x_c$ with the half width of the open space, the probability decreases drastically.

1.3.3 Implication to our experiment

The channeling effect certainly increases the scintillation yield in the scintillator due to its large ratio of the electronic stopping power for the total stopping power. Since events produced by the WIMP–nucleus scattering increases exponentially at the lower energy, the effect plays a role to make the sensitivity for the dark matter search to increase by enhancing some of events to a level that is above the energy threshold in the measured energy spectrum. Although due to the blocking effect, the channeling fraction in the scintillator may be not enough, however, due to the large amount of events in lower recoil energies, counts/keV/kg/day of the channeling effect can be nonnegligible. Moreover analytic calculations of the channeling fraction can not include the effects of reentering the channel and the resultant scintillation yield. Thus numerical methods to reproduce the scintillation yield associated with the channeling effect is necessary. Another thing to expect to measure is the blocking effect. Due to the time reversal relation, the blocking fraction should be the same as that of the channeling of incident ions, thus to measuring the effect might be

easier than the channeling effect for recoil ions. So if we observe the blocking effect, it could be a guarantee that we could observe the channeling effects in the scintillation crystal, although with smaller probability.

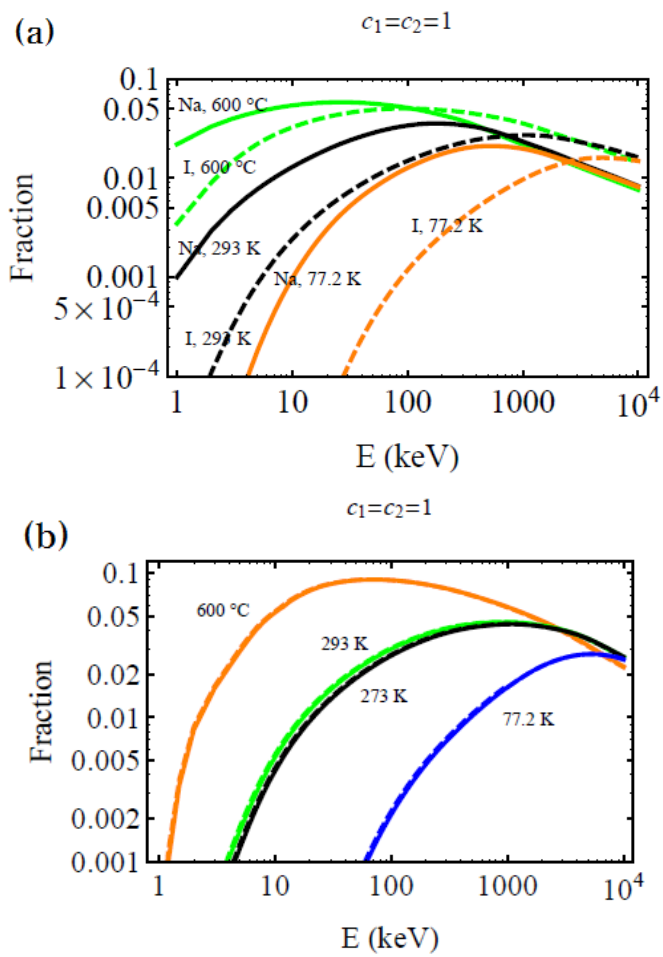

Figure 1.16: The channeling fraction upperbound with setting 1 to C_1 and C_2 and without dechanneling effect for NaI(Tl) (a) and CsI(Tl) (b) [44][2]

1.4 Scintillation detector

CsI(Tl) and NaI(Tl) have been widely used for the fields of security, medical techniques, particle experiment and so on due to their fast responses and high light yields. They yield 65,000 photons/MeV and 38,000 photons/MeV and have the decay times of 800 ns and 230 ns for the fast scintillation components, respectively [45]. The scintillations in these detectors are in visible range, with peaks at 540 nm and 410 nm respectively and the color centers are expected to be the Tl dopants, since the doped crystal produces higher scintillation yield at the different wavelength region in the comparison with the undoped crystal. From the point view of the crystal engineering, studies of their luminescence(color) center, the scintillation mechanism and the temperature dependent characteristics of the yield and the decay time have been performed [46][47][48][49][50][51], although there are different conclusions. The next section 1.4.1 will introduces the general description of the scintillation mechanism and results of the references for different models.

For dark matter searches, KIMS uses CsI(Tl) , and DAMA and NaIAD use NaI(Tl) . KIMS measured the response of the scintillation detector for radiation sources of gamma, electron, alpha and ion to figure out how to identify the source of measured signals in their detectors. In order to do that, they measured the scintillation yields for gammas or electrons and use these to set the energy scale, and the scintillation decay time induced by each source for use as an event source selector. After classification and selection, they estimate the cross-section of the interaction of WIMP-nucleus scattering based on the measured event rate. However, to obtain better selection efficiency, an understanding of the scintillation process from the irradiation to the scintillation in the crystal is necessary. DAMA and NaiAD discriminate only PMT noise by the scintillation decay time, but did not go further for the scintillation characteristics because their background measurement indicates that their crystals and PMTs are very pure, with event rate level of 1 count/keV/kg/day.

1.4.1 Scintillation mechanism

When a scintillator is irradiated by gammas or charged particles, free electrons and holes are produced in the material by the photo-electric effect and the Compton scattering, and the kinetic energies of hot electrons are degraded by thermalization and the creation of phonon, plasmon and point defects while undergoing cascades into secondary electron, x-ray and delta-ray. After cool-down and cascade, they are trapped or recombined as excitons and decay to the ground state with or without emitting scintillation light and some of secondary electrons and x-ray can escape from the surface [52][46]. This is an outline of the scintillation process. Fig. 1.17 depicts the motions of an electron and a hole after the cool-down to be at the bottom of a conduction band and the top of a valence band for each of them. Here A means an activated site like that of a thallium in CsI(Tl) crystal and there can be another interband site of Tl_0, when a Tl^+ captures an electron [49].

Z. Wang *et al.* [46] constructed a MC tool, NWEGRIM, to reproduce the thermalization of electrons created by gamma excitation. Fig. 1.18 shows the end state of electron energies after the thermalization, and the first peak in the graph represents the electron energy after the plasmon decay, which means that electrons lose their energy by moving the electron cloud around a lattice, of which energy is lower than the bandgap energy of the crystal. The end state of electrons are divided into the recombined electrons as self trapped excitons(STEs), thallium trapped electrons and stopped electrons, and the incident gamma energy dependence of the fraction of each category from the simulation is shown in Fig. 1.19. They argue that the scintillation in CsI and CsI(Tl) is mainly caused by the STE-STE radiation decay, and the Tl trapped electrons in CsI(Tl) can be another luminescence center and may be the source of the slow component of scintillation due to the same tendencies according to incident gamma energy for the fraction of the slow component in the measurement and Tl trapped electrons in the simulation.

V. Nagirnyi *et al.* [47] measured four different emissions of 3.31 eV, 3.08 eV, 2.55 eV and 2.25 eV, of which ratio and decay times are dependent on

the temperature, after irradiation of CsI(Tl) with UV light. They assumed a perturbed STE model to explain the visible emissions of 2.55 eV and 2.25 eV in CsI(Tl) as Fig. 1.20-(b). For the UV emissions, they assumed the triplet state of Tl^+, however, when they raised the temperature until 300 K, they observed the signature of the energy transfer between those centers as shown Fig. 1.21.

V. Yakovlev *et al.* [49] and L. Trefilova *et al.* [50] have a different point of view for the luminescence center. They measured optical absorption density in the large wavelength after irradiating CsI(Tl) with 250 keV electrons. The spectrum is shown in Fig. 1.22 and each peak corresponds to the absorption of each luminescence center, $6^2P_{1/2} \rightarrow 7^2S_{1/2}$ and $6^2P_{1/2} \rightarrow 6^2P_{3/2}$ in Tl^0 center for the 1.3 eV absorptions, $6^2P_{1/2} \rightarrow 6^2D_{3/2}$ in Tl^0 center for 2.25 eV absorption, $^2\Sigma_u^+ \rightarrow ^2\Sigma_g^+$ in V_k center,I_2^-, for the 3.0 eV absorption, and $^2\Sigma_u^+ \rightarrow ^2\Pi_g^+$ in V_k center for the 1.9 eV absorption. Since they did not observe the absorption of excitons, they conjectured that the Tl^0 and V_k are the luminescence centers and the decreasing rise time in the scintillation kinetics measurement above 90 K support the V_k movements to near Tl^0 sites. According to the number of activated sites and the excitation density, the ratio of $[Tl^0V_k]$ and $[Tl^+V_k]$ is determined. If the temperature is above 170 K, the thermal energy, above 0.13 eV, arise the hopping of an electron in Tl^0 to the $[Tl^+V_k]$, so the rise time decrease and the scintillation yield increases continuously. The radiation recombination of Tl^0 and V_k is conducted by one of the two kinds of paths as shown Fig. 1.23. In this figure, Type I corresponds to the 2.55 eV emission center and Type II to the 2.25 eV emission center at 80 K. and the former shows the fast decay time and the latter shows the slow decay time, however, at 295 K, 2.25 eV emission is the dominant one [49]. L. Trefilova *et al.* [50] tested the temperature dependent rise time for the crystals under 4×10^{-3} Tl concentration, and conclude that only crystals above that concentration can construct Tl sub-band and make electrons transfer from Tl^0 to Tl^+. For the slow rise component, above 130 K, V_k can disassociate from $[Tl^+V_k]$ with above 0.26 eV energy and go to near the Tl^0 site. Also electrons

in Tl sub-band above 170 K take a role for the slow rise component. And because of this Tl sub-band, they concluded that internal photo-effect under UV radiation inside CsI bandgap of 6.2 eV is possible.

R. T. Williams *et al.* [48] performed a measurement for the excitation density dependent scintillation yield and construct a model to explain the results. This main purpose is to explain the scintillation quenching, which will be mentioned in detail in the next section, however, they refer to STE(Self trapped exciton) as one of the luminescence center at room temperature, which is different argument with V. Yakovlev *et al.* It may be the difference of the excitation density, since the probability to be recombined as STE increases with it, and they observed 4.1 eV (302 nm) emission as pure CsI, though the yield is much lower than 2.25 eV emission.

From this study, we can conjecture that the different conclusions between these experiments may come from different conditions of temperature, Tl concentration, and excitation density. KIMS also measured the emission spectra and the scintillation decay time for CsI(Tl) , however, two experiments showed different results, 2.95 eV (486 nm), 2.38 eV (500nm) and 2.21 eV (560 nm) emissions with 0.6 us favored decay times at one time [53] and 2.21 eV (560 nm) and 1.9 eV (640 nm) with 1∼4 us favored decay times at the other time [54]. These measurements had a purpose of better understanding about the different decay times of electron, alpha and ions, but the separate experiments with slightly different setups with different energies and powers of lasers could not give any implications. Currently we conjecture that the higher excitation density, which is referred to the stopping power, contributes to the fast decay time which is based on the comparison of the stopping powers and the measured scintillation decay times for the three kinds of particles. Furthermore, we expect the fast component is due to the perturbed STE and the slow component due to the $[Tl^0V_k]$ center based on the summary for all references that we mentioned. Although we expect that we reach to the satisfied conclusion nearer, the emission spectra which are other than 2.25 eV are still unclear about their origins.

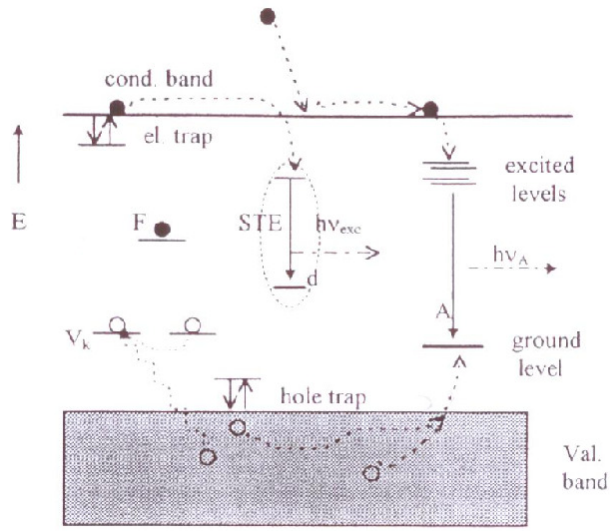

Figure 1.17: Final stage of scintillation process in the energy band scheme of a crystal [52].

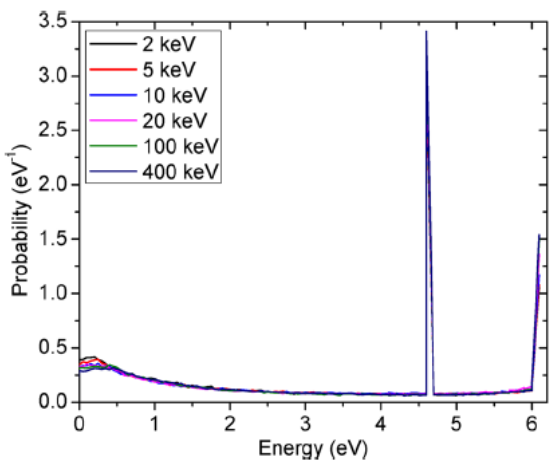

Figure 1.18: Kinetic energy distribution of hot electrons at the end state of the cascade [46].

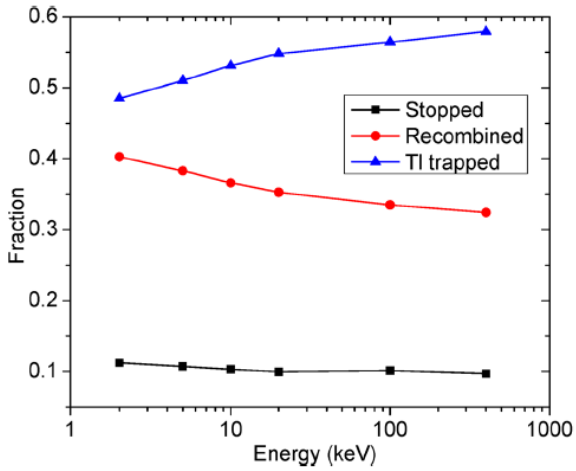

Figure 1.19: Changes in the fraction of stopped, recombined, and Tl-trapped electrons in CsI(Tl) as a function of gamma incident energy for a Tl concentration of 0.1 mol% [46].

1.4.2 Scintillation efficiency, the stopping power, and the proportionality

In the previous section, we provide a summary the scintillation process from the irradiation to the luminescence based on the measurements and the models. In this section, we concentrate on the scintillation efficiency and their nonproportionality for the excitation density.

R. B. Murray and A. Meyer [56] collected data of the scintillation efficiency about the stopping power from different experiments and tried to make a universal formula, which is only dependent on the stopping power of a particle in CsI(Tl) and NaI(Tl) based on their model. The model describes the diffusion motions of excitons to the Tl activated site followed by the recombination luminescence. They assume the high excitation density brings out the saturation of Tl sites, so the scintillation quenching arises. For electrons, due to their lower stopping power than other charged particles, the saturation is assumed not to occur. Eq. 1.28 represents the model, where ϵ is the energy to make

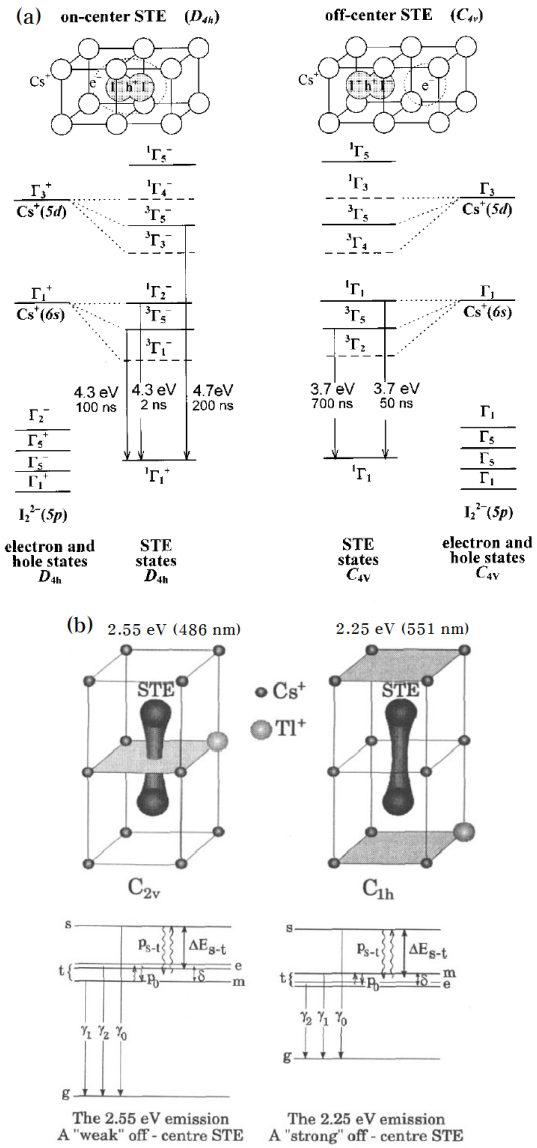

Figure 1.20: Lattice configurations and electron states of STEs in CsI (a) [55] and perturbed STEs in CsI(Tl) (b) [47].

a pair of a free electron and a hole; n_0 and n_e is each the number density of excitons and electron-hole pairs and its ratio is $\frac{\alpha K(dE/dx)}{(1+\alpha K(dE/dx))}$; S is the cap-

tured exciton ratio by Tl sites; P_r is the radiation transition probability for an excited Tl^+; P_e is the probability to escape quenching by near Tl site. The function is fitted to the data as depicted in Fig. 1.24. However, J. B. Birks [57] said that Eq. 1.28 does not match the experimental data, and this function should be modified as Eq. 1.29, but the former can be modified to be like the latter by changing parameters, as presented in section 2.4.2. To reproduce the scintillation yield in this study, we use a similar form of Eq. 1.29 after fitting it to the experimental data in [58] to get parameters, which are the normalization factor and B', and αK inherited from [56]. In Fig. 1.24, the left rising part with the electronic stopping power represents the electron performance in NaI(Tl) and arrives at maximum above 20 $MeV \cdot cm^2/g$. After that, the

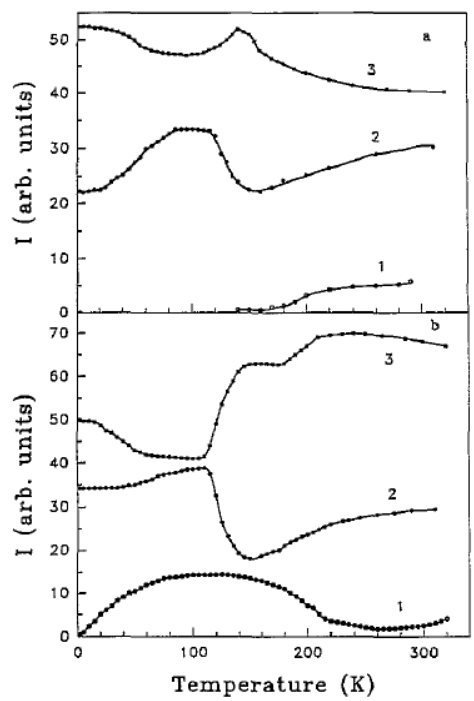

Figure 1.21: Temperature dependence of the intensities of the 3.09 eV (1), 2.55 eV (2) and 2.25 eV (3) measured on the excitation in the maxima of 4.504 eV absorption band (top) and the 4.3 eV absorption band (bottom) [47].

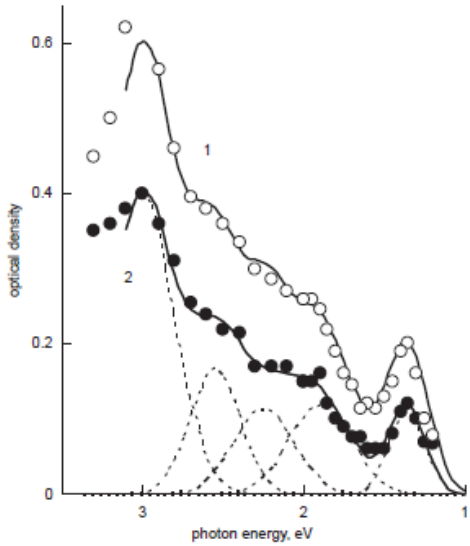

Figure 1.22: Optical absorption spectra of CsI(Tl) at 80 K at different time delay after the irradiation [49].

fitting function in Fig. 1.24 but also Eq. 1.28 and Eq. 1.29 show the quenching effect, which had decreasing tendency for increasing stopping power, however, the explanations for that haver not been proven.

$$dL/dE \;=\; \frac{1}{\epsilon}\frac{n_0}{n_e}\; S\; Pr\; P_e \tag{1.28}$$

$$dL/dE \;\propto\; \frac{\alpha K(dE/dx)}{(1+\alpha K(dE/dx))}\frac{1}{(1+B'(dE/dx))} \tag{1.29}$$

R. T. Williams *et al.* [48] measured scintillation yields in CsI and CsI(Tl) after irradiating them by using 5.9 eV laser beam with nine different intensities. They made a diffusion-drift model as Eq. 1.31.

$$\begin{aligned} \frac{\partial n(\mathbf{r},t)}{\partial t} &= -\nabla \cdot \mathbf{J}_e(\mathbf{r},t) \\ J_e(\mathbf{r},t) &= -D_e \nabla n_e(\mathbf{r},t) - \mu_e n_e(\mathbf{r},t)\mathbf{E}(\mathbf{r},t) \\ \nabla \cdot \mathbf{E}(\mathbf{r},t) &= \frac{\rho(\mathbf{r},t)}{\epsilon\epsilon_0}, \end{aligned} \tag{1.30}$$

where $\mathbf{J}_e$ is the electron current density; n_e is the electron number density; D_e is the diffusion coefficient of $\mu_{e\ or\ h} k_B T/e$; $\mathbf{E}$ is the electric field which is obtained by Gauss's law in this equation and $\rho(\mathbf{r},t)$ is $e[n_h - n_e]$. And they considered two kinds of quenching terms as follows:

$$\frac{\partial n_{ex}}{\partial t} = -k_2(t) n_{ex}^2(\mathbf{r},t) \tag{1.31}$$

$$\frac{\partial n_e}{\partial t} = -\gamma n^3(\mathbf{r},t), \tag{1.32}$$

where $k_2(t)$ is the dipole-dipole quenching parameter and n_{ex} is the exciton number density; γ is the Auger quenching parameter. Here n_{ex} is not same to n_e, but they estimate n_{ex} by calculating the average distance of electrons and holes at the stationary time, τ, with Eq. 1.31 and Eq. 1.33 and defining the ratio of independent carriers and recombined carriers.

$$\mathbf{d}_e(\mathbf{r},t) = \int_0^\tau \frac{\mathbf{J}_e(\mathbf{r},t)}{n_e(\mathbf{r},t)} dt \tag{1.33}$$

Figure 1.25 shows that the higher the excitation density, the faster the scintillation rise and decay in pure CsI, which is attributed by the higher exciton number density and their dipole-dipole quenching. $k_2(t)$ can be obtained from the fitting function. However, for CsI(Tl) , there was no difference for the different excitation densities. This represents Tl sites remove the dipole-dipole quenching and excitons are relaxed at those sites with radiations, even though it should be studied further whether the electron-hole pair near a Tl is an Tl^{+*}, a Tl with an exciton, or $[Tl^0 V_k]$, since the criteria for the independent or the recombined is the Tl-Tl spacing. From Fig. 1.26(a), we can infer the exciton density according to the stopping power, and the implication of the left region is similar with the measured Fig. 1.24 and simulated Fig. 1.19 values.

R. T. Willams *et al.* [48] explained this with the difference of mobility for the electron and the hole. In this work, we conjecture that the nonproportionality of electron and gamma response in CsI(Tl) above tens of keV energy in the measurement, which is the decreasing tendency increasing incident energy, is due to this reason. However, there are measurements that show a decrease in the scintillation efficiency above 10 $MeVcm^2/g$ in the CsI(Tl) , same region for low energy electron and gamma, but this work can explain that. It may be due that in [48], 0.3 % Tl, a quit high concentration, was used.

1.4.3 The quenching factor of ions and the scintillation yield of channeling events

Since even for electrons and gammas, there is the nonproportionality in the scintillation efficiency, it seems not strange that the ion response has nonproportionality. For ions, there is a defined variable to represent the ratio between the scintillation yield and the incident energy, which is called the quenching factor. The definition of quenching factor is as follows:

$$Quenching\ Factor = \frac{E_{meas}}{E_{recoil}} = \frac{L_{meas}}{E_{recoil}} \frac{E_{\gamma,calib}}{L_{\gamma,calib}}, \tag{1.34}$$

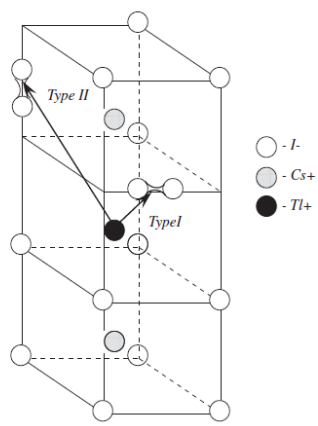

Figure 1.23: Models of the two types of close pairs $[Tl^0V_k]$ in CsI(Tl) [49].

where $E_{\gamma,calib}$ is the energy of gamma calibration source and $L_{\gamma,calib}$ is light yields of those gamma. This is the variable used to convert the measured energy to the recoil energy in WIMP search. We usually use an energy of a

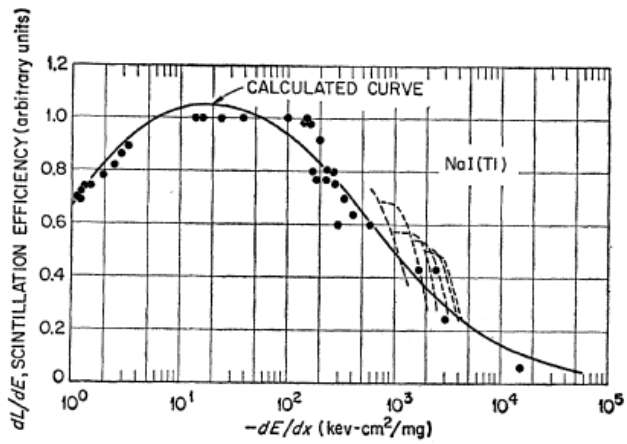

Figure 1.24: The fitted function of the saturation model in NaI(Tl) to experimental data [56].

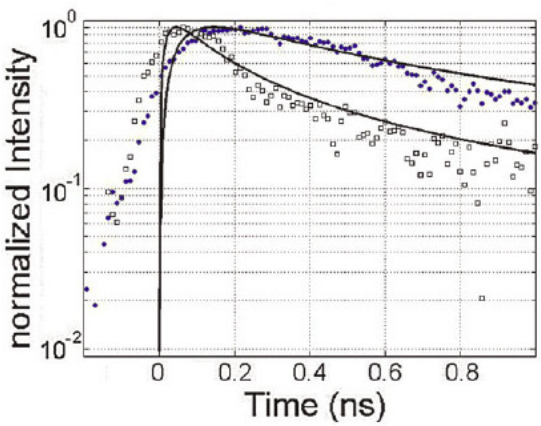

Figure 1.25: Comparing decay of 4.1 eV STE luminescence in CsI at room temperature. Filled points are for the lower excitation density and open points are for the higher excitation density [48].

gamma or electron for the calibration in the quenching factor measurement, so the nonproportionality of the gamma or the electron can affect the value of the quenching factor according to which source we use for the energy calibration.

Even though the calibration source response in CsI(Tl) is linear, the quenching factor can vary with incident ion energy or the recoil energy as shown in Fig. 1.24 and Fig. 2.14. This is due to the difference of the electronic stopping power, which is the ionization energy loss per unit depth and is mentioned in detail in section. 1.5.1. Figure 1.27 depicts the nuclear stopping power and the electronic stopping power for different ion energies in CsI(Tl) and NaI(Tl) obtained from SRIM program [3]. From the measured quenching factors and Fig. 1.27 [6], we can conjecture that the anti-correlation between the electronic stopping power and the scintillation yield can be explained by the Birk's formula in Eq. 1.29. But the quenching mechanism should be studied further.

In section. 1.3, the enhanced scintillation yield for ions moving between symmetry axes or planes, which is called the channeling effect, is described. The reason for the enhancement is not only the decrease of the nuclear stopping power, which is the energy transfer to the nulceus, but also the decrease in the electronic stopping power, which is the energy transfer to electrons.

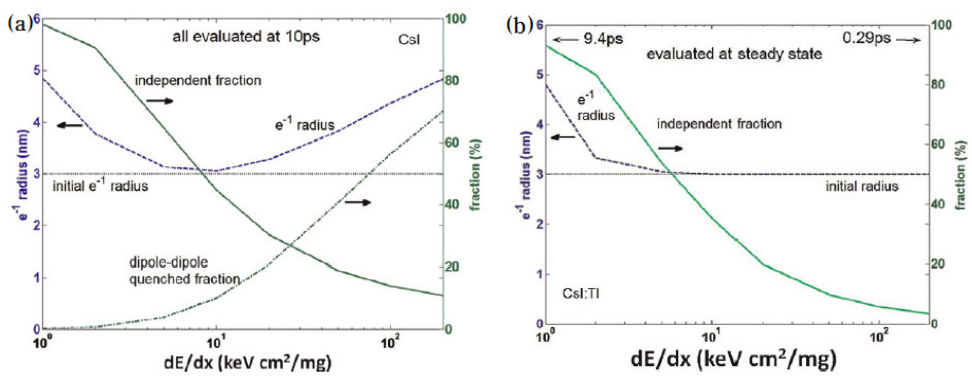

Figure 1.26: The e^{-1} radius of the electron distribution and independent fraction at the steady state time in the CsI (a) and CsI(Tl) of 0.3 % Tl (b) [48].

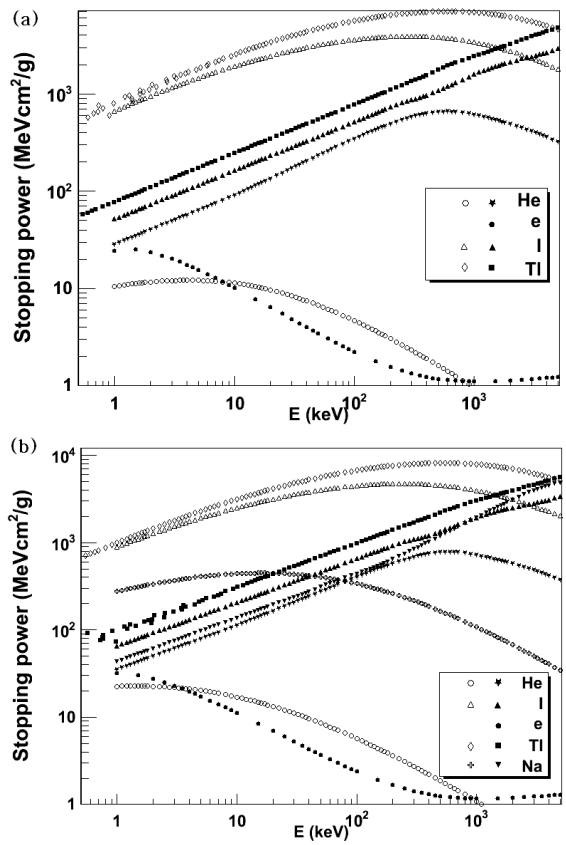

Figure 1.27: The nuclear(S_n) and electronic(S_e) stopping power for various particles in CsI(Tl) (a) and NaI(Tl) (b). The open circles are S_n, and the filled squares are S_e. For the electron, we used estar program [59].

Because the scintillation yield has an anti-correlation with the electronic stopping power as Birk's formula, and the larger the impact parameter between a projectile ion and a target atom, the lower the electronic stopping power. Thereby the range of the projectile ion increases. Therefore, the scintillation response may looks like that of a gamma, if the ion energy is a several tens of keV, in which case a gamma is expected to have a low stopping power, under 10 $MeVcm^2/g$ and a scintillation decay time increases with containing of the larger slow component, Tl trapped electrons [46].

1.5 Simulation tools for reproducing the scintillation yield

In order to simulate particle interactions with detectors, we usually use the GEANT4 program, which is developed by CERN [41]. Although the complex experimental setup can be constructed and various analytical formula or cross-section tables in regard of physics process are included, the scattering process between ions and the material can not be described in detail. GEANT4 uses ICRU 73 for the stopping power of heavier ions than heliums, however the minimum energy of the table limits its applicability for lower energy particles. The stopping power is explained in the next subsection in detail. Since for describing the channeling effect in the scintillation detector, we are interested in where in a material and how much ion's initial energy is lost and how far the ion can penetrate, we use other programs, SRIM [3] and MARLOWE [4]. They are binary collision cascade programs which contain the classical interatomic potential and the electronic energy loss model. By the simulations with these codes, we can reproduce the movement of ions and secondary recoil ions. For SRIM, the measurements fit the simulation results within 5%.

1.5.1 SRIM [3]

SRIM has a characteristic of the universal screening potential. Since atoms have electron clouds surrounding themselves, the Coulomb potential between two nuclei is screened as follows:

$$V(r) \;=\; \frac{Z_1 Z_2 e^2}{r}\Psi(r), \tag{1.35}$$

where $\Psi(r)$ is the same screening function as in Eq. 1.9, which is defined by $V(r)/V_{coulomb}(r)$, Z_1 and Z_2 are the atomic numbers of two atoms, and r is the distance between them. The author calculates $V(r)$ from the sum of $V_{nn} + V_{ne} + V_{ee} + V_k + V_a$, where V_{nn} is a nucleus-nucleus Coulomb potential, V_{en}, a sum of electron-target nucleus potential, V_{ee}, a sum of electron-target electron potential, V_k, a kinetic energy, which is earned by incident electrons from Pauli

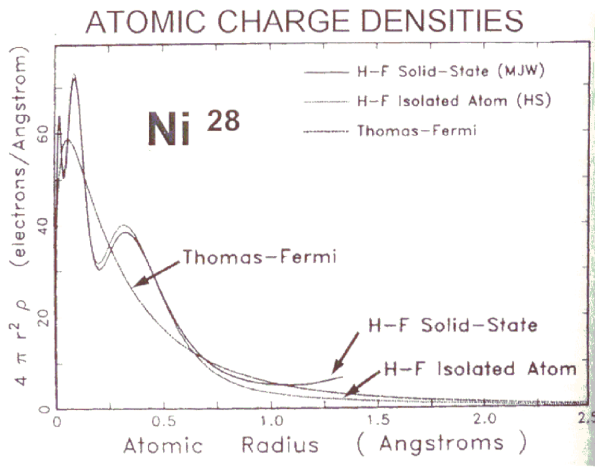

Figure 1.28: The calculated atomic charge densities for ^{28}Ni atoms. Thomas-Fermi atom has no shell, but a HF atom has the inner shells in a face centered crystal(FCC) [3].

principle in the case of overlap of electrons, and V_a, an exchange energy from same spin electrons. The electron density is calculated by assuming Hartree-Fock(HF) atoms in a solid state to express dense electron shells of K, L and M inside the electron halo, which decrease with as distance from the nucleus as shown Fig. 1.28. When $\Psi(r)$, which is obtained from $V(r)$, is scaled with a universal screening length of Eq. 1.36, a_u, where a_0 is a Bohr radius of 0.529 $\mathring{A}$, they can contract all of the screening functions for various atom compositions into a narrow line as Fig. 1.29, so they fit them with a universal function:

$$a_u = \frac{0.8853 a_0}{(Z_1^{.23} + Z_2^{.23})} \tag{1.36}$$

$$\begin{aligned} \Psi(r/a_u) &= .1818 exp(-3.2 r/a_u) + .5099 exp(-.9423 r/a_u) + \\ & .2802 exp(-.4028 r/a_u) + .2817 exp(-.2016 r/a_u). \end{aligned} \tag{1.37}$$

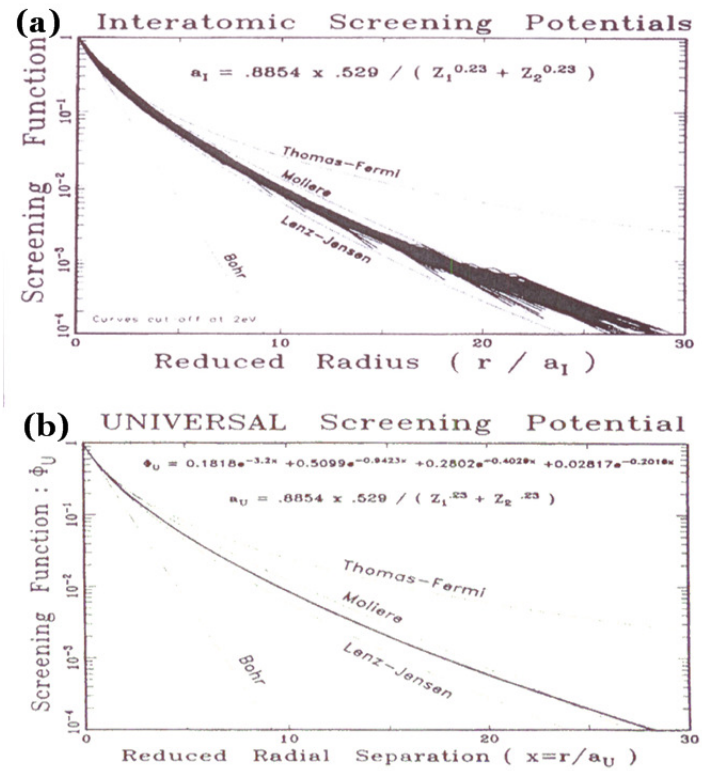

Figure 1.29: The various screening functions. a_I is same as a_u. The crowded lines are from the calculations by authors of SRIM for many atom compositions.(a) The solid line is the universal screening function from fitting. (b) And other screening functions are also depicted to compare each other [3].

Stopping power [3]

Stopping power is the energy loss produced as an ion slows down at every unit penetration depth in a material. It can be divided into two kinds, one is the nuclear stopping power(S_n) and the second is the electronic stopping power(S_e). The nuclear stopping power is the average of energies which are transfered to target atoms of different impact parameters in a unit depth. We

can represent it as follows:

$$\begin{aligned} S_{n,ion}(E) &= \int_0^\infty T(E,p)2\pi p dp \\ &= 2\pi\gamma E \int_0^{p_{max}} sin^2\frac{\Theta}{2} p dp, \end{aligned} \tag{1.38}$$

where T is the transfered energy, E is the incident ion energy, γ is $4M_1M_2/(M_1+M_2)^2$, and p is the impact parameter. Θ in this equation is the scattering angle in the center of mass frame, which is obtained as follows:

$$\Theta = \pi - 2\int_{x_0}^\infty \frac{bdx}{x^2[1-\frac{\Psi(x)}{x\epsilon}-\frac{b^2}{x^2}]^{1/2}}, \tag{1.39}$$

where x is a reduced distance, r/a_u, and b a reduced impact parameter, p/a_u, x_0 a reduced closest approach distance, and ϵ a reduced energy, $a_u M_2 E_0/Z_1 Z_2 e^2(M_1+M_2)$. $\Psi(x)$ is the same as Eq. 1.37. So, we can obtain any nuclear stopping powers for any ion-atom compositions with any ion's energy. However, the authors made this calculation much simpler with a fitting function of $S_n(\epsilon)$, which is $\frac{\epsilon}{\pi a_u^2 \gamma E_0} S_n(E)$. Eq. 1.41 shows a function with only 1 parameter, which is obtained by using the solution of Eq. 1.38 and the fitting. The straggling of $Q_n(E)$ which is similar with the standard deviation of $S_n(E)$, is defined as $\int_0^\infty T^2 d\sigma$ and its simple and empirical function is given in Eq. 1.42.

$$S_n(\epsilon) = \frac{ln(1+1.1383\epsilon)}{2[\epsilon+0.01321\epsilon^{0.21226}+0.19593\epsilon^{0.5}]}\ ,\ \epsilon \geq 30 \tag{1.40}$$

$$S_n(\epsilon) = \frac{ln(\epsilon)}{2\epsilon}\ ,\ \epsilon > 30 \tag{1.41}$$

$$Q_n(E) = \frac{\gamma}{4+0.197\epsilon^{-1.7}+6.584\epsilon^{-1.0494}}. \tag{1.42}$$

Electronic stopping power of protons is represented by an empirical corrected function from the Lindhard's theory shown in Eq. 1.43, which fits well with the experimental stopping power.

$$S_e = \int I(v,\rho) Z_1^2 \rho dx^3, \tag{1.43}$$

where

$$I \;=\; \frac{4\pi e^4}{mv^2}\cdot\frac{i}{\pi w_0^2}\int_0^\infty \frac{dk}{k}\int_{-kv}^{kv} wdw[\frac{1}{\epsilon^L(k,w)}-1], \tag{1.44}$$

where v is ion's velocity, ρ is the density of electrons in a target atom, of which integral about a total volume of the atom is same to the atomic number of the target atom. In Eq. 1.44, the longitudinal dielectric constant, ϵ_L is

$$\epsilon^L \;=\; 1+\frac{2m^2w_0^2}{\hbar^2k^2}\sum_n \frac{f(E_n)}{N}[\frac{1}{k^2+2\vec{k}\cdot\vec{k_n}-\frac{2m(w-i\delta)}{\hbar}}+\frac{1}{k^2-2\vec{k}\cdot\vec{k_n}+\frac{2m(w-i\delta)}{\hbar}}], \tag{1.45}$$

where e and m are the charge and mass of electrons, w_0 is the classic plasma frequency, which is defined by $w_0^2 \;=\; 4\pi e^2\rho/m$, E_n and k_n are the energy and the wave vector of electrons in n_th state, $f(E_n)$ is the distribution function, and δ is a small damping factor. In this theory, not only the polarization of a plasma but also the excitation of electrons in a shell are considered in the electronic stopping power. Fig.1.30 shows the interaction function and the electronic stopping power according to the distance from the core of a target atom based on the above equations. For helium and heavier ions, the electronic stopping power is calculated with a scaled function of the effective charge, $\gamma\cdot Z_{ion}$, which is

$$\frac{S_{ion}(v)}{S_H(v)} = \gamma_{ion}^2\cdot Z_{ion}^2. \tag{1.46}$$

Because when an ion's velocity is larger than the Fermi velocity of electrons around it, they can be stripped and the ion can be a bare atom. This effective charge is assumed to be determined only by the ion's velocity and the equation for γ is represented as

$$\begin{aligned}\gamma \;&=\; 1-exp[-\sum_0^8 a_i ln(E)^i], for\ Z \;=\; 2\\ &= 1-exp[-v_{ion}/(v_0 Z_{ion}^{2/3})], for\ Z \;>\; 2,\end{aligned} \tag{1.47}$$

where the a_is are fitting parameters for the experimental ratio distribution of helium and protons for various energies, and v_0 is the Bohr velocity, 25

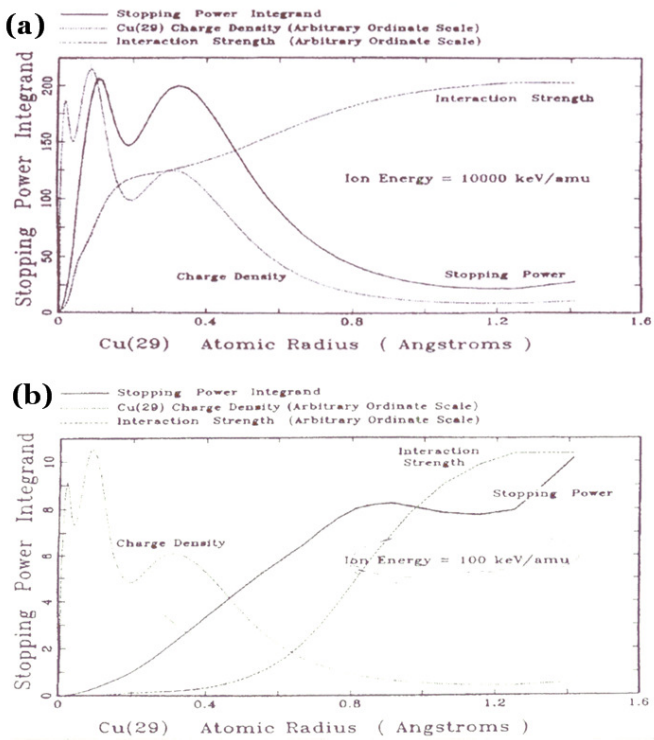

Figure 1.30: The interaction function for the electronic stopping power according to the distance from the core of a target atom for a high speed particle(a) and a low speed particle in copper atoms(b) [3].

keV/amu. From these calculations, the electronic stopping power can be represented simply as $kv^{0.9}$ for a proton of which velocity is below 25 keV/amu except for $Z_2 \leq 6$, in which case, $Se = kv^{0.5}$, and for a helium below 1 keV/amu, $Se = kv^{1.0}$. What we are interested in among them is the low velocity heavier ions, since we are intend to reproduce the scintillation yield induced by recoil Cs or I ions of tens of keV in CsI crystal. For this case, Lindhard and Firsov considered a model of slow heavy ion in a uniform electron gas, where the electronic stopping power is proportional to the ion's velocity except for $Z_{ion} \leq 19$ in a target of $Z = 6, 14, 32$ due to its bandgap structure, where $Se = kv^{0.75}$, since if an ion's energy is low enough, the electronic

interaction is mostly concerned with conduction band electrons as Fig. 1.30 (b).

Magic formula and Free flight path [3]

Another characteristic of SRIM is the use of the Magic formula (Eq. 1.48), and Free flight path for the fast calculation with the high accuracy. From Fig. 1.31, which depicts the particle trajectory in the center of mass(CM) frame, we can derive the magic formula.

$$cos\frac{\Theta}{2} = \frac{B + R_c + \Delta}{R_0 + R_c}, \tag{1.48}$$

where Θ is the scattering angle in CM frame as shown in Eq. 1.39, B is the reduced impact parameter by the universal screening length, a_u, R_c is the reduced radius of the curvature at the closest approach, R_0 is the reduced distance at the closest approach, and Δ is the reduced correction term. When an ion has high enough velocity, there should be unscreened Coulomb interaction potential, the Rutherford scattering, so Δ can be represented as follows:

$$\begin{aligned} \Delta &= A\frac{R_0 - B}{1 + G} \\ A &= 2\alpha\epsilon B^{\beta} \\ G &= \gamma[(1 + A^2)^{1/2} - A]^{-1}, \end{aligned} \tag{1.49}$$

where $\alpha = 1+C_1\epsilon^{-1/2}$, $\beta = \frac{C_2+\epsilon^{1/2}}{C_3+\epsilon^{1/2}}$, and $\gamma = \frac{C_4+\epsilon}{C_5+\epsilon}$. C_1 to C_5 are determined by fitting.

Another thing to make the SRIM calculation more exact and faster is the free flight path, which means that within the distance, an ion loses an amount of energy that is small enough to be neglected. High energy ions can pass some of target layers due to the decreased nuclear stopping power :

$$\begin{aligned} \frac{M_2\Delta E_n}{M_1 E} &= \frac{M_2 L\ S_n(E)}{M_1 E} = constant \\ L &= \frac{0.02[1 + (M_1 + M_2)]^2\epsilon^2 + 0.1\epsilon^{1.38}}{4\pi a_u^2 N\, ln(1 + \epsilon)}. \end{aligned} \tag{1.50}$$

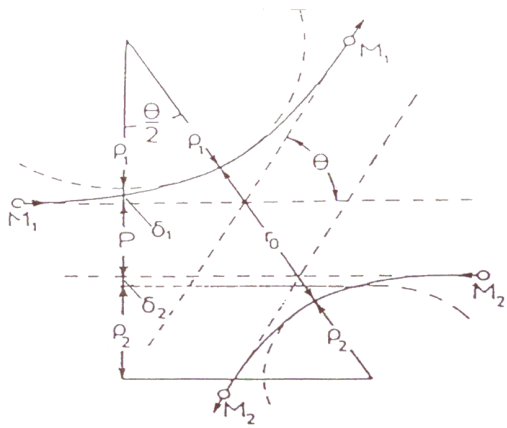

Figure 1.31: The particle trajectory in the CM frame and the scattering angle. p is an impact parameter, r_0 is the closest approach distance, which is obtained from the solution for the denominator in Eq. 1.39 to be zero, ρ_1 and ρ_2 are the radii of the curvature of the trajectory at r_0, and δ_1 and δ_2 are the small corrections, which will be explained in the context in detail.

If we define the free flight path, L, as the distance at which the scattering angle is about 5°, we can calculate it with Eq. 1.50 and the minimum impact parameter to be used for finding target atoms as

$$W(p)\delta p = W_2(p)W_1(p)\delta p = exp(-NL\pi p^2)NL2\pi p\delta p$$
$$p = [-ln(R_n)/\pi NL] \quad , \tag{1.51}$$

where $W_1(p)\delta p$ is the probability for a target to be about $p + \delta p$, $W_2(p)\delta p$ not to be there, R_n is one of the random number from 0 to 1, and N is the mean volume of a unit cell . For low energy ions, which we are interested in for WIMP search, the free flight path is similar to the mean interatomic distance, $N^{1/3}$, and the minimum impact parameter can be calculated with $[R_n/(\pi N^{2/3})]^{1/2}$. Whether we consider the free flight path or not, the results are not different.

Table 1.3: Categories of the deposit energy in the binary collision cascade

Name	Case	Deposit energy to the material
PhononE	$E_t \leq E_d$ && $E_p > E_d$	E_t
	$E_p \leq E_d$ && $E_t > E_d$ [a]	E_p
	$E_p \leq E_d$ && $E_t \leq E_d$	$E_p + E_t$
IonizationE	$E_p > E_d$	$k\sqrt{(E_p)}$
DamageE	$E_t > E_d$	E_b
	Escaping of ions	E_p

[a] Only the case of $Z_t = Z_p$; the replacement.
Here E_p and E_t is the energy of a projectile ion and a target atom after a collision, respectively, and E_d and E_b is each the displacement energy and lattice binding energy.

Application

Figure 1.32 shows results from TRIM(TranspoRt of Ions in Matter) for Cs ions in a CsI(Tl) crystal. There are a lot of recoil atoms in the tracks, because the energy loss of ions with high atomic numbers like Cs is affected by nuclear stopping power more than electronic stopping power. In these cascades of binary atoms collisions, the last target atoms with kinetic energies lower than the binding energy release phonons, the lattice vibrations, and the atoms with higher energies leave their sites, which then become vacancies, with energy loss equal to the binding energy. Incident ions also stop and become interstitial ions, if the kinetic energies are lower than a cut off energy which can be set by the user. While in flight, ions and the secondary atoms lose their energy by ionization. The information about energy losses averaged for all events can be found on the right box named energy loss % in Fig. 1.32. Table 1.3 shows these three categories for the energy loss and their components. By checking the check box on the distribution menu on the leftmost side, we can get informative plots and text files easily.

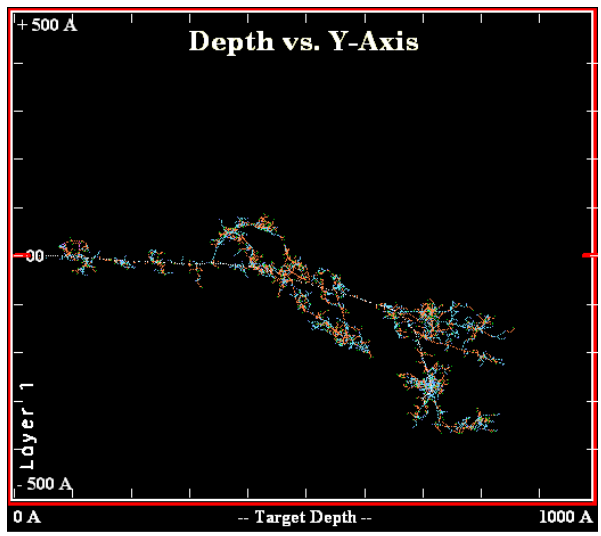

Figure 1.32: A cascade event for Cs ions with 50 keV in a CsI(Tl) crystal in TRIM. The small branches are the recoil ions.

1.5.2 MARLOWE[4]

MARLOWE 15b is the latest version program among those having the same name, edited in 2003. It can be obtained in [4] after registration and submitting a request on the web. It is also a binary collision cascade program with the impulse approximation like SRIM, which means the potential energy from other atoms can not affect the energy transfer between a projectile ion and a target atom. One of the characteristics of this program is that it considers not only amorphous but also polycrystalline and monocrystalline targets. Another thing is that it is an open source code written in FORTRAN so that users can list variables of interest every steps in the cascade. It contains various classical interatomic potentials and two kinds of models for the electronic energy loss. "Expsum" for the interatomic potential and Oen-Robinson model for the electronic energy loss shown in Eq. 1.52. This produces results that are similar with those of SRIM, if we use an appropriate α in Eq. 1.52, the ratio between nonlocal and local electronic energy loss. The local loss describes the

electronic energy loss varied according to the distance, or impact parameter, to the target nucleus, the first term in Eq. 1.52, and nonlocal loss is only dependent on the ion velocity, the second term in the equation. However, since SRIM uses the electron density as a function of the radius considering Hartree Fock atoms in the electronic energy loss model, matching the electronic energy losses in SRIM and MARLOWE exactly is difficult.

$$S_e^{OR}(E) = k\,E^{1/2}\,((1-\alpha)\,(\frac{\gamma^2}{2\pi a^2})\,exp(-\gamma R(p,E)/a) \\ +(1-\alpha)\,(1+\frac{\gamma P_c}{a})\,exp(-\frac{\gamma P_c}{a})+\alpha), \tag{1.52}$$

where p is an impact parameter, P_c is the maximum impact parameter which is set as the mean interatomic distance by default, γ is a constant parameter which is 0.3 in the simulation, and $R(p,E)$ is the apsis, the distance of closest approach in a collision.

This program is used mainly to see the channeling effect of ions. As explained in section 1.3, an ion between symmetry axes or planes penetrates a target more deeply. To reproduce the ion's motion, it considers the simultaneous collisions for target atoms, which have small differences in impact parameters as shown Fig. 1.33. And the linear collisions, which can be divided into focusons and replacements are also included in the physics process. Figure 1.34 shows a linear collision sequence for atoms along a $< 100 >$ row. If a projectile ion has a focuson energy, E_f, it returns to its original site with a help of a ring made of atoms in $\{111\}$ [60]; if not, the ion replaces the site of a next atom member in a sequence. For each step, a projectile ion loses its energy by a replacement binding energy, which is E_{rb} and usually $0.1 * E_b$ in Table 1.3, and stops and releases its energy into phonons. In these linear collisions, the stopping powers are also small that it is one of the reason for the increase of the range and light yield.

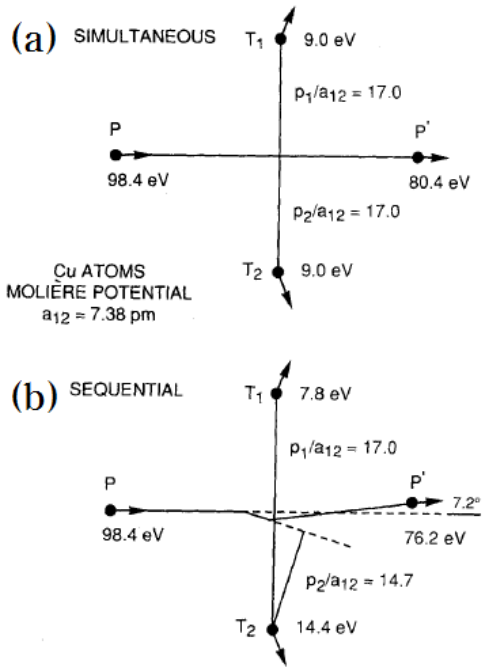

Figure 1.33: Comparing between a simultaneous (a) and a sequential (b) collision in MARLOWE. Cu ion, P, enters [110] axis of Cu target and encounters two target atoms, T_1 and T_2 , of which impact parameter is P_1 and P_2 respectively. And a_{12} is Tomas-Fermi screening length [61].

1.6 Motivation of the this study

The reason that we study the channeling effect on WIMP search is a new argument in a paper from DAMA in 2008 [5]. DAMA is one of the dark matter search groups and has reported that they observe evidence for a WIMP-induced the annual modulation. In 2007, KIMS excluded their results with a detector containing iodines [32](Fig. 1.10). It broadens the scope of our observation for the WIMP search indeed, although for the contribution of this effect, there is a different argument [2]. The channeling effect as we are dealing in section 1.3 can make the quenching factor of ions in the scintillation

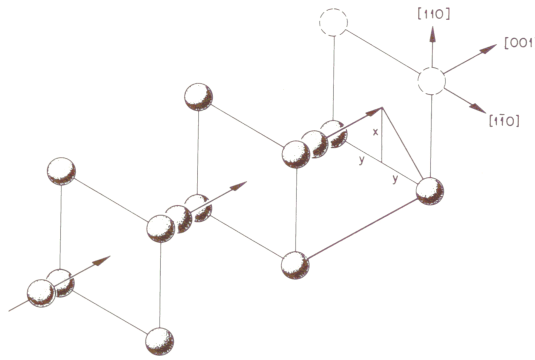

Figure 1.34: Linear collision sequence along $< 100 >$ row of fcc crystal in $\{111\}$ planes [60].

detector to be nearly unity like that for gammas or electrons, however, this has been observed only for incident ions from outside of the crystal. DAMA claimed that the WIMP detectors of CsI(Tl) , NaI(Tl) , and Ge materials certainly should observe the signals originated from the channeling effect with some fractions for total events, however, since KIMS experiment uses the pulse shape discrimination method(PSD) to remove the gamma backgrounds, they lose some of WIMP signals. DAMA estimated the fraction of the channeling effect in NaI(Tl) according to recoil ion energies, with several assumptions to make the problem simple [5]. The assumptions are in Table 1.4. In their assumption, if the recoil angle, ϕ, is under the Ψ_c on a symmetry axis or plain, the ion will be channeled, however, with some probability, it can be dechanneled and the channeling is evaluated again at that point by using the channeling probability for (E,ϕ), which is the channeling fraction without considering Tl dechanneling. The estimated channeling fraction can be found in Fig. 1.35. The calculation of the measured energy can be conjectured from the statement of Ref. [5]. They use an integral of the total stopping power multiplied by normal quenching factor with some straggling from 0 to its range for the nonchanneling ion, which is dependent on the ion energy and supplied

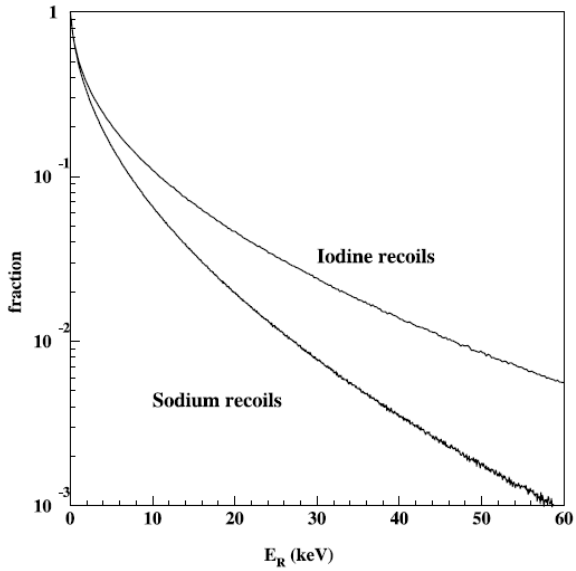

Figure 1.35: The estimated channeling fraction in NaI(Tl) according to the recoil energy from DAMA [5].

by SRIM. For dechanneling ions, which is a partial channeling plus a nonchanneling one, they do each integral for the partial channeling from 0 to λ and the nonchanneling from λ to the range with the straggling. The equations for reproducing measured energy, E_{meas}, are in Eq. 1.54 and the reproduced E_{meas} is depicted in Fig. 1.36. However, due to the energy resolution, they said that the full peak can not be observed in data :

$$E_{meas}^{normal\ scattering} = \alpha \int_0^{normal\ range} \frac{dE_{tot}}{dx}(q'(E) \pm \delta q)dx \qquad (1.53)$$

$$E_{meas}^{partial\ channeling} = \alpha \int_0^{\lambda} \frac{dE_e}{dx}dx \quad , \qquad (1.54)$$

where α is the proportionality factor; dE_{tot}/dx is the total stopping power; E_e is the electronic stopping power; λ is the Tl-Tl distance.

The estimation of the channeling fraction from DAMA does not agree with

Table 1.4: Assumptions for the Monte Carlo simulation about the channeling fraction from DAMA [5]

Factor	Assumption
Criteria for the channeling	Scattering angle $\leq \Psi_c^a$
Recoil direction	Isotropic
Recoil direction after the dechanneling	Isotropic
Dechanneling probability	$\mathrm{P(x)}^b = \frac{1}{\lambda} e^{x/\lambda}$
Energy loss in channeling	Only by the electronic stopping
Quenching factor of channeling	1
Quenching factor of nonchanneling	Normal value, $\mathrm{q(E)}^c$, with the straggling

[a] The critical angle for the channeling

[b] It is determined by the concentration of Tl impurities and λ is the mean distance between Tl ions.

[c] Normal quenching factor is measured in the neutron calibration experiment by using a peak in the measured energy distribution(E_{meas}) for certain recoil energy. Since this is a mono value, they applied the straggling for the range quenching factor obtained from SRIM to the straggling for the energy quenching factor in order to reproduce E_{meas} for nonchanneling events.

Bozorgnia *et al.* [2], because they applied the critical angle of ions to estimate the channeling fraction directly to the recoil ions which start to move from the lattice sites. For such recoil ions, we should also consider the blocking effect as mentioned in section 1.3. It is possible for the recoil ions moving with the angle under the critical angle to be channeled, but due to the blocking effect, the initial distance of them should be larger than the minimum initial distance. Since there is no experiment to see the channeling and blocking effect in the scintillation detector for heavy recoil ions like Cs and I, we decided to use a numerical simulation program to reproduce the channeling and the blocking effect in CsI(Tl) crystals for the estimation of the channeling fraction, the effect on E_{meas} distribution and the efficiency of the pulse shape discrimination,

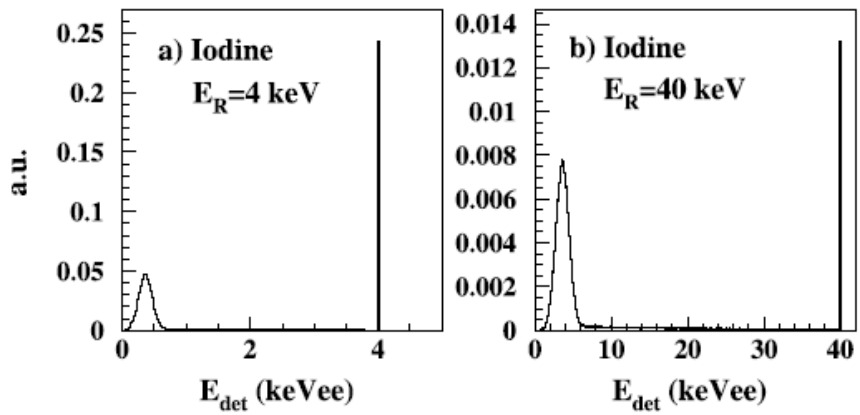

Figure 1.36: The reproduced E_{meas} for iodines of 4 keV (a) and 40 keV (b) in NaI(Tl) from DAMA calculation [5].

which is dependent on the scintillation decay time. In chapter 2, we represent the procedure to reproduce E_{meas} distribution from the electronic stopping power of the simulation programs, SRIM and MARLOWE with a scintillation efficiency model, which is a function of the electronic stopping power. And the simulation results of the channeling fraction according to recoil ion energy and the reproduced quenching factor will be presented. In chapter 3, we introduce the experimental setup to measure the channeling and blocking effect, the experiment for the calibration, and the data acquisition and the analysis method. Chapter 4 show the results of this experiment and compare them with MC data obtained by using MARLOWE and GEANT4. And then we apply the estimated channeling effect to make the expected E_{meas} distribution induced by WIMP-nucleus scattering to reanalyze KIMS data by comparing them. In this procedure we ignore the pulse shape of the channeling events, because in order to know that, we need high statistics, thus more time for data taking. So this will be postponed to the next experiment.

2 Simulation

2.1 SRIM and MARLOWE

We use these two codes to obtain the energy loss distribution of the ions in a material for each penetration depth. This information is a dominant factor to determine the scintillation yield of the crystal detector as mentioned in [56][62][63]. At first, we should set the parameters in those program for two to present similar results. Since SRIM is well known and verified with many data, and has only several parameters to set, we use the results of SRIM as a reference for use of MARLOWE. We evaluate the parameters by comparing the stopping power distribution and the energy cascade, which has three categories at final state, the ionization energy, the phonon energy and the damage energy, which will be explained in detail in section 2.1.2. The ionization energy is a part of the initial energy which is deposited to the electrons, the phonon energy is a sum of received energies of nondisplaced target atoms after each scattering, and the damage energy is a sum of binding energies which should be overcome for target atoms to be displaced after the collision. To obtain this information, the code of MARLOWE is modified a little to write them to another file. After this setup, the dependence on the crystal axis or plane for the scintillation yield can be investigated. Instead of the role of a reference, SRIM is used for the reproduction of quenching factors for high energy ions due to the lack of a model in MARLOWE for their electronic energy loss. The quenching factors for alphas estimated using SRIM will be presented in section 2.4.2.

2.1.1 Parameter setting

For driving SRIM and TRIM, we should set up several things in the main menu, the species of ion and target material with the included periodic table(PT), a target width to tracking ions, the number of generation, and the method for damage calculation as shown in fig. 2.1. There are lots of pre-established compounds in the dictionary menu for easy construction of the target material. If we make a data file of *.dat which is the same structure as an example file included in the SRIM package, we can run the simulation for different particles, energies and incident angles. However, MARLOWE needs some delicate work to make the parameter input file. Fig. 2.2 shows an example of the input file. But it can be said that it opens the possibility to simulate the collision cascade for various conditions. The user guide book in the package helps one to understand the meanings of these parameters.
The following Table 2.1 shows the parameter setup which is used for this study to obtain the identical energy loss distributions between SRIM and MARLOWE. As mentioned in section 1.5.2, the α factor of ions are found by comparing the electronic energy loss with SRIM. Since if an ion is faster and faster, it interacts with deep electrons, we should increase the local loss term by reducing α as the thin solid line on fig. 2.3-(b). However, E_{meas} changes only a few % , we use the same condition for same composition of ion-atom scattering. The comparison of the electronic stopping power(S_e) and the energy losses are presented in the next section.

2.1.2 Comparing stopping power distributions and total energy loss

Figure 2.3 depicts the electronic stopping power(S_e) distributions for the penetration depth, which are obtained from SRIM and MARLOWE with the parameters of table 2.1. They show the consistent results as expected. Table 2.2 shows the mean energies of different categories, phononE, ionizationE, and damageE for two programs. The phonon energy(phononE) is the summed

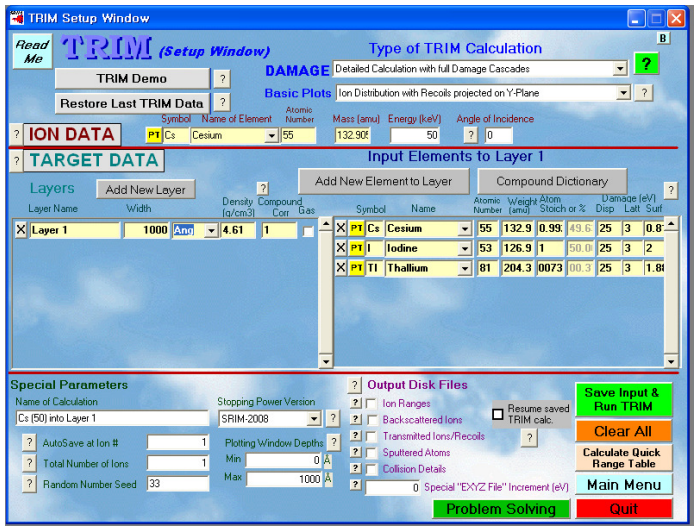

Figure 2.1: The main menu of TRIM in SRIM to set parameters.

```
Channeling Effect
with various energies
&MODL FILE(1)="file1.1st",FILE(2)="file2.1st",FILE(3)="file3.1st",FILE(4)="file4.1st",FILE(5)="file5.1st"
      ,RDNML(1)=T,RDNML(3)=T,RDNML(5)=T,RDNML(6)=T,SURFCE=1,TRAM=F,ICHAN(1)=10000000,TIM=F,F,F,T,T,T,T/
&XTAL NEWS=4,ALAT=4.5670,CENTRE=1,RZ=3*0.0,3*0.5,POLY=1,AXISA=5.0,3.0,8.0,AXISB=-1.,-1.,1./
&ATOM NTYPE=3,TYPE='Cs','I','Tl',Z=55,53,81,W=132.905,126.904,204.383,INEL=3*1,EQUIT=3*6.3
      ,EBND=6.3,0.6,0.6,6.3,0.6,0.6,6.3,0.6,0.6,LOCK(1)=-1,LOCK(2)=2,ORDER(1,1)=0.99927,ORDER(3,1)=0.00073,ORDER(2,2)=1/
&SURF ORIGIN=100.,100.,SIDES=1.0,1.0,RSRF=0.0,0.0,DEPTH=2E15,SBND=0.6,0.6,0.6/
&SIZE RB(1)=0.55,RB(2)=0.55/
&QPAR ALPHA=3*1.0/
&TVIB T=298.0,TDEBYE=3*115.08/
&OUTP DRNG=3*0.25,GREX=T,LOOK=1,TRACE=0,0,0,INFORM(1)=T/
&PROJ MAXRUN=1000,NGR=1,PRIM=0,EKIP=18400,LEAP=3,LAIP=2
      ,RAIP=100.5,100.5,0.5,TRMP=F,MILLER=F,REFIP=100.5,100.5,0.5,THA=0.,PHI=0.,DVRG=0.0/
```

Figure 2.2: An example of an input file for running MARLOWE.

kinetic energies of projectile ions when they stop interstitially in the crystal lattice when their energies are under the energy cut and those of target atoms when they vibrate at their original site after the scattering. The damage energy(damageE) is the summed kinetic energy when they escape at the target surface and the sum of binding energies of recoil atoms when they scatter off in their lattice site. For the binding energy, we apply the lattice energy if there is the measured value in the reference or a default value, $\sim$ 3 eV in SRIM if not, and for the redisplaced interstitial target atom, 0.1 * binding energy is

Table 2.1: Parameters for driving simulation codes

	SRIM and MARLOWE
S_n	From ZBL potential [3] [4]
S_e	k[a]$\sqrt{E}$ (SRIM) and Eq. 1.52 (MARLOWE)[b]
Unit depth	$\frac{1}{100}$ of the maximum range
Temperature	295 K [c]
Debye Temperature	115.08 K [c] [64]
Free Flight Path	0.25 $\mathring{A}$[e]
Simultaneous Collision	0.25 $\mathring{A}$[f]
Maximum impact parameter	$\sqrt[3]{N}$+X [g]
target structure	Amorphous CsI
Lattice Binding energy	6.3 eV [65]
Replacement Binding energy	0.6 eV
Displacement Binding energy	25 eV

[a] k is a coefficient from LSS theory [3], and E the kinetic energy of an ion.
[b] In MARLOWE, they use similar k$\sqrt{(E)}$ as the electronic stopping, but due to the different electron density in an atom, we should include local loss term in MARLOWE with a parameter α.
[c], [d] No need in SRIM, only for MARLOWE
[e] ,[f] No need in SRIM. The default value in MARLOWE
[g] The Maximum impact parameter is the range to fine a target. N is the mean volume of the unit cell, so $\sqrt[3]{N}$ means the mean distance between atoms. Empirically, when we add X to this value with a unit of $1/l(\mathring{A})$, where l means the unit cell size in a monocrystalline, the probability to fail to find a target decreases and the energy losses become similar with SRIM.

used. Since this binding energy loss process was not supplied in the original code of MARLOWE, we added them including the displacement criteria for MARLOWE to do similar works with SRIM 1.5.1. After this setup, we change only the target structure to study channeling effects with MARLOWE. The

next section will explain the target structure of CsI(Tl) and NaI(Tl) , and the relation to the channeling effect.

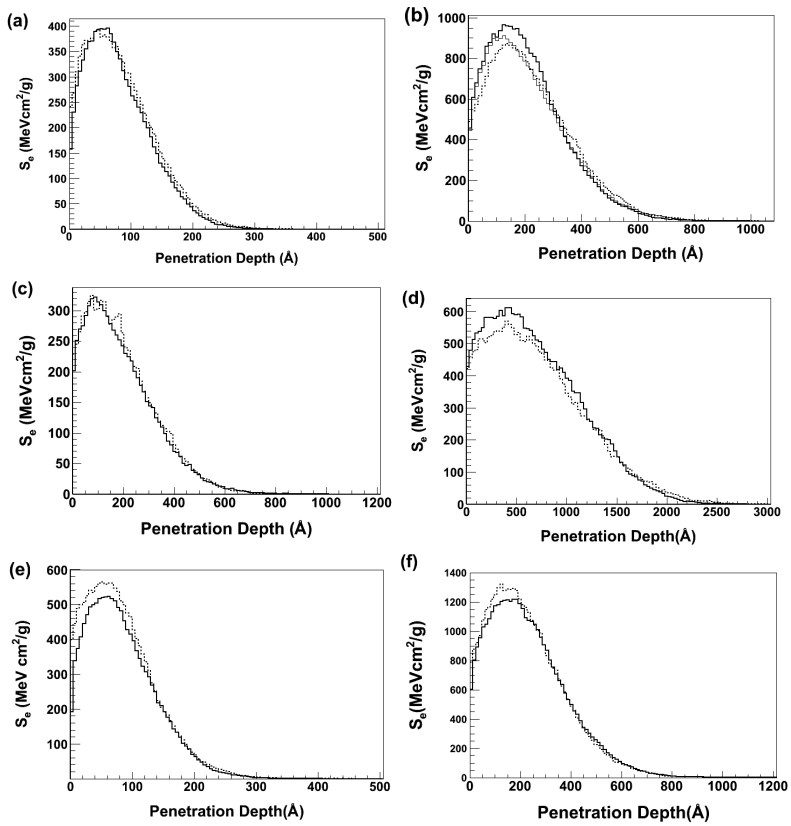

Figure 2.3: The comparison of the electronic stopping power distributions between SRIM and MARLOWE for 10 keV (a) and 50keV (b) Cs ions in CsI(Tl) , 10 keV (c) and 50 keV (d) Na ions in NaI(Tl) , and 10 keV (e) and 50 keV (f) I ions in NaI(Tl) . The α factors are 0.75, 0.75 and 1.0 for Cs in CsI, Na in NaI and I in NaI, respectively.

Table 2.2: Comparing the mean energy loss for 3 categories

SRIM	PhononE[a]	IonizationE	DamageE
Cs 10 keV in CsI(Tl)	6.4	2.4	1.2
Cs 50 keV in CsI(Tl)	30.6	13.7	5.7
Na 10 keV in NaI(Tl)	5.6	3.7	0.7
Na 50 keV in NaI(Tl)	21.6	25.2	3.6
I 10 keV in NaI(Tl)	6.1	2.83	1.07
I 50 keV in NaI(Tl)	28.7	17.2	4.8
MARLOWE[b]			
Cs 10 keV in CsI(Tl)	6.35	2.2	1.25
Cs 50 keV in CsI(Tl)	29.5	14.1	5.72
Na 10 keV in NaI(Tl)	5.54	3.47	1.13
Na 50 keV in NaI(Tl)	21.6	25.8	3.8
I 10 keV in NaI(Tl)	6.5	2.5	0.98
I 50 keV in NaI(Tl)	29.5	16.6	4.5

[a] All energies have a unit of keV.

[b] All are obtained from the mean value of each energy loss distribution.

2.2 Crystal structure formation

2.2.1 CsI(Tl) and NaI(Tl)

CsI(Tl) crystal is a cubic crystal, however, since each of Cs and I ion constructs its cubic and they overlap, the crystal looks like the body centered crystal(BCC). This kind of the alkali halide can have both of BCC and FCC, the face centered crystal, according to the ratio of the radius of a cation and an anion. If the ratio is from 0.73 to 1.37, then the molecule has a BCC structure with higher probability that that of FCC. If the ratio is outside of the range of BCC, then the probability to be a FCC structure is higher. That is why CsI(Tl) are mostly BCC crystals and NaI(Tl) mostly FCC crystals [66].

Table 2.3: Center positions for the open spaces in CsI(Tl) and NaI(Tl) [a]

CsI(Tl)	[111]	[001]	[110]	
	(0.408, 0.0, 0.0)	(0.5, 0.0, 0.0)	(0.354, 0.25, 0.0)	
NaI(Tl)	[110]	[001]	[111]	[-211]
	(0.17, -0.25, 0.0)	(0.25, 0.25, 0.0)	(0.204, 0.0, 0.0)	(0.14, 0.17, 0.0)

[a] These are used for the simulation of the channeling effect with external ions. And these are normalized distance by the length of a unit cell in each monocrystalline.

As mentioned in section 1.3, in BCC crystals, the most open axis is order of <111> - <100> - <110> and the most open plane {110} - {100} - {112} and for the FCC crystals, the most open axis and plane are in order of 100 - 110 -111. However, since the structure of NaI(Tl) is composed of ions with largely different sizes, the order is somehow different as <110> - <100> - <111> for the axis and {111} - {100} - {110} for the plane. Fig. 2.4 depicts the atomic arrays on the one of the most open axis,[110] in (a) and [111] in (b), and plane, (100) in (a) and (211) in (b). In this figure, we indicate the unit square and a plane pair in which ions undergo the channeling effect. The ions have the largest probability to be channeled at the center of the spaces, the positions of which are listed in Table 2.3.

2.3 The range and the critical angle for ions from outside

In order to test whether the MARLOWE, the simulation code, reproduces the channeling events well or not, its results are compared with the experiments for the range and the critical angle of incident ions in this section. After the comparisons, we discuss the suitability of MARLOWE for estimating the channeling effect for recoil ions in CsI(Tl) .

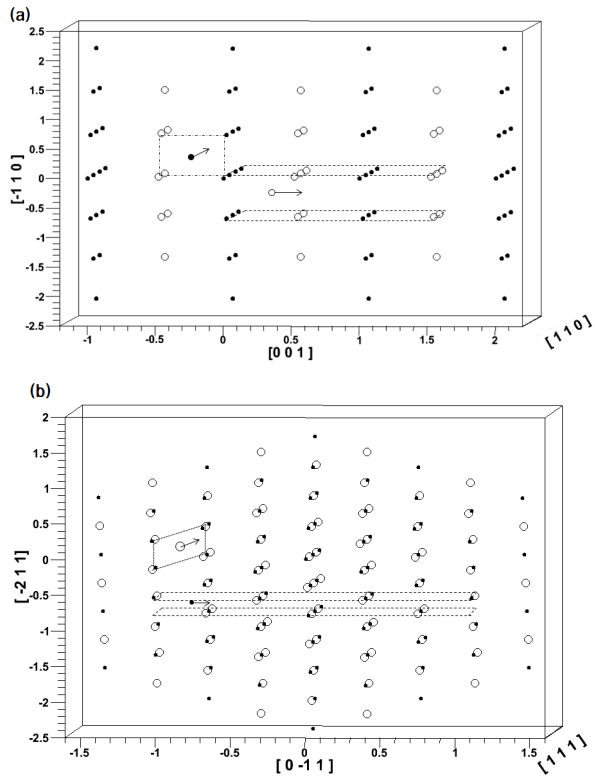

Figure 2.4: One of the views of CsI(Tl) (a) and NaI(Tl) (b) structures constructed in MARLOWE. In (a), filled points are Cs ions and open points are I ions according to the size of ions. A Cs ion enters an open space around [110] axis, and a I ion enter an interplanar space of [-110] plane. In (b), filled points are Na ions and open points are I ions. An I ion enter an open space around [111] axis and a Na ion enter an interplanar space of [-211] plane.

2.3.1 The range

Piercy *et al.* [67] injected $^{85}Kr^{+}$ radio isotopes into the amorphous Al_2O_3, polycrystalline Al and monocrystalline Al, while arranging directions of symmetry axes to be aligned along the incident beam to know the direction dependence of ranges. By measuring the amount of residual radio isotopes, $^{85}Kr^{+}$, with stripping the target crystal layer by layer electrochemically and

measuring the radioactivity for the remained crystal, they obtained the range distribution of $^{85}Kr^{+}$ in the target material. We reproduce those situations with MARLOWE by injecting ^{85}Kr ions in the direction of [110], [100], [111], and 7° tilted from [211] in a monocrystalline Al target and in an amorphous Al target. Fig. 2.5 shows the comparisons between the measurement in [67] and the MARLOWE simulation with default parameters. In this simulation, to fit with data, the incident ion beam, of which structure is $exp(x^3 \times log(cos(\triangle\theta)))$ is tilted by 2° and the beam divergence is ±20°. The results describe the dependence of the incident directions of ions on the depth distribution in the target material. The simulation shows the similar tendencies with the measurements, but the depth distributions are not exactly same.

There are detailed reports which describe the channeling behavior of boron injected to the monocrystalline silicon target [68][69]. In Ref. [68], boron ions of 20 keV are implanted in the directions of [100], [110] and [211], and parallel to (111) plane. In the binary collision simulation constructed by themselves, the ZBL potential and modified Oen-Robinson(OR) model were used, which are similar to our work, and a damage accumulation process was included, which contributes to fit to their measured data well. For the OR model, they modified α, which is the ratio of the nonlocal and local losses as a function of the ion energy, $y * E^q$, where y and q are fitting parameters for the case of B in Si. γ was changed from 0.3 to 0.05 and k to 1.5k in Eq. 1.52. For the damage accumulation, they calculated the number of point defects, a pair of a vacancy and an interstitial atom, with the modified Kinchin-Pease model and the stable number of point defects after the recombination taking account or pre-existed defects at the previous cascade. By placing the interstitial atoms around the lattice vacancies according to the surviving probability in the simulation, they included the damage accumulation effect. We also tried these mentioned modifications in MARLOWE for better fitted ranges shown in Fig. 2.5, the use of the energy dependent α and the damage accumulation. The damage accumulation is a choice in MARLOWE doing reduction of defects which is not one of the unpaired defect, the distant frenkel pair, the substitutional impurity and

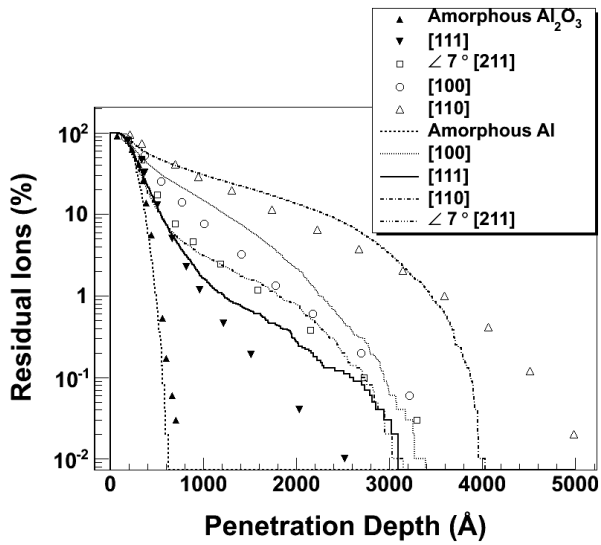

Figure 2.5: The residual concentrations of $^{85}Kr^{+}$ in the Al target according to ions incident directions. All simulation parameters are those in default.

the escaped defect and passing the surviving defects on the next event. In the modification, we used input parameters mentioned in section 2.1.1 for the energy loss to be similar with SRIM. However, the modifications did not show any significant change for the curves in Fig. 2.5, except it found that the tilt of 2° of target material was unnatural. The modified curves are in Fig. 2.6.

Therefore, we can not reproduce the experimental ranges for the channeling ions correctly. If we use only the local energy loss function, above the distance of $1.65 * a_u$ from the core, the electronic energy loss becomes lower than that we use the local + nonlocal loss [6]. But in that case, there is a problem that total energy loss decreases. So, we can conjecture that the local energy loss should be applied only for the channeling ions, not for normal scattering ions. Since there is no option for that in MARLOWE, we should study further to modify the code. However, our main purpose of this study is to reproduce the enhanced energy due to the channeling effect, we decide the local + nonlocal energy loss.

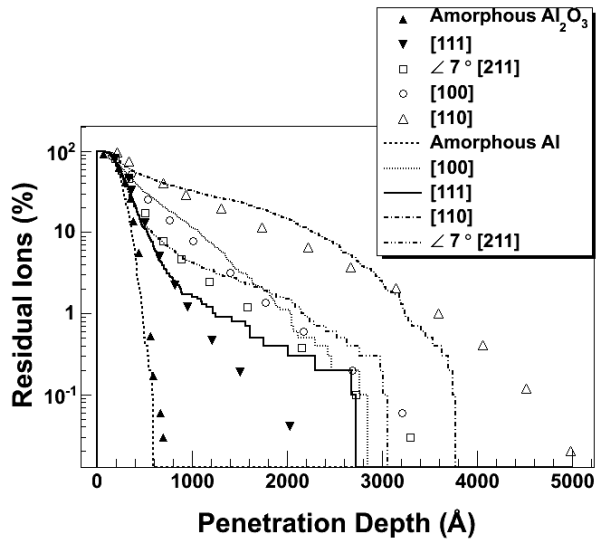

Figure 2.6: The comparison with the measurement of residual concentrations of $^{85}Kr^{+}$ in the Al target and the modified simulation.

2.3.2 The critical angle

The critical angle for the low energy range is obtained from Eq. 1.13. In the simulation, we reproduce the half angle in the procedure that we generate events with injecting ions along the symmetry axis with $\pm 20^{\circ}$ of the beam divergence, compare the range with that of amorphous target, select events of which ranges are above the maximum in amorphous target, and than fit the selected event distributions according to initial theta angles with Gaussian + constant fuction to obtain the FWHM angle. Fig. 2.7 shows the selected events with a Gaussian + constant fitting function. At first, the number of events in a theta bin are identical, but by the event selection, only events with larger ranges than that of an amorphous target remain. The reason to do the simulation with this method is to detect the number of events according to the angles from a symmetry axis or plane and get FWHM in that yield spectrum. But the criteria for the maximum range is artificial, because in the

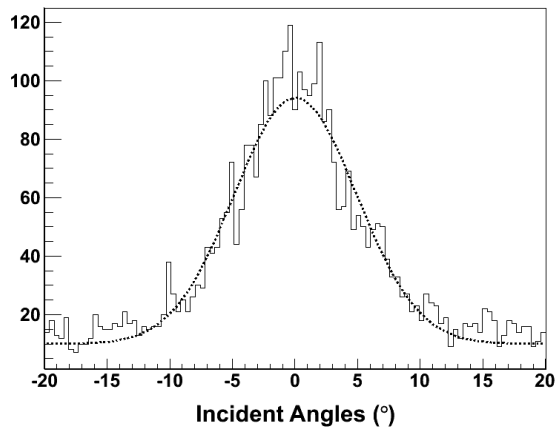

Figure 2.7: The selected events for each incident angle about a symmetry axis, [111], for 20 keV iodines in the CsI crystal and the Gaussian + constant fitting fuction

experiment, a thin target is used to detect escaping ions. Table 2.4 compares the calculated critical angles and the simulated ones with MARLOWE. Due to the different criteria for the half angle, they have about factor two difference. But in other way from [70], we estimate the critical angles again. Fig. 2.8 depicts the mean of range distributions per each angle about a symmetry axis for all events. As done by [70], if we define the critical angle is the difference of angles between two start points for the ranges to increase from the pedestal value, the simulated ones become similar with the calculated ones. By the way, the total energies to deposit to the electrons shows the same shape for the incident angle. This means that the range correlates with the deposit energy to electrons. Therefore, it is conjectured that E_{meas}, the light yield converted to the electron equivalent energy, from ions in a monocrystalline target implies the channeling effect. This will be explained in detail in the next section.The simulation for the half angle is done with default input parameters, and there is no significant deference with using others.

Table 2.4: Calculated characteristic angles and simulated half angles with MARLOWE [6]

(a) Axial angles for iodine ions in CsI.

	5keV	10keV	20keV	50keV
[111]	**12.7**	**10.7**	**9.0**	**7.2**
	6.8	5.3	4.9	4.2
[100]	**11.6**	**9.7**	**8.2**	**6.5**
	5.9	5.1	3.9	3.2
[110]	**8.9**	**7.5**	**6.3**	**5.0**
	4.0	3.6	2.7	2.7

(b) Axial angles for sodium ions in NaI.

[100]	**6.1**	**5.2**	**4.3**	**3.5**
	4.1	3.5	3.8	2.5
[110]	**6.7**	**5.7**	**4.8**	**3.8**
	2.6	1.6	2.0	0.9
[111]	**4.1**	**3.4**	**2.9**	**2.3**
	2.4	2.7	2.2	1.5

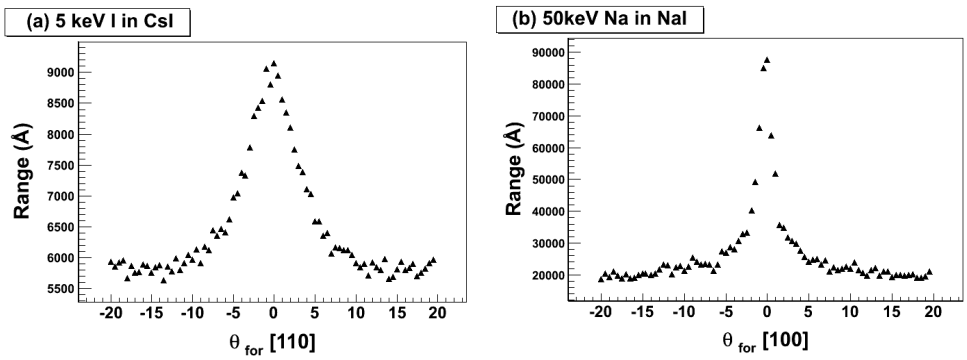

Figure 2.8: The range distribution for the incident angles of ions, which is that of 5 keV iodines about [110] axis in the CsI crystal (a) and that of 50 keV sodiums about [100] axis in the NaI crystal (b).

2.4 Reproduction of E_{meas}

Although the range of the channeling ion in MARLOWE simulation is not the same as data as shown in Fig. **??**, the angle dependence for it is well reproduced. The reduced range in the simulation for the channeling ion is due to its larger energy loss per a penetration depth from the nonlocal loss, however the total deposit energy for the ion would be conserved. So the comparing the electronic deposit energy for the channeling and nonchanneling case is possible in MARLOWE simulation. However, the measured one in the experiment using the scintillation crystal is not the electronic deposit energy but the measured energy, E_{meas}. So, we should know how the electronic deposit energy is transformed to E_{meas} and where in that spectrum the channeling effect emerge. E_{meas} is defined by $QF * E_{ion}$ as in Eq. 1.34. In other words, QF is the conversion factor from the incident energy to the measured energy or the scaled light yield in the scintillation detector. The higher the QF is, the higher the light yield is for a given energy. In QF, there are two categories, one is the nuclear quenching and the other is the electronic quenching. The former means the light yield is quenched by transferring the energy for a

target atom to recoil, and the latter is related to the scintillation efficiency of the target material for the electronic excitation density as mentioned in section 1.4.2. From the simulation, we obtain the energy loss and the stopping power by the phonon and damage creations and the ionization, so we deduce the nuclear quenching. For the estimation of the electronic quenching, we apply Birk's formula as a scintillation model to the deposit energy to convert it to the light yield. In this section, we reproduce E_{meas} in the monocrystalline and amorphous target with informations of the deposit energy and a scintillation model from an incident ion energy. With the E_{meas}, we obtain QF and the region of the channeling effect in that spectrum. By using the maximum E_{meas} in the amorphous target as a criteria for the channeling effect, we also estimate the channeling fraction for the isotropically radiated recoil ions. In the reproduction process, we use the input parameters for MARLOWE which make the energy loss in MARLOWE and SRIM to be same.

2.4.1 Scintillation model

Gwin *et al.* [58] had measured the scintillation efficiency for electrons, protons and alphas with various energies. The particles of those energies have different ranges of the stopping power, so the scintillation efficiency is represented as a function of it as Fig. 2.9. Since these particles have low atomic numbers and masses, they interact mostly with electrons and the electronic stopping power is dominant in the total stopping power. We use a modified Birk's formula, 1.29, of which parameters are 1.375 for the normalization factor, 1 for $k\alpha$, and 0.0038 for B' obtained by the comparison with Gwin's data. The reason that we use this curve for the scintillation efficiency, the electronic stopping power for Cs or I ion with tens of keV energy is similar with that of the alpha with few MeV energy in the CsI crystal, which is considered in Gwin's data as shown in Fig. 1.27. For the summed electronic stopping power, it is similar, which means the sum of the electronic energy losses per a unit depth of target for the primary and secondary ions and this is the one that we are interested in for reproducing E_{meas}. Since the nuclear stopping power of Cs or I is higher

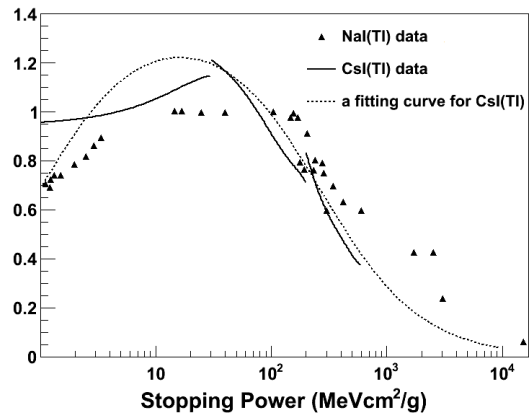

Figure 2.9: The scintillation efficiency for the stopping power for the electron, proton and alpha of various energies. The solid lines are from three particles in CsI(Tl) [58], the points are collected from other references for NaI(Tl) in [56] and the dashed line is our function, which is the fitted one to the Gwin's data with a modified Birk's formula.

than the electron stopping power, many secondary ions are generated in the cascade initiated by an ion and playing a role to deposit energy to the target again. Murray *et al.* [56] mentioned the possibility that the reason for making the scintillation efficiency increase to the discrete level for particles of high Z numbers is the generation of delta rays. Delta ray means the high energy electron from the core shell of the target atom. Due to its low stopping power, its range is large and the its deposit energy is not subject to the quenching from the primary ion.

2.4.2 Quenching factors and the channeling fraction

To reproduce E_{meas}, the first, we generate events with an ion from a lattice point as shown in Fig. 2.10, the second, divide the penetration depth along the initial direction into a unit depth as in Table 2.1 and calculate the summed electronic stopping power, and the third, apply Eq. 2.1 to obtain E_{meas} with an assumption that $\frac{L_{\gamma\ or\ e}}{E_{\gamma\ or\ e}}$ is 1.

$$E_{meas} = A \sum_{i=1}^{max.depthbin} \triangle E_{e,i}\ S(\frac{dE_{e,i}}{dx_i}), \quad (2.1)$$

where A is a normalization factor, $\triangle E_{e,i}$ is an electronic energy loss for i-th depth bin, and $S(\frac{dE_{e,i}}{dx_i})$ is a scintillation efficiency for the i-th summed electronic stopping power. The examples of E_{meas} distributions for the monocrystalline and amorphous targets and their fitting functions are in Fig. 2.11. From these we obtain the three informations, the quenching factor from $\frac{Mean\ of\ E_{meas}}{E_{initial\ ion}}$, the channeling fraction from the selection of events of which $Emeas$ is above the maximum E_{meas} for the amorphous target as shown in Fig. 2.12, and the fitting parameters to apply to GEANT4 simulation for comparing the results to our channeling experiment. The channeling fraction for each energy of Cs and I ion in CsI(Tl) is depicted in Fig. 2.13. The fractions are under 3 %, and from 5 keV, they are decreasing. This tendency is similar that the estimations from N. Bozorgnia *et al.* [2] and G. Hobler [69] due to the large critical distance comparable with the channel width. However, the values from this work are a little larger than that in [2], of which value around 100 keV is 2 % and around 1 keV is 0.1 % at the upperbound. We conjecture that this difference is due to the partial channeling with some dechannelings which can be reproduced only in the simulation.

The method in Eq. 2.1 is tested for alphas in CsI(Tl) crystal. Figure 2.14 shows alpha quenching factors of the measurement and the simulation. Since MARLOWE does not have the electronic energy loss model for ions above 25 keV/amu, we use only SRIM in this case. The summed electronic stopping power obtained from SRIM is the average value of each depth, because it is difficult to select the variable of our interest event by event in SRIM. In the data of R. Gwin *et al.* [58], only 7 μs of DAQ time window was used, which is somewhat small to measure the light yield of gammas with 662 keV in CsI(Tl) . Y. F. Zhu *et al.* [71] and T. Y. Kim *et al.* [72] used 12.5 μs and 25 μs, respectively. So we infer that the reduced light yield which they measured in the gamma calibration causes the enhanced E_{meas} and thereby, the quenching factor. After applying a factor of 0.93 to the process to obtain

the quenching factor, we can gather the data points on the same place. And then, we compare the reproduced quenching factors with them. Due to the discrepancies between the scintillation efficiency curves of the measured and our fitting function in Fig. 2.9, there is 3.7 % difference at 8 MeV of alphas.

Figure 2.15 depicts the reproduced quenching factors of Cs and I ions in CsI(Tl) and Na and I ions in NaI(Tl) by using SRIM and MARLOWE with other measurements. As mentioned above for alphas, we used the average value of the summed electronic stopping power from SRIM, however, that in event by event from MARLOWE. So the former represents the smooth curve for the penetration depth as Fig. 2.3, while the latter the fluctuated distribution. Since the more the deposit energy is concentrated on a region, the less the light yield due to the characteristic of the scintillation efficiency curve in Fig. 2.9, we conjecture that the quenching factor from SRIM is overestimated. For NaI(Tl) , the same scintillation efficiency curve with CsI(Tl) is used just to test our method. If there is the measured scintillation efficiency curve for NaI(Tl) , the more correct quenching factor can be achieved. The input parameters for NaI(Tl) is in default with no significant change for the results from using other parameters. The initial moving angles of ions are set to be isotropic within $\pm$ 20°, since MARLOWE sometimes fails to find target atoms over the angle.

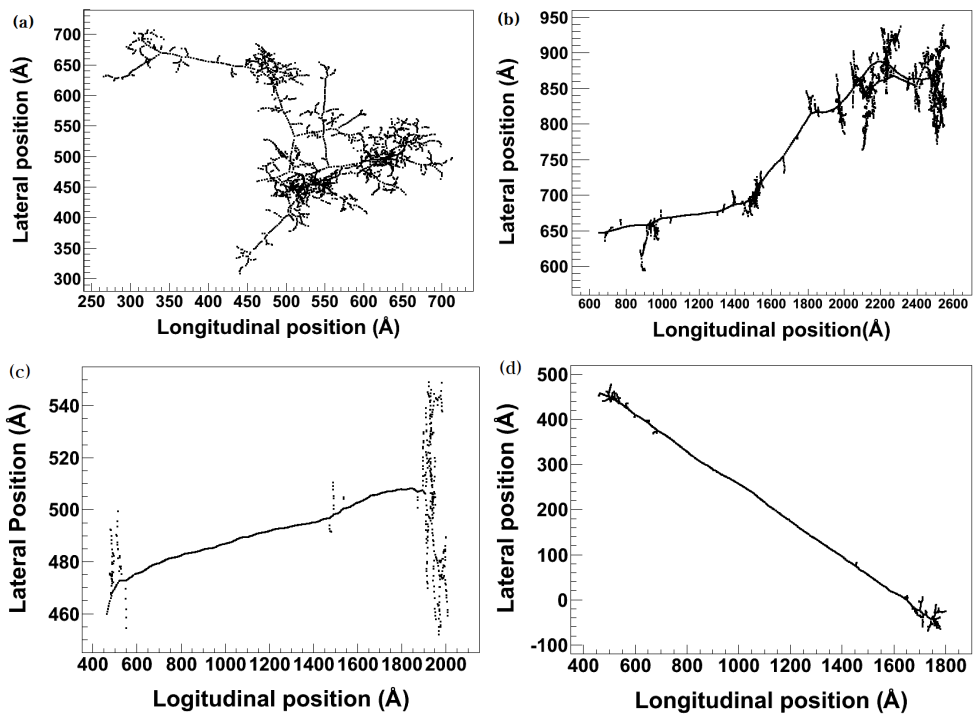

Figure 2.10: Tracks generated by an iodine and a sodium recoil ions of 50 keV in CsI(Tl) (a) (c) and NaI(Tl) (b)(d), respectively. (a) and (b) are the nonchanneling events, and (c) and (d) are the channeling events.

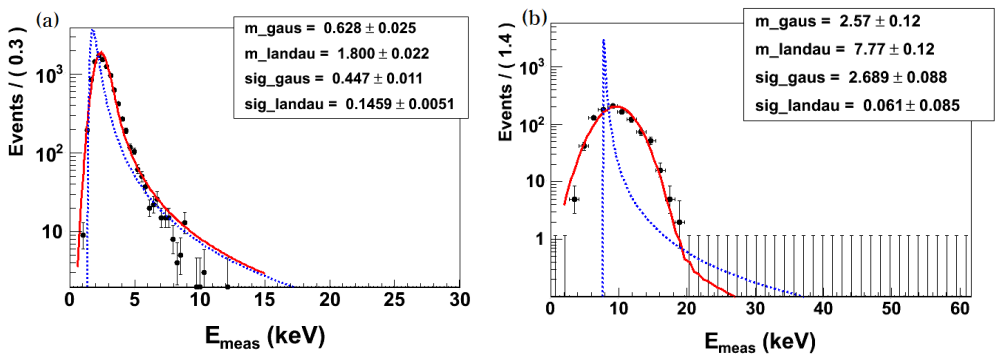

Figure 2.11: The E_{meas} distributions reproduced with MARLOWE for the monocrystalline (a) and amorphous targets (b) and their fitting functions of the Landau-Gaussian convolution from Roofit package in ROOT [39]. The sharp peaks in the background are the Landau distributions. (a) is for Cs ion in CsI(Tl) with 30 keV, and (b) with 140 keV.

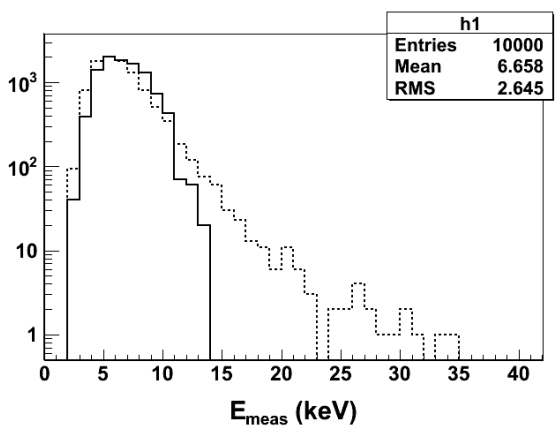

Figure 2.12: The comparison of E_{meas} for Cs ion with 90 keV in the monocrystalline, the dashed line, and amorphous CsI(Tl) crystal, the solid line. Above the 14 keV, the maximum energy for the amorphous target, events are $\sim$ 3 % in the monocrystalline target.

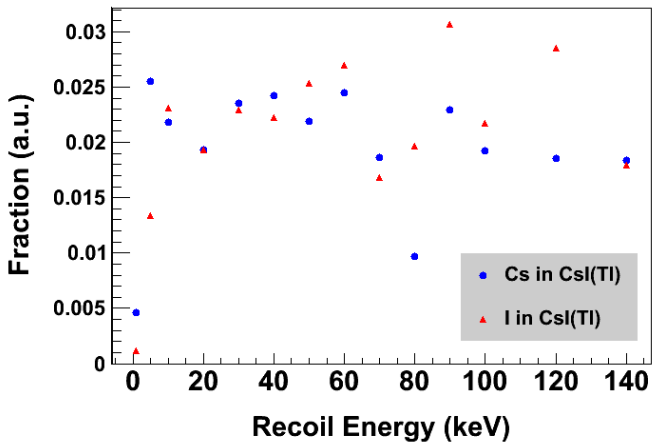

Figure 2.13: The channeling fractions for Cs and I ions in CsI(Tl) , which are all under 3 %.

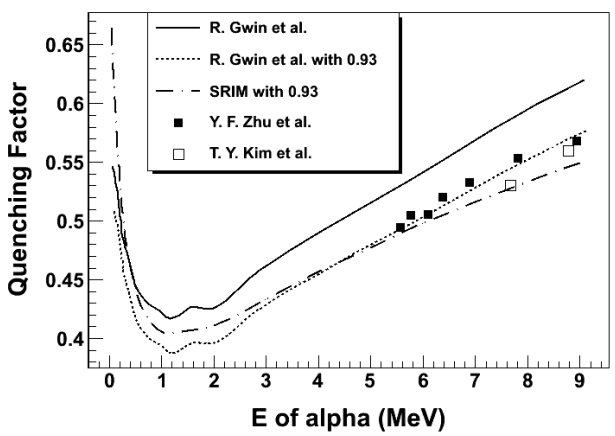

Figure 2.14: The reproduce quenching factors of alphas in CsI(Tl) with SRIM and the measurements of R. Gwin *et al.* [58], T. Y. Kim *et al.* [72] and Y. F. Zhu *et al.* [71].

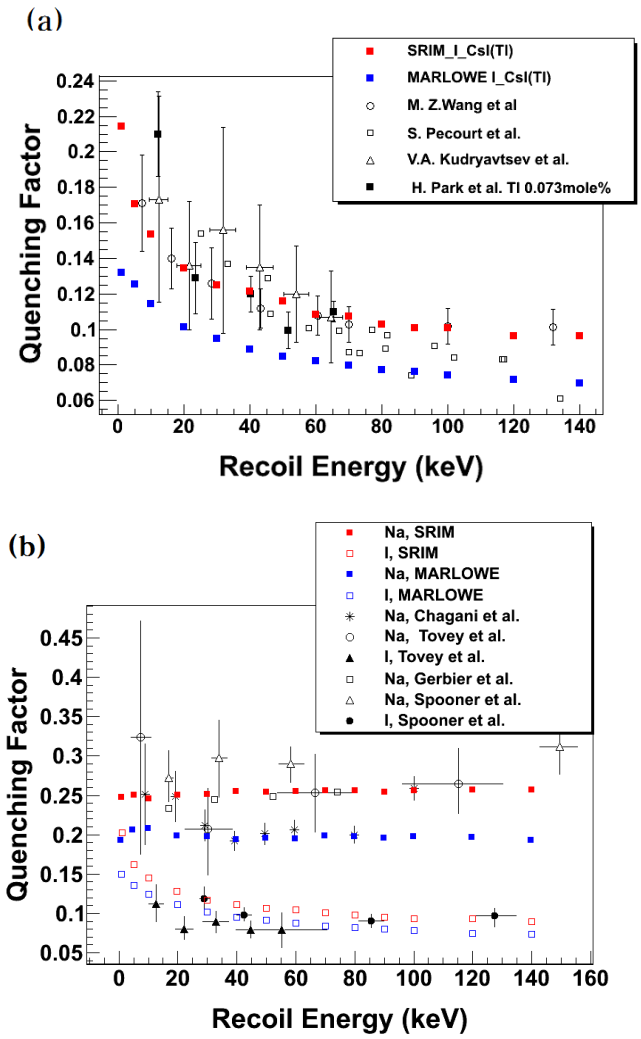

Figure 2.15: The reproduce quenching factors of Cs and I ions in CsI(Tl) (a) and Na and I ions in NaI(Tl) (b) with SRIM and MARLOWE and the measurements. Data are from M. Z. Wang *et al.* [73], S. Pécourt *et al.* [74], V. A. Kudryavtsev *et al.* [75], and H. Park *et al.* [76] for CsI(Tl) (a) and H. Chagani *et al.* [77], D. R. Tovey *et al.* [78], G. Gerbier *et al.* [79], and N. J. C. Spooner *et al.* [80] for NaI(Tl) (b).

3 Experiment

3.1 Goal of this experiment

In order to measure the channeling and blocking effect in our crystal, we make the directions of recoil ions induced by the neutron-nucleus scatterings to be aligned along one of the symmetry axis or plane in the experiment. The setup is similar with the KIMS neutron calibration experiment, because we use neutrons and neutron detectors to measure the scattered neutrons in the CsI(Tl) crystal. However, for the discrimination of recoil directions, we should put the neutron detectors far from the CsI(Tl) detector to reduce their solid angles, and have a monocrystalline CsI(Tl) crystal.

In the experiment, we expect that we measure the different E_{meas} spectra in the CsI(Tl) crystal when we select events tagged by different neutron detectors, which have the same scattering angles but different azimuthal angles on the bottom plane of a cone in Fig. 1.30 due to the channeling or blocking effect. By comparing the results with the reproduced E_{meas} from MARLOWE and GEANT4 with considering the equivalent setup, we test our scintillation model and the estimation for the channeling and blocking effect. If the experimental results agree with the expectations, we apply the reproduced E_{meas} for composing the expected E_{meas} spectrum induced by WIMP-nucleus scattering and then estimate the change of the cross-section limit of WIMPs. In the next two section, we introduce our experimental setup and the energy calibrations for detectors, and show the method of the coincident event selection and the coincident event rate.

3.2 Setup and calibration

3.2.1 CsI detector

The test crystals of CsI(Tl) are all cut crystals from large ones used in Y2L, of which dimension is 30 × 30 × 14 in unit of mm. For being safe from the external contaminations of the crystals from Rn gas in the air and radiation damages from cosmic ray and neutrons in the calibration experiment, the large crystal cannot be used to measure its quenching factor with our setup. However, from the comparisons of the responses to 59.54 keV gamma of ^{241}Am source and to 5.9 keV x-ray of ^{55}Fe source [13] [34], we assume that the small and large crystal are identical in the radiation response.

X-ray diffraction measurement

We measured the three planes of each CsI(Tl) crystal by X-ray diffraction(XRD) measurement which is requested to Center for Materials Analysis in Seoul National University. Figure 3.1 shows the 2θ results for 5 different CsI(Tl) crystals. Except Fig. 3.1 (e), they show many peaks which mean the crystals are polycrystalline or, no significant peak which means the planes are nonsymmetry. For 0609B crystal, there are three peaks only in one plane, of which angles are 27.6°, 57°, and 91.4°. These represent (110), (220) and (411) for each plane and that the 0609B crystal had grown to be monocrystalline well. However, the other planes show no peak, this implies the crystal was cut along the plane of nonsymmetry, but the probability to be monocrystalline is larger than those with many peaks. Crystals are usually grown along a [110] or a [111] axis. So (110) plane of 0609B might be obtained by the cut in parallel with crystal growing direction. Thereby we use the 0609B for the measurement of the channeling and blocking effect with aligning the [110] which is the normal vector of the (110) plane to the one of the recoil directions.

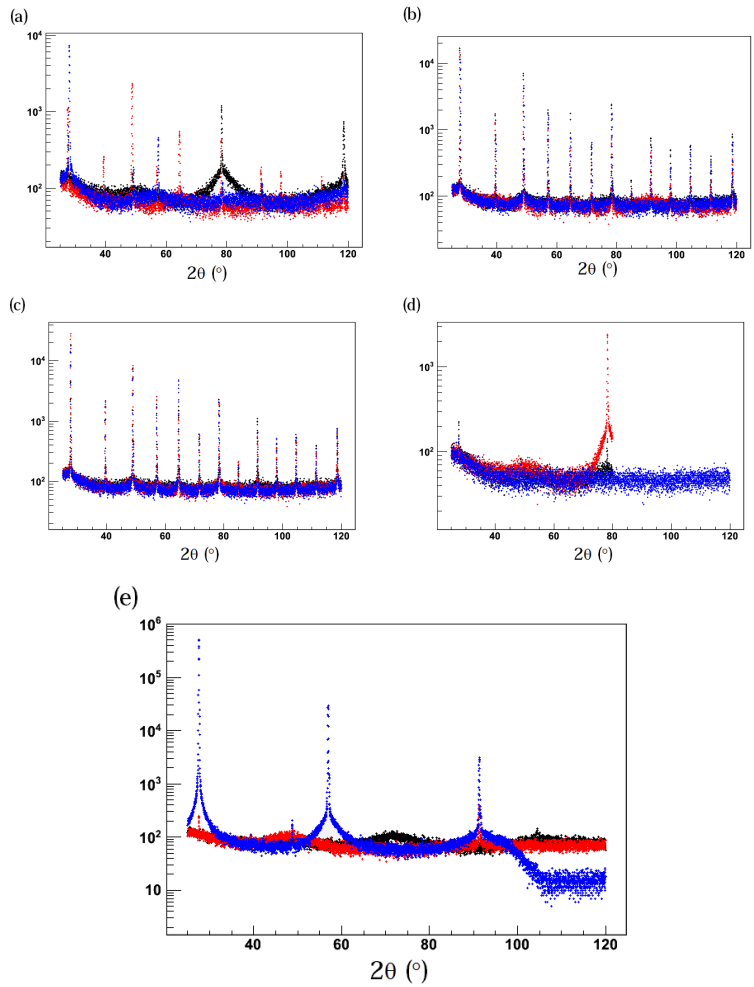

Figure 3.1: X-ray diffraction measurements for the CsI(Tl) crystals, which are cut from large ones which are in Y2L, 0605B (a), 0607A (b), 0607B (c), 0610B (d) and 0609B (e). The three different colors represent 2θ distribution of each plane of the crystal.

Energy calibration with gammas and electrons

In order to convert the light yield of the scintillation detector to E_{meas} , which is the electron equivalent energy, the energy calibration is important.

Table 3.1: Miller index subjected to 2θ in XRD measurement for CsI(Tl) [a]

$2\theta^{\circ}$	d$\mathring{A}$[b]	Intensity	h	k	l
27.593	3.23	100	1	1	0
39.419	2.284	20	2	0	0
48.789	1.865	35	2	1	1
56.973	1.615	18	2	2	0
64.426	1.445	8	3	1	0
71.463	1.319	4	2	2	2
78.227	1.221	10	3	2	1
84.822	1.142	2	4	0	0
91.364	1.077	6	4	1	1
97.888	1.022	4	4	2	0
104.529	0.974	20	3	3	2
111.424	0.932	2	4	2	2
118.627	0.896	4	5	1	0
134.916	0.834	2	5	2	1
145.072	0.808	2	4	4	0

[a] From 2010 International Center for Diffraction Data supplied by the technician in the center for materials analysis.
[b] the interplanar distance.

We usually use 59.54 keV gamma from ^{241}Am for this calibration, however, there are reports about the nonlinearity in CsI(Tl) [25][58][79][81], we add gammas and electrons of various energies to the scintillation measurement. Figure 3.2 depicts E_{meas} of various gammas in our calibration and Table 3.2 represent E_{meas} and their proportionality. For ^{241}Am , we overlap the reproduced E_{meas} and incident x-rays obtained from GEANT4 simulation, of which detector scheme in Fig. 3.6, with the measured spectra. The incident x-rays are emitted from ^{241}Am decay source. For reproducing E_{meas} , we applied the resolution of the measured energy, $0.015/\sqrt{(E)}$, to the deposit energy in

the simulation. From these results, we can state that the gamma responses of CsI(Tl) is linear from 10 keV to 100 keV for the gamma energy. W. Mengesha *et al.* [81] argued that the nonlinearity of gamma response in CsI(Tl) is due to the electron response, which is based on the measurement. When Cs or I absorbs energy from gamma, if the energy is higher than K or L shell binding energy of the electrons of them, the atom emits several electrons having some part of the absorbed energy as the following :

$$E_\gamma \;=\; \Delta(E_{b,K} - E_{b,L}) + \Delta(E_{b,L} - E_{b,M}) + \alpha \;, if \; E_\gamma > E_{b,K}, \qquad (3.1)$$

where the first term and the second term is the difference of binding energies of two shells, $\sim$ 30 keV and $\sim$ 5 keV, respectively, and we called the electrons emitting with these energies from the atoms Auger electrons. The last term, α, is the remained energy after subtraction of the sum of the first and second terms from E_γ. This equation will be changed in the case of $E_{b,L} < E_\gamma < E_{b,K}$ into that without the first term. W. Mengesha *et al.* [81] argued according to the sum of an electron response of each energy term the light yield is determined. Since the first and second terms are almost mono energies, these terms play roles of the pedestal and the fluctuation of the gamma response depends on the response for α. Figure 3.3 (a) and (b) show the electron and gamma response in CsI(Tl) respectively, which are measured by ourselves and W. Mengesha *et al* [81]. For the experiment of the electron response will be described in detail in the latter half of this section. Two graphs that we measured are normalized with 1.1, the ratio of light yields between 59.54 keV and 662 keV gammas in our measurement, since we did the energy calibration with 59.54 keV gamma and W. Mengesha *et al.* with 662 keV gamma. By the way, our measurements are different from those of W. Mengesha *et al.* below 30 keV, there is an increasing region with decreasing energies below 10 keV in the electron response and no fluctuation between 10 keV to 60 keV in the gamma response. This should be studied further. The decreasing region below 20 keV in the gamma response should be also studied, however, the surface effect of low energy x-rays should be considered carefully, which makes the light yield decrease by the interaction of x-rays at the surface. We estimate

the nonrpoportionality of CsI(Tl) for the response to the calibration source of electrons or gammas, is within ±10%, however, the low energy characteristics will be investigated further. For the calibration data, we also measure the time characteristics for the pulse shape discrimination. We will use the results to compare with that of nuclear scattering events and their channeling events. Figure 3.4 shows the Log(rmt10), which means that the mean value for the logarithmic mean time of signals within 10μs time window. There are two lines in the Log(rmt10) distributions for the E_{meas}, which are leaded by the Compton scattering electrons, the upper one, and x-rays and gammas from ^{241}Am , the lower one. For other gammas from ^{109}Cd and ^{57}Co in Fig. 3.4 (b), Log(rmt10)s are in the lower line if E_{meas} are due to their low energy gammas, and in the upper line if due to the Compton scattering electrons from high energy gamma background. It tells that if there are scintillations induced by electrons, Log(rmt10) are larger than that induced by photons. Figure 3.5 are comparing the Log(rmt10) distribution for the electron and photon at each E_{meas} bin. The distribution for the electrons are placed at the right side from that for photons. Photo-electric effect makes incident photons to be divided into low energy electrons in CsI(Tl) as we mentioned with Eq. 3.1, however, one of the Compton scattering makes only one electron. So for the same incident energy, two scatterings makes different number of electrons. Since the lower the electron energy, the larger the stopping power, low energy photons may cause the shorter mean times than electrons at the same energy. This argument will be confirmed in the future and this study will be important to estimate the pulse shape for the channeling events.Another strange thing is Log(rmt10) under 10 keV for ^{241}Am with a teflon reflector and a VM2000 reflector, which are used to wrap the CsI(Tl) , show different distributions. ^{241}Am source cannot produce photons under 10 keV, so Log(rmt10) in those energies should be similar with that of the Compton electrons by high energy backgrounds like the ^{241}Am with teflon in Fig. 3.4(a). When we see Log(rmt10) induced by ^{55}Fe , there is no difference between using teflon or VM2000. So the lower Log(rmt10)s of ^{241}Am with a VM2000 can be interpreted that low

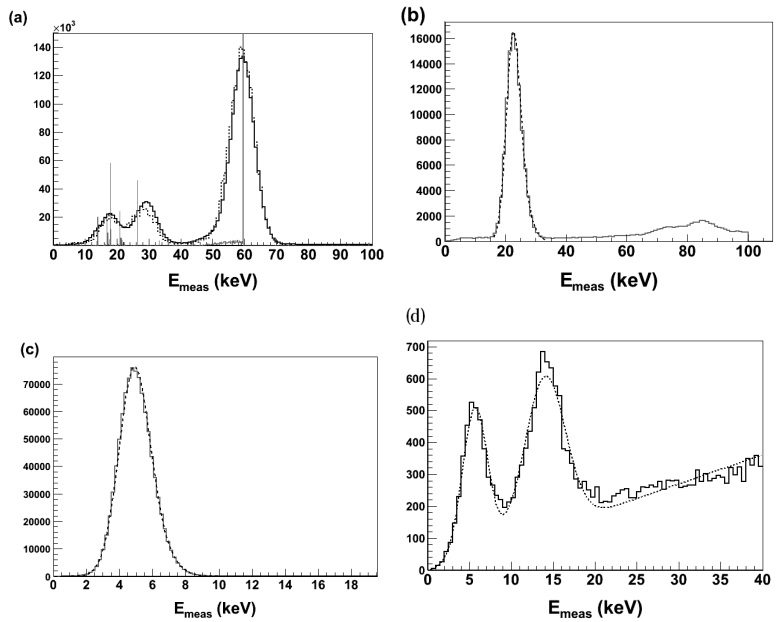

Figure 3.2: E_{meas} of various gammas with a CsI(Tl) crystal, which are from ^{241}Am (a), ^{109}Cd (b), ^{55}Fe (c), and ^{57}Co .

energy photons and electrons can penetrate VM2000 more than teflon. One possible reason is that VM2000 has the thickness of 64 μm which is used with 75μm teflon tape for the tightening, while two layers of teflon has that of 200 μm and the escaping photons or electrons from the reflector can enter the CsI(Tl) crystal more through the thiner material. Another probability of the fast scintillation of VM2000 itself is also in study [82].

We also measure the electron response of CsI(Tl) , since there is a non-proportionality in the low energy gamma response and thereby, the energy calibration with gamma has somehow uncertainty. We use the Compton scattering electrons as the source, and the gammas generating the Compton scattering are 661.6 keV of ^{137}Cs source. We detect the scattered gammas by the Ge detector, and from E_{meas} of them after the calibration, we estimate the electron energies in CsI(Tl) . Figure 3.7 shows the experimental setup. We make coincident signals between CsI(Tl) and Ge detectors to use them as the

Table 3.2: Measurement of the scintillation efficiencies of CsI(Tl) according to various gamma energies.

source	$E_{gamma}(keV)$	E_{meas} (keV)	Scintillation efficiency(a.u.)[a]
^{241}Am	17. 8	18	1.01
	59.54	59.54	1.
^{109}Cd	22.1	22.4	1.01
	25.	25.4	1.01
^{55}Fe	5.89	4.86	0.83
	6.49	0. 94	0.94
^{57}Co	6.4	5.64	0.88
	14.4	14.0	0.97

[a] All are normalized by the ratio of light yields and 59.54 keV.

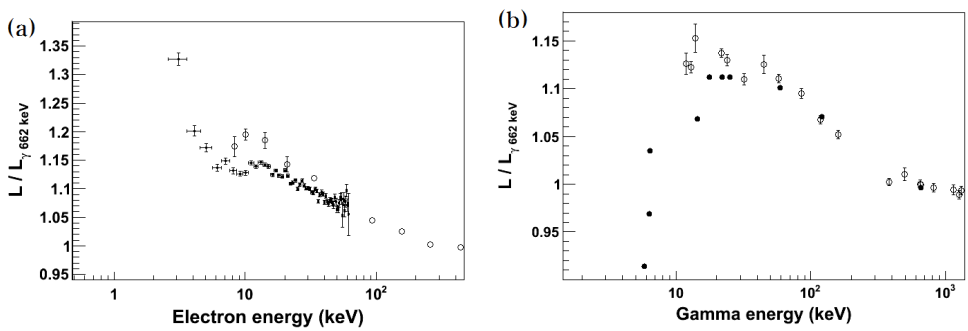

Figure 3.3: The electron (a) and gamma (b) responses in CsI(Tl) from measured by ourselves, the dots in (a) and the filled circles in (b), and by W. Mengesha *et al.* [81], the open circles in (a) and (b).

external trigger. The energy resolution of Ge detector is 2.9 keV in Fig. 3.9 (a), and 3.9 keV in Fig. 3.9 (b) at 661.6 keV due to our slow ADC module, and that of CsI(Tl) detector is 8.5 keV in FWHM at 59.54 keV due to the intrinsic resolution. E_{meas} in the calibration of Ge detector is depicted in Fig. 3.8 The two dimensional measured energy plot for the coincident events are in Fig. 3.9.

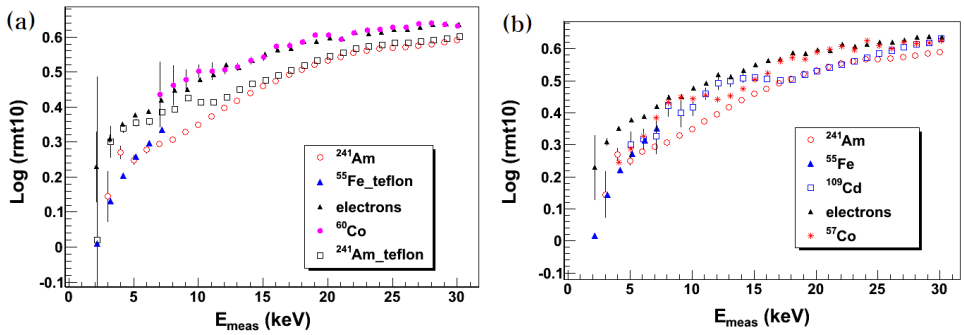

Figure 3.4: The Log(rmt10) vs. the initial energy of the electron and gamma, There are two lines in Log(rmt10) distributions. The upper line is relevant to the Compton scattering electrons by high energy gammas, and the lower line to the low energy gammas to generate the photo-electric effect in the target material. The name with "teflon" means that the CsI(Tl) crystal is wrapped by teflon and that without it by "VM2000".

When we compare the event rates with or without a gamma source, the rate with source is about 20 times higher, so we can say that events in the plot are mostly generated by ^{137}Cs gammas. In Fig. 3.9, the events of upper region from those of strongly correlated are random coincident events between two detectors because the sum of the energies is larger than the incident gamma energy. We use a cut of E_{meas} over 660 keV not to include random coincident events, thereby the energy threshold in CsI(Tl) becomes 1.6 keV. The sum of two E_{meas} for the strongly correlated event is in the range from 650 keV to 670 keV. The reason that the sum is not the exact 661.6 keV is the problem of the energy resolution. If there are partial energy depositions both of two detectors, the events are on the random positions under the correlated region in the figure. The electron response in the CsI(Tl) crystal from this measurement is in Fig. 3.3(a).

In this CsI(Tl) calibration, we used event selection cuts. Two cuts are same with those applied to the nuclear recoil event in the channeling experiment, which are (5) and (8) of Table 1.2 and will be explained in section **??**

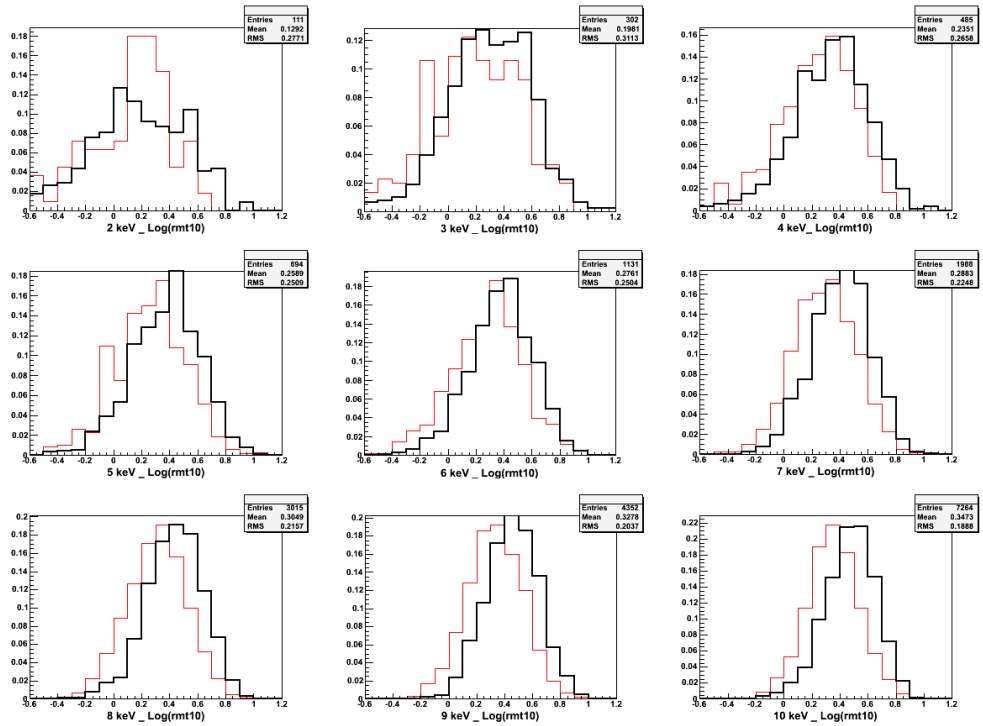

Figure 3.5: The Log(rmt10) distributions of electrons and gammas et each E_{meas}. The thick dark line is for the electrons and the thin light line for gammas.

in detail. The biggest cluster cut in (1) of Table 1.2 in order to remove some abnormal events which shows similar energy and decay time distribution in all of gammas and electrons in the calibrations experiment, which are in study in KIMS [82] and Fig.3.10 shows the effect of the cut. The abnormal events can be divided into two regions. One is under 2keV in E_{meas} with a broad decay times and the other is a broad island between 2 to 10 keV with very fast decay times. These are not from the full energy depositions from gammas and electrons but usually exist in the calibration data to distort the energy spectrum and decay time spectrum. We obtain the consistent decay time spectra of Log(rmt10) with this cut, as shown in Fig. 3.4 for the calibration data,

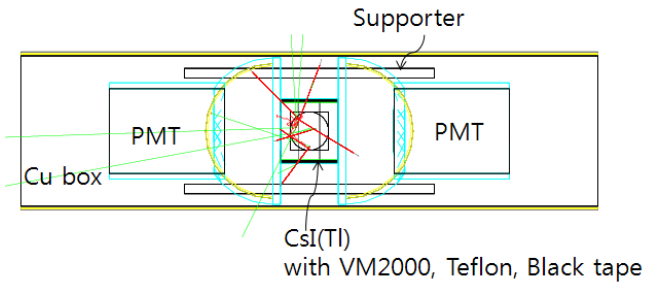

Figure 3.6: CsI(Tl) detector structure constructed in GEANT4. In both side of CsI(Tl) , there are a 2 PMTs, and the crystal is wrapped by a VM2000 reflector of 64 μm, a teflon tape of 0.5 mm, and a black tape of 0.15 mm. This PMT attached CsI(Tl) setup is tighten up with helps of 4 supporters made of SUS and 2 planes. These are all inside of copper box, where there is a hole to accept radiative sources for the calibration.

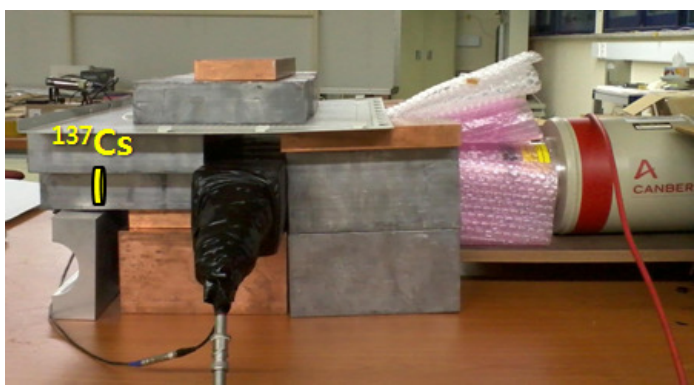

Figure 3.7: The electron response measurement setup of csi and Ge detectors which is established in the nuclear physics experimental laboratory in Seoul national university.

however, since it removes most of low energy events under 2 keV and this is the range of E_{meas} in neutron scattering events, we decide not to use it in the channeling experiment. It will be explain in section. 3.3.1 in detail.

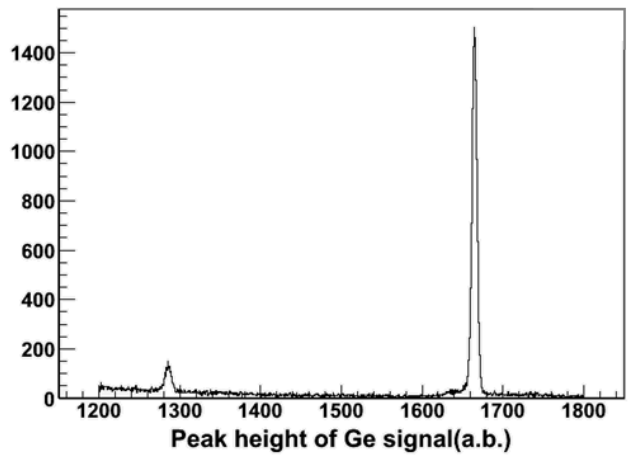

Figure 3.8: The Ge detector calibration with ^{22}Na and ^{137}Cs sources of 511 keV and 661.4 keV. The difference between two peaks are used to obtain a linear function about the ADC value.

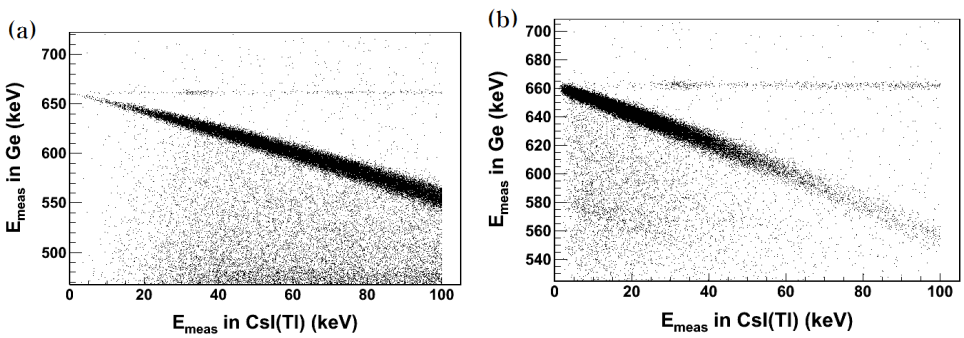

Figure 3.9: The two dimensional detected energy plot for the coincident events between CsI(Tl) and Ge detectors. The inclined and correlated events are of our interest since, the sum of E_{meas} is around 661.6 keV of ^{137}Cs gamma. (a) is obtained with the larger solid angle for the Ge detection, and (b) with the smaller solid angle, so the event rate of the low energy increases with (b).

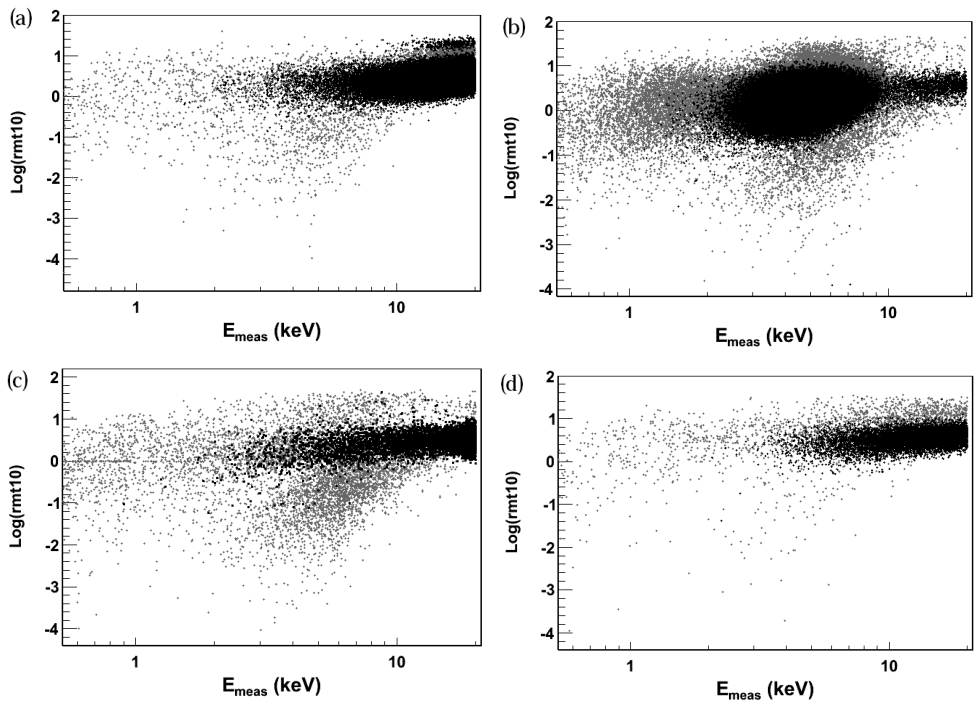

Figure 3.10: The effect of the biggest cluster cut in two dimensional plot of Log(rmt10) and E_{meas} for ^{241}Am (a), ^{55}Fe (b), ^{109}Cd (c) and Compton scattering electrons(d).

3.2.2 Neutron detector

BC501a and the detector design

In order to detect neutrons which scatter off the nucleus in CsI(Tl) , we set up neutron detectors at certain scattering angles. These are made of BC501a, the name of the liquid scintillator, which has the highest discrimination power for the neutron and gammas. However, It has the flash point at 24 °C, and it is toxic and volatile. Besides, it is easily oxygenated and denatured, when the sealing of its bottle is not enough. So the protection of its leakage is most important thing in terms of the safety and the discrimination power. The prototype of our detector has an auxiliary bottle for more containing of

BC501a, which can reduce the loss of light induced by the nitrogen bubble which is usually needed to prepare the expansion of the scintillator. Since the emission spectrum of BC501a has the maximum value at 425 nm, which is similar with the wavelength of maximum quantum efficiency of PMT, and the light output is 75% of the anthracene, if we can remove the nitrogen bubble, the light yield increase much. The reason to make the scintillation yield worse is the refractive index of 1.505 in average and 1.530 at 425 nm different from the nitrogen bubble of 1. But welding was a hard work, so the scintillator easily vented itself and the color turned to yellow, which means the oxygenated. So our final detector shape is simple, easy to rock, and with nitrogen bubble. The design of the bottle in Fig. 3.11. Figure 3.12 shows the process of bubbling, which means the deoxygenated process in the high pressure condition with only nitrogen and with an incandescent lamp to blow out oxygens and vapors. We did the bubbling with a level for BC501a to be fluctuated violently in the sealed glove box for more than 2 hours. We make 8 identical detectors to set at same scattering angle in order to obtain more statistics with detectors having narrow solid angle and compare E_{meas} between neutron tagged events by each of them. The attached PMTs and the high voltages for the neutron detectors are listed in Table 3.3.

Energy calibration

For the energy calibration of these detectors, we measure the Compton edge of ^{137}Cs with them. Due to large activity of the source which contributes double scattering events and the scintillation yield change depending on the tilt angles, which is relevant to the bubble area attached to the PMT, we put them on a place of 20 cm far from the source with standing it in upright position. The module which we use for the conversion of analog signals to digital signals(ADC) saves the electronic current, which is converted to the voltage in the module, with a 10 bit(2^{10} = 1024) memory, therefore the available range for detection of E_{meas} is under 1 V, when we set 1 bit as 1 mV. In order not to lose some part of energy of the Compton edge due to the

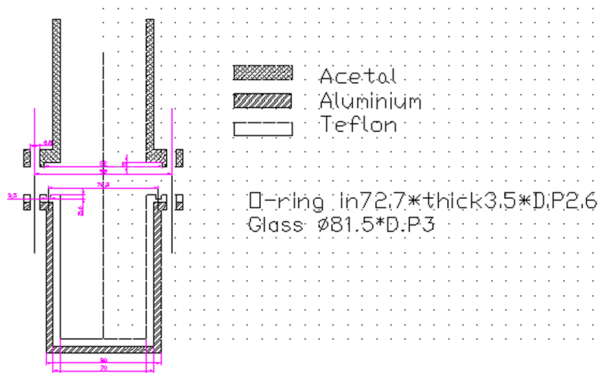

Figure 3.11: The neutron detector design. We modified the material from aluminum to stainless steel(SUS) due to its shielding of x-rays and its hardness. In addition with this, we use a quartz glass for the window to the PMT and an O-ring for the sealing, which is strong to the volatile solvent.

saturation, we modify the power of each PMT to the optimum value. Since the saturation starts when E_{meas} is over 0.45 in ADC sum, which has a linear correlation with the biggest height of the electronic pulses, we set the power for the ADC sum to be in the range from 0.35 to 0.45 as Table 3.3 with considering

Figure 3.12: The bubbling process in Y2L.

Table 3.3: Photomultiplier tubes used for the neutron detectors[a]

Name	Part number	ALS[b](A/lm)	ADC[c](nA)	HV[d](V)	Peak[e]
ND1	RD5404	427	0.42	2103.4	0.380
ND2	RD5405	596	1.2	1979.8	0.387
ND3	RD5101	892	1.5	1436.4	0.432
ND4	RD5267	248	0.52	1661.6	0.328
ND5	RD5415	478	1.5	1541.8	0.354
ND6	RD5419	336	1.7	1613.5	0.380
ND7	RD6247	744	3.3	1981.4	0.406
ND8	RD6250	863	3.0	1939.4	0.388

[a] All are the model of H6410 and R329-02 manufactured by HAMAMATSU [83].

[b] Anode Luminescence Sensitivity

[c] Anode Dark Current

[d] The used high voltage of each PMT

[e] The peak position near the Compton edge in ADC sum distribution

the energy resolution simultaneously. Figure 3.13 depicts how the ADC sum is scaled to be an energy in the unit of keV by using GEANT4 simulation. The obtained data and MC data for gammas in the neutron detector are fitted by applying an inverse scaling factor(1/keV) and an energy resolution which are changed in step by step. We choose the values when the chi square of that fitting is the smallest. From this we can find where the Compton edge, 477.3 keV, is placed in data. These parameters are used for the simulation of our experimental setup which will be explained in section 3.3.2. The data obtained from the gamma source are used also for the pulse shape discrimination for gammas and neutrons as a gamma reference. The separation of neutrons and gammas in the analysis are presented in the next section.

Pulse shape discrimination(PSD) of the neutron detectors

In this kind of neutron scattering experiment, the pulse shape discrimination power is most important to prove that the events are induced by neutrons. BC501a that we use was bought in 2001 with contained in two stainless steel drum. The power of our detector is decreasing every time we open the drum. However, with bubbling in the nitrogen condition, the power becomes the level of available. We examine the PSD power for the previous used detector, of which dimension is ϕ 8 $\times$ 6 containing the fresh material and for the new manufactured one, of which dimension is ϕ 6 $\times$ 10. Figure 3.14 depicts the comparison of the PSD values, the biggest height/the charge sum for the signal, between two detectors. The larger the distance between two peaks from the neutron induced events and gamma induced events, the higher the confidence for the neutron event selection. Due to the deoxygenation and the larger depth of the dimension, the new one shows a little closer peaks. So the stronger event cut is needed for the neutron event selection which is presented in section 3.3.1.

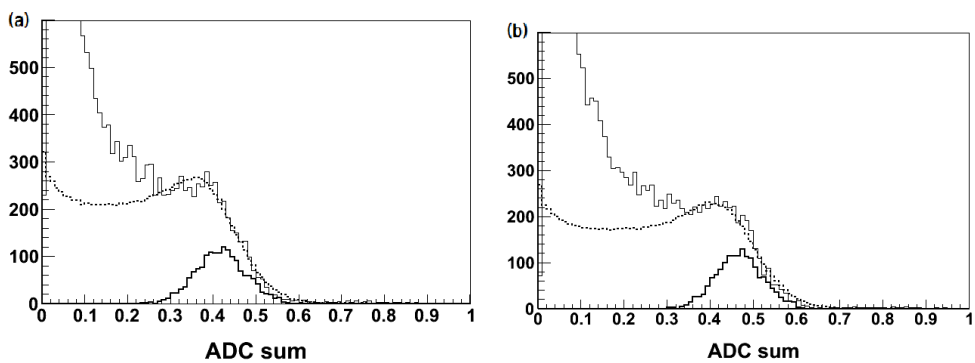

Figure 3.13: The energy calibration of ND1(a) and ND3(b) listed in Table 3.3. The dashed line is the fitted MC data and a thick line represents the E_{meas} distribution for Compton edge events, and a thin line shows the data.

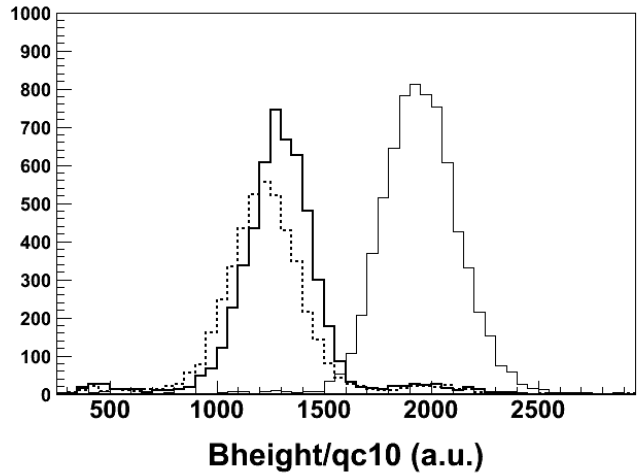

Figure 3.14: The comparison of the PSD power between previous used detector (the dashed line) and new manufactured detector (the thick solid line) . The left peaks are induced by neutrons. Because of the small amount of gamma induced events, the peaks from the gamma calibration data (the thin solid line) is also drawn which is obtained from the new manufactured one used for this comparison.

Stand type construction

We establish the stand type neutron detectors of 8 having narrow solid angles for the neutron-nucleus scattering, which cover the recoil energy deviations of 2.86 keV at FWHM. The pillar which supports the detector is composed of a camera mount which is available to modulate the angle and stands 50 kg at maximum, an aluminum profile for the frame and auxiliary part to assemble all of the components. And for combining of the detector and the pillar, we make a polyethylene box which can be joined with the camera mount. For the alignment of the scattering angle and the direction at which detectors look, we use a laser and a digital protractor. Figure 3.15 depicts an imaginary setup of a neutron detector and the needed equations for the distance and angle for the alignment. We try for the laser, which passes through the origin of

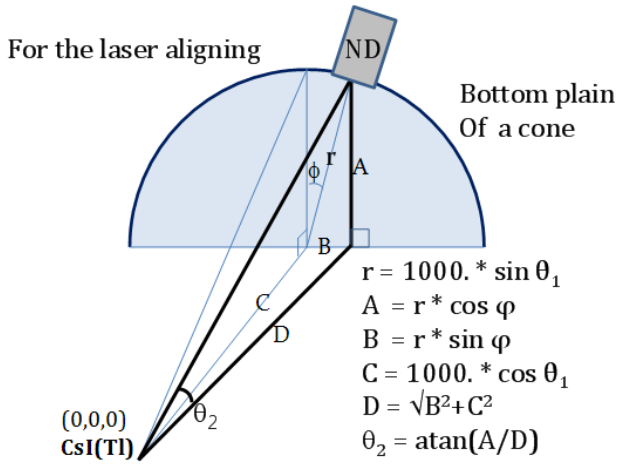

Figure 3.15: An imaginary setup of a neutron detector and the equations needed for the alignment. We obtain θ_2 and measure $A, BandC$ and set the laser on the black triangle. And we try for the laser to pass through the polyethylene box in parallel with its z axis.

our setup, to arrive at the center of each neutron detectors, however there are discrepancies under 1 cm on their faces, which mean that the recoil energies related to the detectors are deviated by 400 eV at maximum. The established detectors are seen in Fig. 3.16.

3.2.3 Neutron generator

In order to determine the nuclear recoil energy for the selected events, the mono energetic neutrons are also needed with neutron detectors at the same scattering angles. We use a neutron generator manufactured by Thermo Fisher Scientific, which emits 2.4 MeV mono energy neutrons by deuterium-deuterium collisions. This is compact, portable and easy to operate. The shape is shown in Fig. 3.17. The accelerator tube is connected to the electronics part with BNC cables. The electronics part plays a role to supply low voltages for the ionization and high voltages, 90 kV at maximum, for the ac-

Figure 3.16: The neutron detectors of the stand type. Upper figure is the front view, and bottom figure is the side view. The detectors look at the origin of this experimental setup, where CsI(Tl) crystal will be located. They are in a base side of a cone, of which angle is 60°, with making an arc.

celeration of deuteriums. When they collide at the target plane, the neutrons come out almost isotropically. The flux is around 10^6 per a second. For the control of the incident neutron direction, we need a collimator. For the safe environment, there should be the shielding stuff around it, and there also must be an emergency cut off function. We will explain the performance principle of this neutron generator and how are the safety prepared in the following sections.

Performance principle

Figure 3.18 depicts the process of the neutron generation. In the acceleration tube, there are mostly sulfur hexafluoride gases with over 8 atmospheric pressure and electronically dry, and two deuterium reservoirs at both sides, which play roles as an ionized deuterium supplier and a deuterium target plane respectively. The reservoirs are made of the zirconium material and the amount of deuteriums there depend on the temperature. The deuteriums collide and breed neutrons almost isotropically as the following process:

$$ {}^2_1H + {}^2_1H \longrightarrow {}^1_0n + {}^3_2He + 3.27MeV, 50\% \tag{3.2} $$

$$ \longrightarrow {}^1_1p + {}^3_1H + 4.03MeV, 50\% \tag{3.3} $$

Figure 3.17: The neutron generator which is composed of an accelerating tube and an electronics part.

Protons and tritiums which are generated by the same amount as neutrons are detained in the target plane due to the high negative voltage. However, high energy gammas from the fusion and x-rays from the structure material induced by the radiation come out, the shielding structures for neutrons and gammas are needed.

The shielding structure and the interlock system

Polyethylene is very effective to stop neutrons due to their hydrogen components, since neutrons deposit their energies to the same mass target at maximum in the collisions. Polyethylene of a 10 cm of thickness can reduce the neutron flux by 1/10 times, and 5 mm lead plane can reduce x-rays of tens of keV by 1/3 times. With the shielding box made of these structures, the total radiation dose rate become 26.7 $\mu Sv/h$ at maximum on the top surface of the box, 2.73 $\mu Sv/h$ at the operation place with a desktop computer, and 0.15 $\sim$ 0.73 $\mu Sv/h$ outside of the operation room. Figure 3.19 shows the neutron generator inside the shielding box. Those are appropriate level comparing to the regulation of 20 mSv/yr, when we use the generator about 2000 hours in a year. However, since there is no shielding for gammas coming from the deuterium fusion inside the tube and also from the neutron capture process in the polyethylene, we should add shielding with lead more, so we set 10 cm of shielding structure in three sides of the box, which is a part of top surface

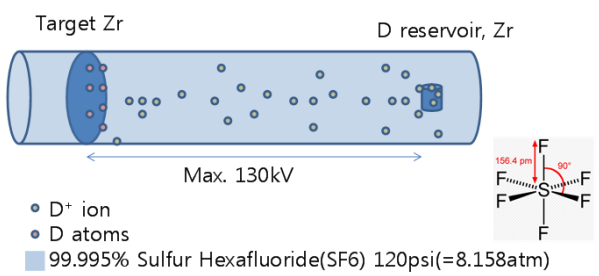

Figure 3.18: The performance scheme of the neutron generator.

and a rear surface for decreasing gamma detections in the neutron detectors and a side surface for other laboratory in the next room.

The operation for the neutron generator is done by a distant computer from the shielding box for the safety, which is connected to the generator by a serial port ,and controls the generator by a Graphic User Interface(GUI) program shown in Fig. 3.20. We modulate five parameters on the menu, the beam current, the high voltage, pulse frequency and its duty time, and the total run time. The maximum neutron flux comes out at the combination of 60 μA and 90 kV for the beam current and the high voltage respectively. However, since the gamma flux also increase, we measured the flux ratio between neutrons and gammas, $\frac{f_{Neutron}}{f_{Gamma}}$, with changing the combination. The larger the beam current, the higher the neutron flux. So we fix the beam current to 60 μA, and with changing the high voltage, we get the highest flux ratio at 50 kV, which is about 2, however, after that we add a lead shield of 25 mm thickness at the exit hole and a lead neutron guide of 75 mm thickness in the shielding box, the ratio was extremely increased as shown in Fig. 3.14. Although the added gamma shield at the exit hole can pass neutrons mostly , since gamma with over 100 keV energy can pass the shield and the isotropically radiating gammas from the shielding box can increase the trigger rate by arriving at the neutron detectors in the channeling experiment, we can not increase the beam current and high voltage further. These measurements are usually done in the pulse setup with 2000 Hz and 10 % duty time, because our DAQ time window is 30 μs and a dead time is needed for the scintillation pulses from two different events not to overlap. And the flux ratio measurement are not changed significantly with several different setup, the 200 Hz and 250 μs or the 1000 Hz and 50μs. Therefore the pulse structure has 50 μs width and 500μs interval.

Above the shielding, there should be another safety, the interlock, which can be used to shut down the high voltage in the accelerator when there is an emergency. In this generator, the interlock system is well established because neutron flux is very fatal when we are exposed to them. Figure 3.21 shows

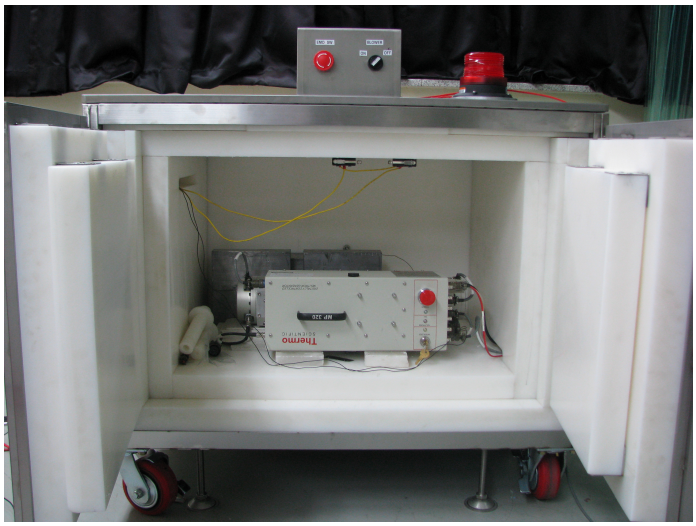

Figure 3.19: Neutron generator inside the shielding box

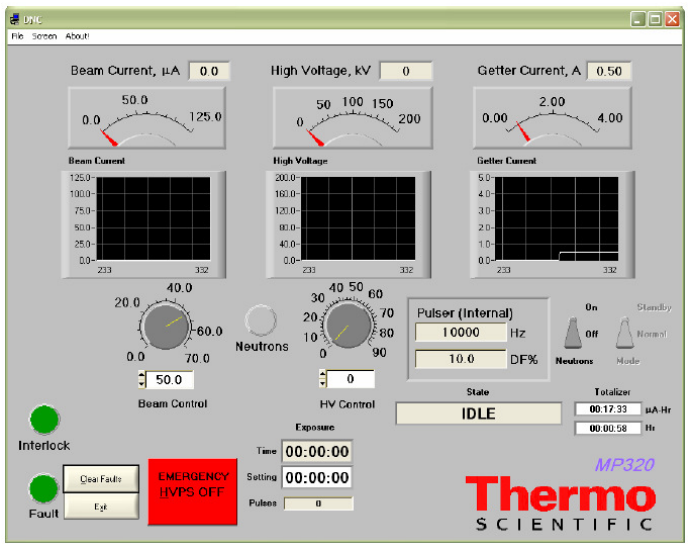

Figure 3.20: Graphic User Interface for the neutron generator

several interlocks in the circuit. Some of them are monitoring the pressure of the sulfur hexafluoride gas, the high voltage in the tube, the current through

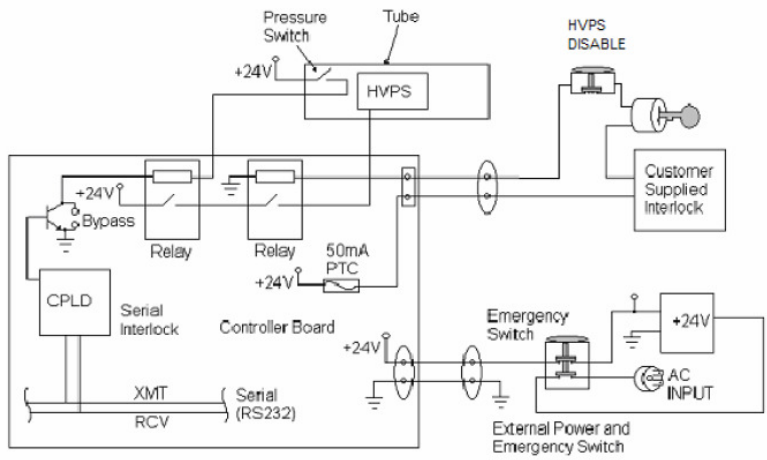

Figure 3.21: The interlock system circuit for

the warning lamp and the communication with computer through the serial port. Some of them are the active shut down for user to press the emergency button on the electronics part, the HV disable box or an emergency menu on GUI. And the auxiliary interlock can be widely applied to make an interlock. The two terminals on the aux part should be always connected, and when we construct a closed circuit with them, for example, for making a door interlock on the shielding box, if the connection is broken due to opening the door, the high voltage will be shut down.

3.2.4 Trigger logic and Data AcQuisition(DAQ)

We use VME and NIM modules to obtain data as shown in Fig. 3.23. The electronic signals and their time informations of CsI(Tl) and neutron detectors go to Flash Analog to Digital Converter (FADC) in a VME crate. FADC do the sampling for the electronic and time informations at every 2.5 ns. When there are more than two pulses in each PMT or a large peak of over 300 ns width in a PMT for CsI(Tl) detector, the combined channels in FADC generate a trigger signal(The CsI(Tl) trigger). For neutron detectors, whenever there

is single pulse larger than 40 mV and over 10 ns of the pulse width, of which equivalent ADC sum is much lower than 0.15 that is our event cut value, the trigger comes out(The neutron detector trigger). One of the triggers from two FADCs used for 5 or 8 neutron detectors, in which there are 4 channels respectively, goes to the FAN IN/OUT module to convert a TTL signal to an analog signal in the inverse mode. The trigger signal from the neutron generator is also converted to an analog signal in the module. And then those analog signals make a coincident signal while passing through the discriminator

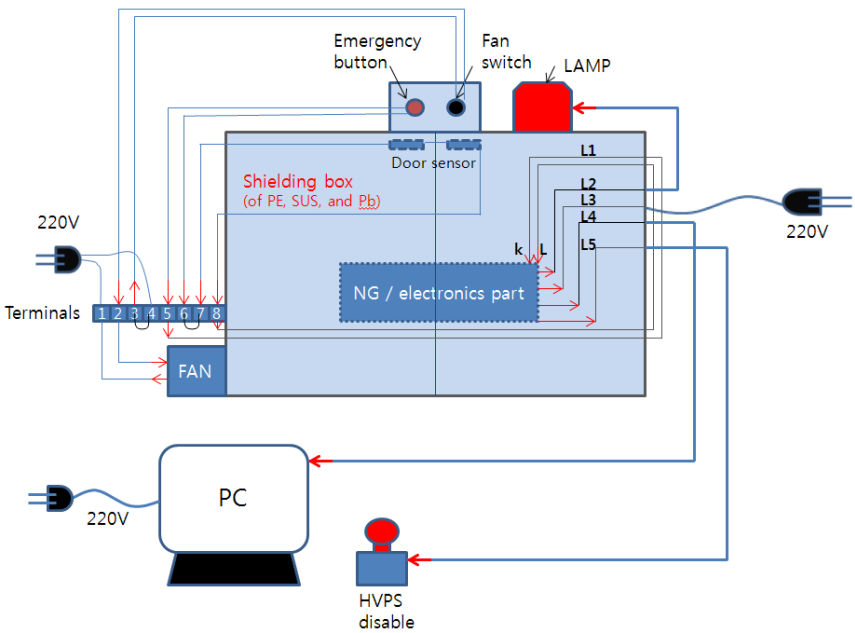

Figure 3.22: The scheme of the line connection for using the neutron generator. L1 is for the auxiliary interlock circuit connection, and the door lock on the shielding box is connected in the circuit. L2 is for the warning lamp to transform the electric power and monitor its operation. L3 is a line for the main power and L4 is for the connection to an operating computer by a serial port. L5 is for the high voltage disable box which is needed on an emergency state.

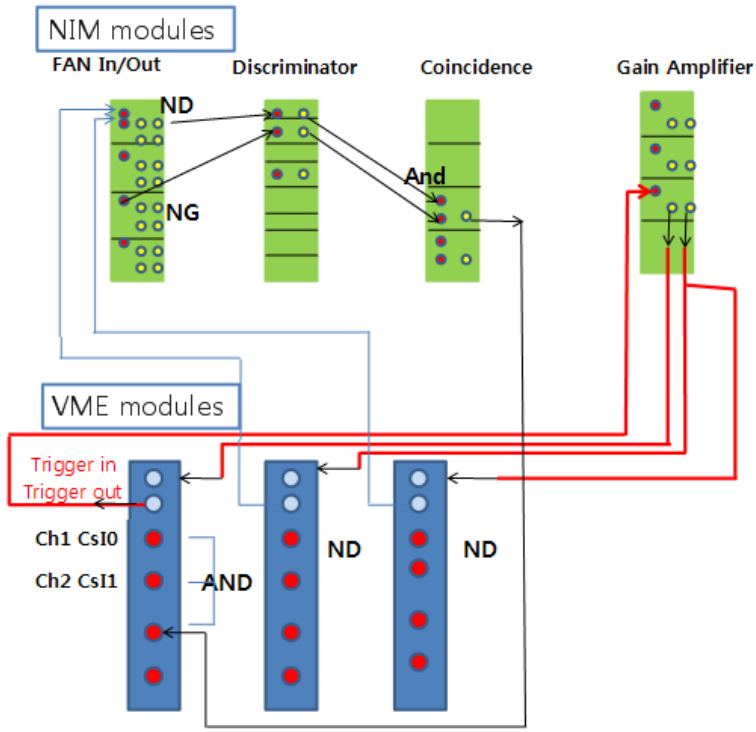

Figure 3.23: The trigger system for DAQ. The input trigger is composed of CsI(Tl) trigger output, one of the neutron detector trigger out, and the neutron generator trigger out, which are all TTL signals.

module and a coincidence module. These are all in the NIM crate. The coincident signal has usually the same width and the height as FADC trigger out of neutron detectors except the polarity, because the neutron generator trigger pulse width is 50 μs as explained in section 3.2.3 and the trigger out in FADC is 1.3 μs of width, but the polarity is inverted in FAN IN/OUT. It goes to the next channel of CsI(Tl) in FADC module, and when these are gathering in a 2μs window, there is the final trigger out. It is distributed with a help of a gain module in NIM crate. Figure 3.24 shows a three coincident event displayed on GUI made by KIMS collaboration.

3.3 Event rate

3.3.1 Analysis method for obtaining the coincident events

For the neutron scattering event selection, we use two of the same cut used in KIMS analysis for WIMP search, (5) Fit Quality cut and (8) Second time cut in table 1.2. Other cuts in the table are used to reduce asymmetry events in both sides of PMTs and PMT induced backgrounds. But in the neutron scattering events those are not necessary due to higher event rate than the backgrounds in the coincident events. Fit quality cut is for the high energy tail events, of which pulse shape looks like the randomly dispersed pulses in a DAQ time window. These events are one of the dominant background in

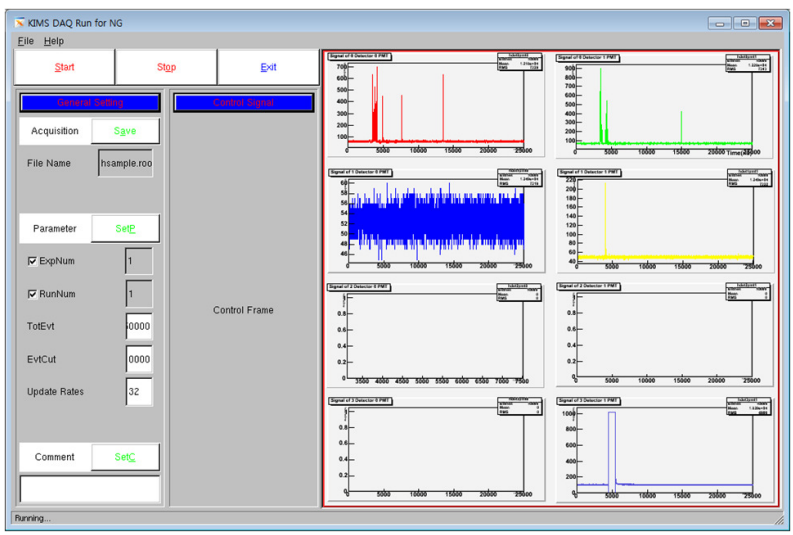

Figure 3.24: The coincident event display. Upper two plot show the signals from CsI(Tl) detector and the next 5 plots show neutron detector signals when they are coincident with CsI(Tl) detector and the neutron generator. And the last plot shows a coincident signal between a neutron detector and the neutron generator, which is inserted to the third channel in the FADC for CsI(Tl) detector to make a final coincident trigger out.

this experiment due to the high energy gammas from inelastic scatterings or neutron captures by ions in CsI(Tl) . When we fit pulses in an event with an exponential decay function, we can remove most of them by the fit quality cut. After applying the cut, the still remained elastic scattering events contaminated with this tail event can be removed by the second pulse time cut. When an event is triggered, the module places the trigger position of the pulses on the predetermined time, and save the time information. So when an event is contaminated by several random pulses, although the fit quality is good, but the start time of the pulses is in front of the predetermined time.
One of other cuts used for the neutron scattering experiment is the time coincident cut, which selects events of which start time difference between CsI(Tl) and one of the neutron detectors are within 100 ns. But for the events of lower than 5 keV energy, the cut is not applied because the start time of CsI(Tl) pulses have larger deviations in the low energy region. And the last cut is the pulse shape discrimination cut for the neutron selection in the data from neutron detectors. Due to the stand type of the detector, there is few shielding for the neutron detector. So gamma backgrounds from the environment and cosmic rays make significant coincident triggers by chance. Figure 3.25 depicts a two dimensional plot for a variable which are used for PSD and E_{meas} for total events from neutron detectors. A function on the plot divides the events into two categories of neutrons and gammas. The variable is defined as the ratio between the tail ADC sum and the total ADC sum, where the tail part is defined as "the total ADC sum – the ADC sum for the biggest pulse".

3.3.2 The coincident event rate and the Geant4 simulation

We measured neutron scattering events for four different conditions, which are for different scattering angles of 45°, 60° and 90°, and a different tilt angle of CsI(Tl) for the same scattering angle of 60°. Except 60° setup, all are not concerned with the channeling effect because we do not know the axes of three planes of the used crystal, 0610B shown in Fig. 3.1. In order to measure

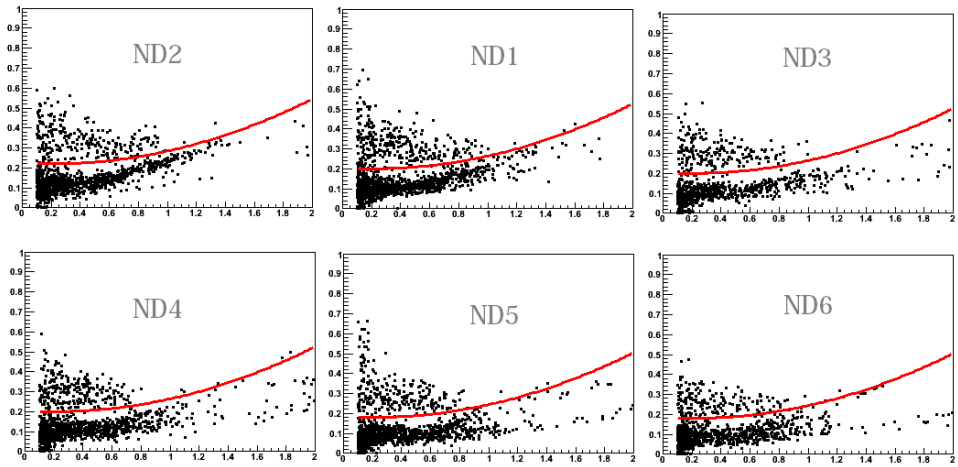

Figure 3.25: The pulse shape discrimination plot for 6 neutron detectors. The vertical axis represents the PSD value, and the horizontal axis represents the total ADC sum. The pulse height of gamma increase faster than neutrons according to the same energies. So they are saturated in FADC in the lower energy. Gamma events of the inclined shapes in the high energy mimic the neutron PSD values.

the channeling effect and the blocking effect, we used the crystal, 0609B with aligning its [110] axis to one of the recoil directions, in 60° setup after the stabilization of DAQ with 45° and 90° setups. They show much higher event rate due to the larger differential cross-section of the neutron-nucleus elastic scattering for 45° setup and the larger solid angle to detect neutrons for 90° setup. Therefore, we measure the quenching factors for 3 different recoil energies in CsI(Tl) and the channeling and blocking effect for one recoil energy. After the all event selection, we get E_{meas} originated from the neutron scattering events. By applying the cuts, the event rate is reduced by about 1/10 times than the total triggered events. The most dominant cut is the PSD cut ($\sim$ 60% reduction) and the next dominant cut is the Fit Quality cut ($\sim$ 40% reduction). The event rate is 0.000145 Hz in average for the 60° setup, and

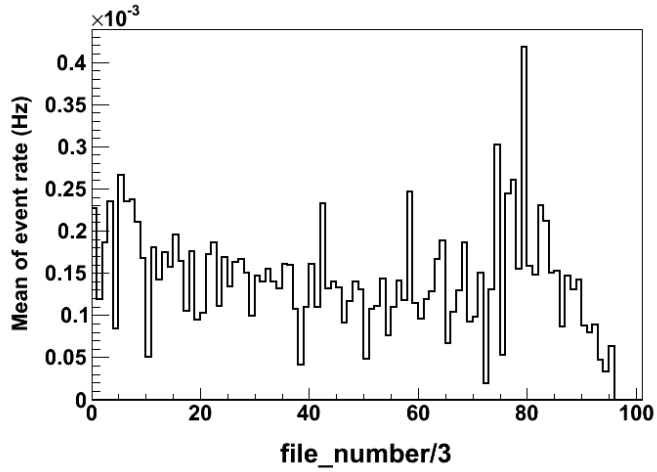

Figure 3.26: The neutron event rate distribution for the file numbers for the 60° setup. The files are combined at every three files. The event rate decreases with time passing due to the life time of the tube of neutron generator with the same setup. When we increase the beam current and high voltage to increase the neutron flux around 80 in the tied file number, actually $\sim$ 240, the flux increases temporally.

we obtain as far as possible within tube life time of the neutron generator in order to measure the tail events induced by the channeling effect with the sufficient statistics. The event rate after applying cuts are distributed for the file numbers, which represent the time passed in Fig. 3.26 and the total time to obtain the data in the 60° setup is $\sim$ 125 days.

We construct the experimental setup in GEANT4 simulation to compare the event rate of measured and estimated for the verification of DAQ system and the setup and to know the CsI(Tl) detector performance by the neutrons injections. To reproduce E_{meas} in the setup, we insert the Landau-Gaussian fitting function of E_{meas} of Fig. 2.11 for each recoil energy in the code. Figure 3.27 shows the constructed setup in GEANT4. The estimation of the event rate is based on the information of the neutron flux and the

decreasing ratio for different conditions of beam currents and high voltages given by company, the geometry of the experimental setup, and the differential cross-section obtained from the simulation in GEANT4 with a neutron high precision model(NeutronHP modle). The estimated rate is 0.00152 Hz, which is about 10 times higher than that of the measured. The reason that the accidental coincident trigger induced by background gammas reduce the probability to detect neutrons. For the experiment for 90°, we just use the previous constructed setup with larger solid angle in data taking. Since it is possible to do enough lead and polyethylene shieldings around CsI(Tl) and also neutrons detectors due to the simple structure, the measured event rate is higher by six times than that of other setup. The neutron scattering events are selected in the simulation when events satisfy the following criteria simultaneously:

- Deposit energy in CsI(Tl) > 0
- Gamma energy from the inelastic scattering in CsI(Tl) > 50 keV[a]
- X keV < $E_{meas,neutron}$ in the neutron detector[b] < Y keV
- No contribution in E_{meas} by gamma in the neutron detector
- Only one of the neutron detectors has E_{meas} , larger than 0.

[a] When there is a transition from L shell to K shell in a nucleus, the gamma energy from Cs is 79.6 or 80.9 keV and from I is 57.6 keV. But in GEANT4 emits lower energy gammas for the energy conservation in the G4NeutronHPFinalState. We do not include those events.

[b] E_{meas} is calculated by the sum of Eq. 3.4 [84]. Since we use the ADC sum cut from 0.2 to 0.8 for the pulses detected bv neutron detectors in the experiment, by comparing the ADC sum at 477.3 keV in the measurement, we determine X and Y. The energy calibration of neutron detectors was in section 3.2.2.

$$E_{meas,neutron} = 0.83P - 2.82[1 - exp(-0.25P^{0.93})], \tag{3.4}$$

where P is the proton energy obtained by an elastic scattering with a neutron.

The reproduced E_{meas} are presented in the next section.

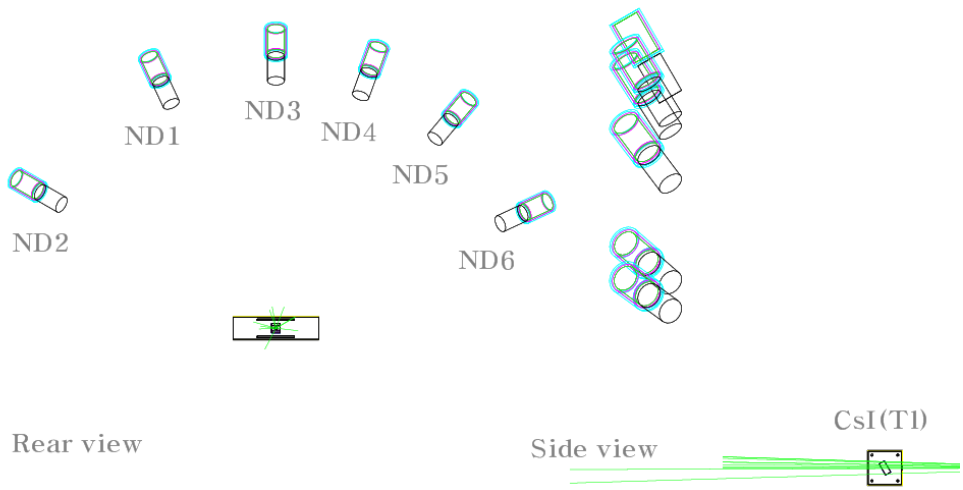

Figure 3.27: The constructed setup in GEANT4 with considering the scattering angle of 60 ° about the central axis of the incident neutron directions. Although not seen in this figure, there are polyethylene boxes around neutron detectors. The empty cylinders represent holes in the boxes and the filled cylinders represent neutron detectors. And a box in the central position is the CsI(Tl) detector setup.

4 Results

For the channeling and blocking measurement, we measure E_{meas} in the case that directions of recoil ions are aligned at a symmetry axis, [110], and other cases that directions are on random axes. The difference between them can be explained one of those effects. For total events including all of the recoil directions, a comparison of E_{meas} between the measured and those modeled by GEANT4 and MARLOWE, enables us to prove the existence of those effects.

4.1 E_{meas} distributions

4.1.1 Comparing with the reproduced E_{meas}

We obtain E_{meas} for three different recoil energies in the experiment and the simulation as shown in Fig. 4.1. The recoil energy is determined for each setup of a different scattering angle by

$$E_{recoil} = \frac{2E_n}{(1+\mu)^2}(\mu + sin^2\theta - cos\theta\sqrt{\mu^2 - sin^2\theta}), \tag{4.1}$$

where μ is M_r/m_n, M_r is the recoil ion mass, m_n is the neutron mass, and E_n is the injected neutron energy. The recoil energies for various neutron scattering angles are given in Table 4.1. In Fig. 4.1, the thick lines are data and the dashed and the filled lines are reproduced ones by GEANT4 and MARLOWE. We normalize them by the number of events from 1 keV to 10 keV, because it is the expected range for most of nuclear recoil scatterings to be observed. The ratio between the peak heights of nuclear recoil events(peak under 10 keV) and that of inelastic events(peaks at 60 and 80 keV) are different for the data and the simulation due to the coincident trigger efficiency in data. The higher the energy deposition, the lower the fluctuation of the start time of the scintillation in CsI(Tl) crystals, so that the time difference would be smaller

between the initial pulses from CsI(Tl) and the neutron detector and thereby, lower probability to be intercepted by other random coincident events. For the simulation spectra, the left peaks represent pure nuclear recoil events without gamma energy depositions and the right two peaks represent the events with gamma energy deposition, induced by the neutron-nucleus inelastic scattering. The energy of the right peaks are divided into the nuclear recoil energy and the gamma energy. These gammas, which are 57.6 keV for I and 79.6 or 80.9 keV for Cs in the spectra, emit when the excited iodines and cesiums at the L shell go to the ground state of K shell, respectively. The event ratio of the right two peaks for the total events increases with the scattering angle. This is because of the differential cross-sections of the elastic scattering and inelastic scattering. The reason that the peaks of ∼80 keV in data are shifted to lower energy is the saturation in FADC module and the nonproportionality for the gamma response of CsI(Tl) .

4.1.2 Channeling fraction

In the reproduced E_{meas} distribution for a recoil energy with MARLOWE, which is discussed in section 2.4.2, less than 3 % of the nuclear recoil events in the monocrystalline CsI(Tl) show larger E_{meas} than the maximum in the amorphous target, which we are attribute to the channeling events. The peaks in the E_{meas} distribution are also different for the two targets. The peak of the monocrystalline target is shifted to lower energy due to some fraction of blocking effect. We compare the spectra in data with those of the simulations considering the monocrystalline and the amorphous CsI(Tl) in order to know which is better fitted to the spectrum in data. Those of the monocrystalline CsI(Tl) in the simulations are fitted to the data better in the points of the position of the most probable E_{meas} , which can see more clearly in Fig. 4.3 and the amount of tail events.Though the differences are not significant, we can state that in our data, there is a shift to the low energy due to the blocking effect, since the position of the most probable peak is lower than that of amorphous and the enhanced tail events due to the channeling effect since the

simulation with the amorphous target could not reproduce tail events enough. We estimate the channeling effect in our data quantitively with an assumption for the energy region of the partial channeling and full channeling. The partial channeling means ions undergo the dechanneling and channeling alternatively in their total ranges, and the full channeling means they undergo only the channeling from start to finish. The regions for the partial and full channeling in our assumption are as follows:

- for the partial channeling : from $E^{a}_{norma} + 3\sigma_{normal}$ to E^{b}_{recoil} - $2\sigma_{recoil}$
- for the full channeling : from E_{recoil} - $2\sigma_{recoil}$ to $E_{recoil} + 2\sigma_{recoil}$.

[a] E_{normal} means E_{meas} for normal nuclear scattering events which can be fitted with Gaussian distribution. So σ_{normal} is their σ value.
[b] E_{recoil} means E_{meas} for the full channeling events which can be fitted with Gaussian distribution due to the energy resolution of CsI(Tl) and the deviation of neutron energies by the solid angle of neutron detectors. So σ_{recoil} is their σ value.

The correspondent values for the energy region and the channeling fraction for each setup is listed in Table 4.2. In this table, the partial channeling fraction is larger that 3 % due to contaminations from multiple scattering and inelastic scattering without gamma energy deposition; both are expected at the $\sim$ 1.3 % and $\sim$ 0.57 % levels, for the 60° setup. These effects for the full channeling peak is negligible. This means the events in the full channeling region are from the channeling effect or the random coincidence events. This will be confirmed with more statistics and better understanding of the systemic uncertainty. The Log(rmt10) for the selected events can be seen in Fig. 4.4, however the statistics are not enough to get their mean values to compare with others in Fig. 3.4.

Table 4.1: The recoil energy for the neutron scattering angle

neutron scattering angle (°)	recoil angle (°[a])	$E_{recoil}(keV)$	
		Cs	I
45	67.7	10.5	11.04
60	59.8	18.0	18.82
75	52.3	26.6	27.85
90	44.8	35.8	37.5
105	37.3	45.	47.1
120	29.8	53.5	56.
135	22.35	60.8	63.66

[a] All recoil angles are same for Cs and I ions except for the setup of 45° neutron scattering, the recoil angle of I ion is 67.4 ° .

Table 4.2: The assumed energy regions for the partial and full channelings and their fractions

Scattering angle(°)	partial	p-fraction[a]	full	f-fraction
45	2.5 ∼ 9 keV	5.6[b] %	9 ∼ 11 keV	0.2 %
60	4 ∼ 16 keV	4.9 %	16 ∼ 21 keV	0.06 %
90	6 ∼ 21 keV	5.2 %	21 ∼ 42 keV	1.8[c] %

[a] The total events are determined as not the entries in data, but the expected number of events from the simulation after the normalization with the events between 4 ∼ 10 keV in data, some part of the tail events, because below 3 keV, the trigger efficiency is lower than 80 % [13].
[b] This fraction includes the multiple scattering and inelastic scattering events, their contributions are 1.3 % and 0.57 % at the 60° setup.
[c] In the full channeling region in 90° setup, around 36.6 keV, there are contaminations from the x-ray escaped events for the inelastic scattering events with ∼ 60 keV of gammas.

4.1.3 Quenching factors

From the first peaks in Fig. 4.1, we can measure the quenching factors for three recoil energies. Quenching factor is important in the analysis for the determination of the WIMP-nucleon cross section, because it is a conversion factor for the recoil energy to the E_{meas} . From this conversion, we can make an expected E_{meas} for WIMPs in the CsI(Tl) crystal at a fixed cross-section, and from the comparison between this and the measured one in the WIMP search experiment, we can find the real cross section. By the way, the quenching factors are usually obtained from the Gaussian mean value in E_{meas} . But E_{meas} in our data shows an asymmetric distribution. The factors to make E_{meas} asymmetric are the multiple and inelastic scattering, the channeling effect and the low trigger efficiency below 2 keV. So, for the exact quenching factor, we should consider all, but in the current status, the trigger efficiency is not corrected for. Table 4.3 shows the estimated quenching factors from the histogram mean value or the peak value of E_{meas} of this experiment. Due to the trigger efficiency, the histogram mean values are inferred to be overestimated, especially for the 45° setup.

Table 4.3: The estimated quenching factors of CsI(Tl)

E_{recoil} (keV)	10.8	18.4	31.3
QF^{b}_{peak}	0.12	0.98	0.8
QF^{c}_{histo}	0.20 ± 0.01	0.13 ± 0.0028	0.117 ± 0.0030

[a] Due to the large solid angle of the neutron detectors in 90° setup, the events of 36.6 keV for 90° neutron scattering angle are not dominant in the detected recoil energies. [b] Quenching factors are obtained from $\frac{E_{peak}}{E_{recoil}}$.
[c] Quenching factors are obtained from $\frac{E_{histogram}}{E_{recoil}}$. Only with statistical errors.

4.2 Comparisons of E_{meas} among different recoil directions

To align recoil directions on a symmetry axis, [110], we tilt CsI(Tl) like Fig. 4.5-(a). So the central positioned neutron detector, ND3 on Fig. 3.27, would see the neutrons of which recoil ions go straight to the next target and undergo a large angle scattering, thereby the light yield may also decrease in CsI(Tl) . The solid angle is ~ 0.2 msr and the recoil angle deviation for the single elastic scattering is $\pm$ 3 $^\circ$ in the GEANT4 simulation. From the MARLOWE simulation, upto $\pm$ 5 $^\circ$ deviations the recoil directions are subject to the blocking effect [110]. For multiple scattering and inelastic scattering, the angle deviations of recoil ions are larger than that of single scattering, but since the fraction of the total events is several %, ND3 is expected to usually see neutrons related to the blocking effect. So we compare each E_{meas} distribution for the six neutron detectors in 60° setup. In Fig. 4.6, we compare the mean of E_{meas} of each neutron detector in the assumption that if a recoil ion goes through the symmetry axis, E_{meas} may be lower than other recoil ions which go to nonsymmetry axes due to the large angle scattering. Within the maximum recoil energy, 18.4 keV in the 60° setup, the mean values are 10% lower for ND3 than the neighboring NDs. The difference of E_{meas} can be found in Fig. 4.7 and Fig. 4.8. Events tagged by ND3 have lower values of the peak position and a lower number of tail events, though the difference is not well discriminated. In the MARLOWE simulation, the difference was 20%. However, when we tilt the crystal in opposite way that the neutron path which will be the road to be detected by ND3 is aligned along [110] axis as shown in Fig. 4.5 (b), still the events from ND3 shows lower E_{meas} . There may be several reasons for this. First, in both cases, neutrons to go to ND3 have the lower probability to do multiple scattering in CsI(Tl) , because of thiner thickness of CsI(Tl) along the neutron moving direction for the case in Fig. 4.5 (a) and [110] channeling of neutrons for the case in Fig. 4.5 (b). Second, the misalignment of the ND3 to detect neutrons with lower scattering angles. Third,

there are fluctuations of E_{meas} due to not enough statistics. The first one will be checked by another experiment with different tilt angle and for the second one, we should align detectors regularly. For the initial time after the setup, the alignment of neutron detectors have $\pm$ 1° uncertainties, which are correspondent to the 0.4 keV recoil energy deviation. For the third one, we checked with GEANT4 simulation where there are $\sim$ 5 % fluctuation. If the first one is the dominant factor to determine the E_{meas} distribution, we should use very thin crystal to observe the blocking effect. Fig. 4.11 and Fig. 4.12 show the reproduced E_{meas} in the monocrystalline and amorphous CsI crystal respectively which are selected by each neutron detector. The dashed line show the multiple scattering and the filled one show the gamma contaminated events. In this figure, if the crystal is monocrystalline, there are enhanced E_{meas} events in addition to multiple scattering events, but, in the amorphous crystal, the multiple scattering events dominate the tail region. Indeed due to the thiner thickness of CsI along the neutron moving direction, the E_{meas} for ND3 is inferred to haver lower multiple scattering events. We can also check the fluctuations in this figure. However, the blocking effect should be exist by the same fraction of the channeling effect of incident ions from outside according to the theoretical work. According to N. Bozorgnia *et al.* [44], I ions of 20 keV injected from outside have the channeling fraction of over 50 % without dechanneling and 5 % with dechanneling. So we will work to reduce the uncertainty in this experiment further.

4.3 Applying to WIMPs search

The uncertainty is remained for the statement that we measure the channeling and blocking effect and the pulse shape of the channeling events are discriminated from that of the Compton electron which is the one to be removed by our PSD. However, we reproduce the E_{meas} spectrum at each neutron scattering angle as Fig. 4.1 and those are fitted to the data well. In addition,

the Log(rmt10) distribution in the partial channeling region can not be said that it is similar with that of the Compton electrons. So we assume that we measure the channeling effect as the way that we expect by the simulation and the events are not removed by our pulse shape discrimination cut, and apply the reproduced E_{meas} to establish the expected E_{meas} induced by WIMP in the CsI(Tl) crystal. Figure 4.13 shows the expected E_{meas} for two different WIMP masses for WIMP–Cs scatterings with 1 pb of the cross-section. In the modified spectrum, the solid lines, there are enhanced E_{meas} events due to the channeling effect. With this modified E_{meas} spectrum induced by WIMP, we can reanalyze the KIMS data to see the channeling effect on WIMP search.

Figure 4.14 show the WIMP-nucleon SI scattering cross-section limt for the WIMP mass. The solid line is our modified limit after consideration of the channeling effect, and the dashed line is the recently published KIMS limit. In order to compare them and to measure the channeling effect on the WIMP-nucleon cross-section limit, the mean of quenching factor which we measure in this experiment was modified, because the quenching factors are different.

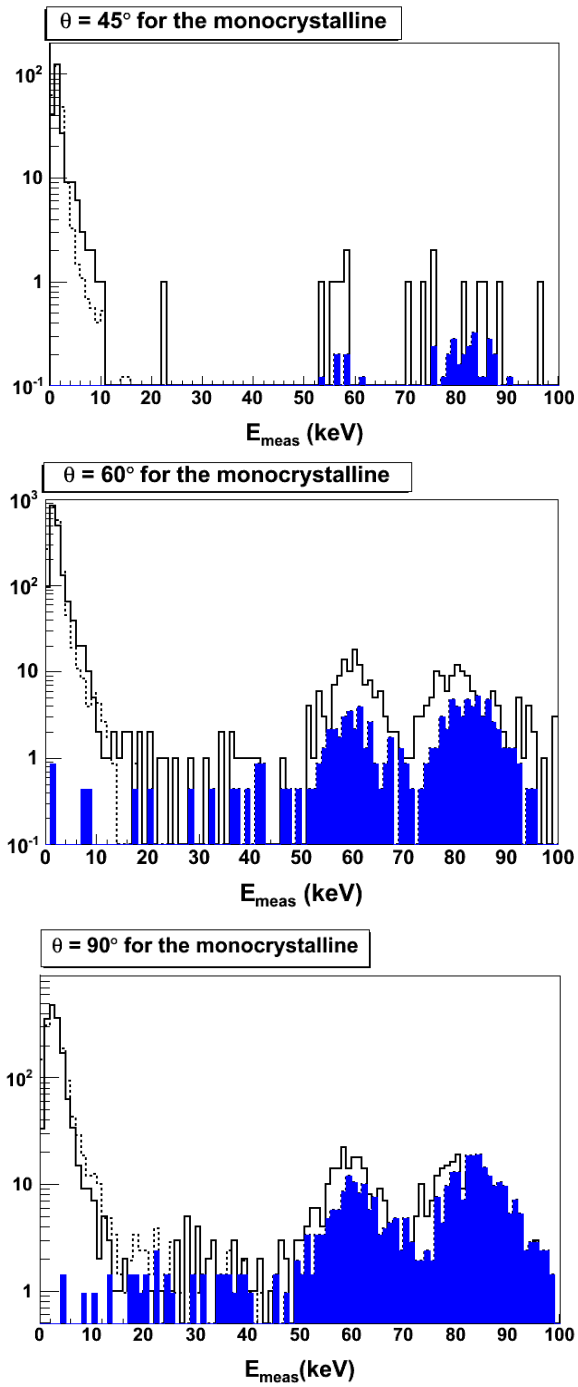

Figure 4.1: The E_{meas} in data and the simulation with the monocrystalline CsI(Tl) for the 45° (top) , 60° (middle) , and 90° (bottom) setups.

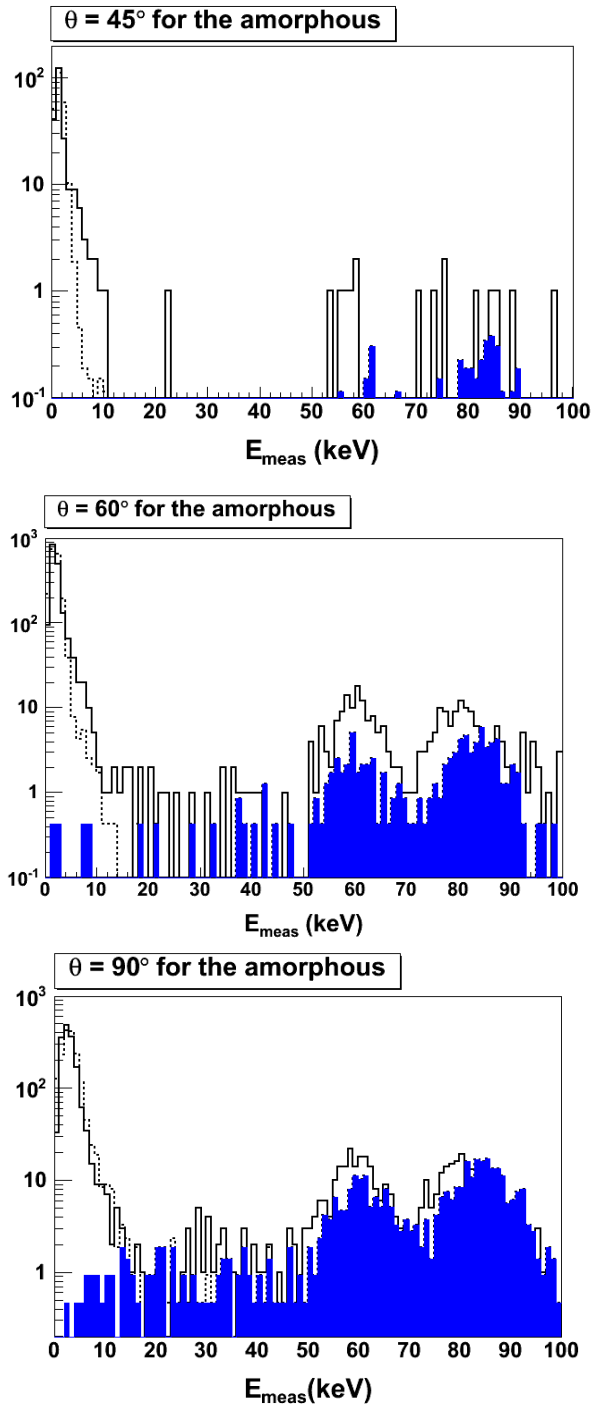

Figure 4.2: The E_{meas} in data and the simulation with the amorphous CsI(Tl) for the 45° (top) , 60° (middle) , and 90° (bottom) setups.

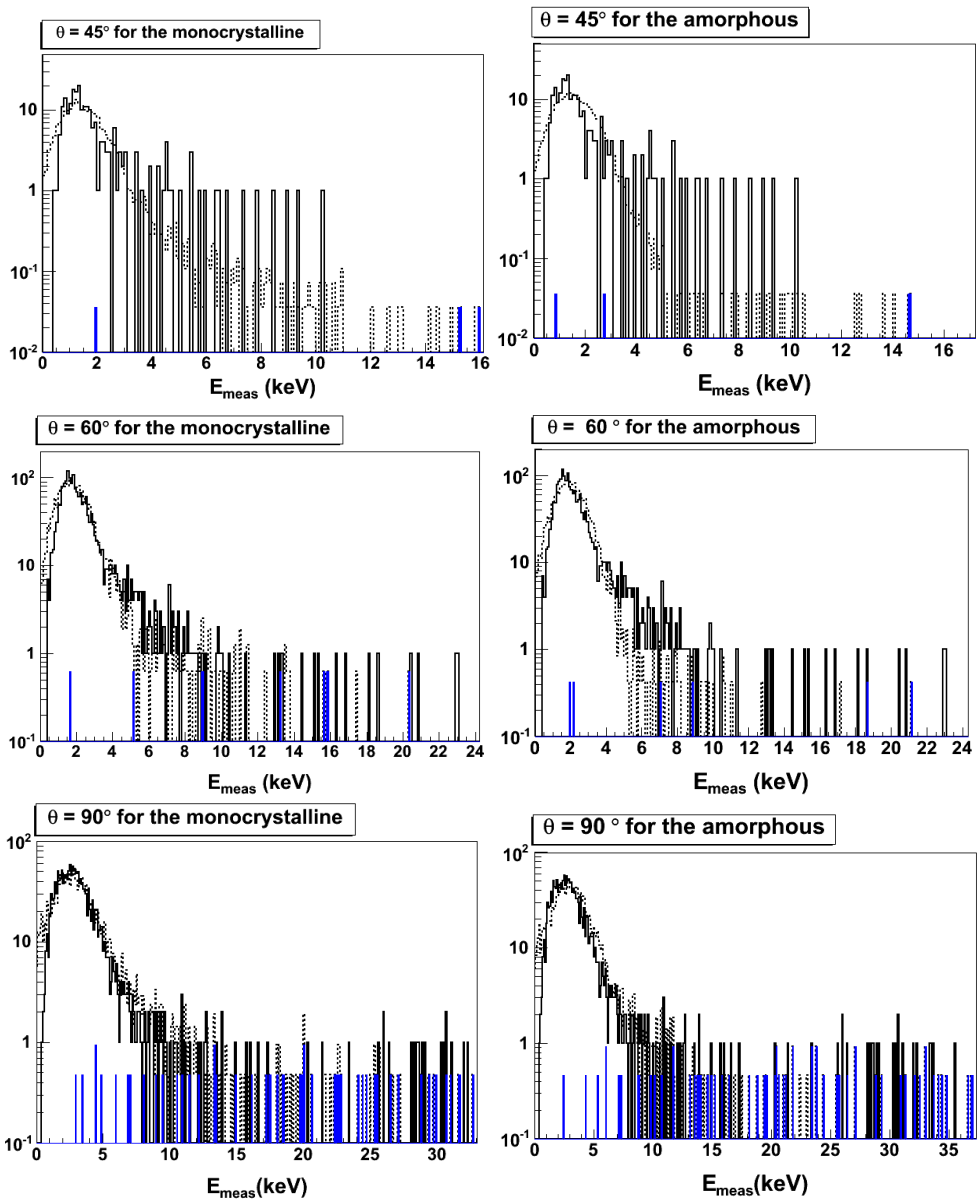

Figure 4.3: The refined E_{meas} for the front peak in data and the simulation with the monocrystalline(left) and amorphous(right) CsI(Tl) for the 45° (top) , 60° (middle) , and 90° (bottom) setups. The thick solid line is E_{meas} from data, the dashed line is that from simulation events which are selected as the pure nuclear scattering, and the filled region represents that from simulation events selected as the gamma contaminated events.

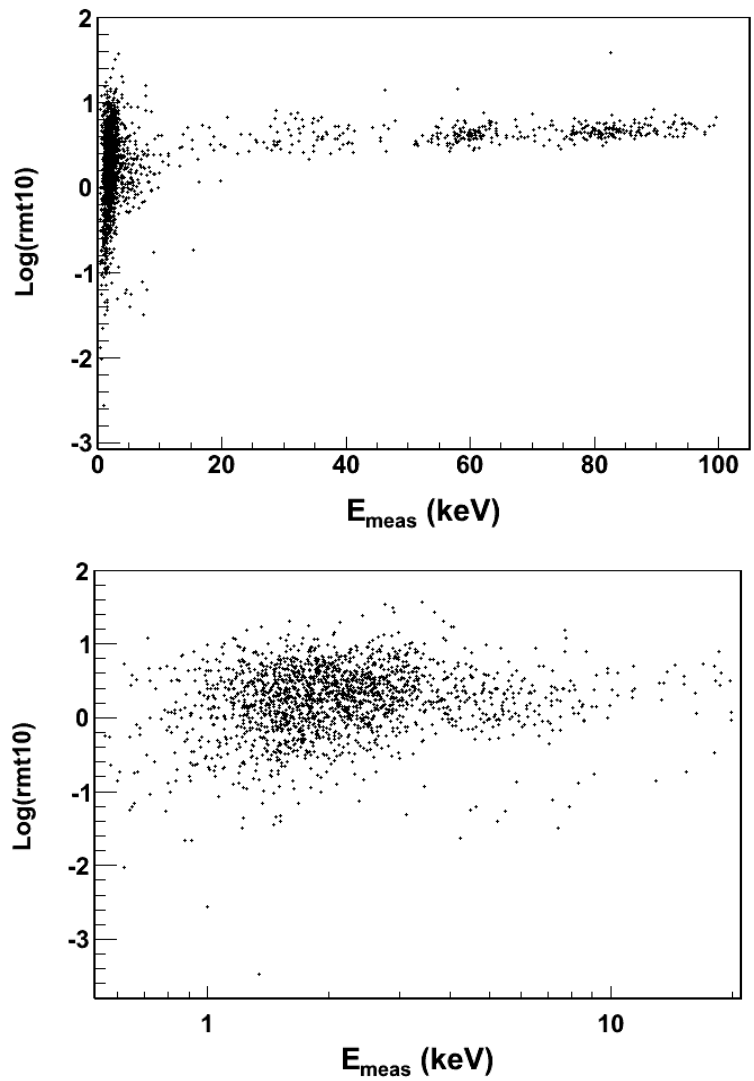

Figure 4.4: Two dimensional plot for Log(rmt10) and E_{meas} for neutron scattering events. Top plot shows events under 100 keV and bottom plot shows under 20 keV.

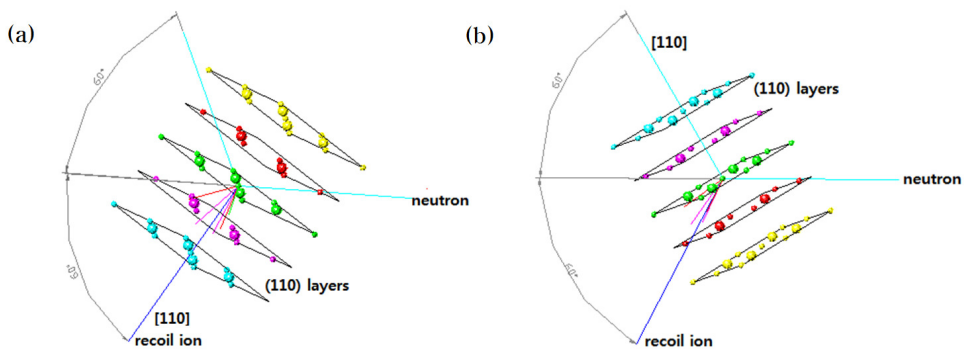

Figure 4.5: The scheme of (110) layers of CsI(Tl) and one of the trajectory of a neutron and a recoil ion in the layers tilted by 60° to the central direction of the incident neutrons for the blocking measurement(a) and tilted by - 60° for the comparison(b).

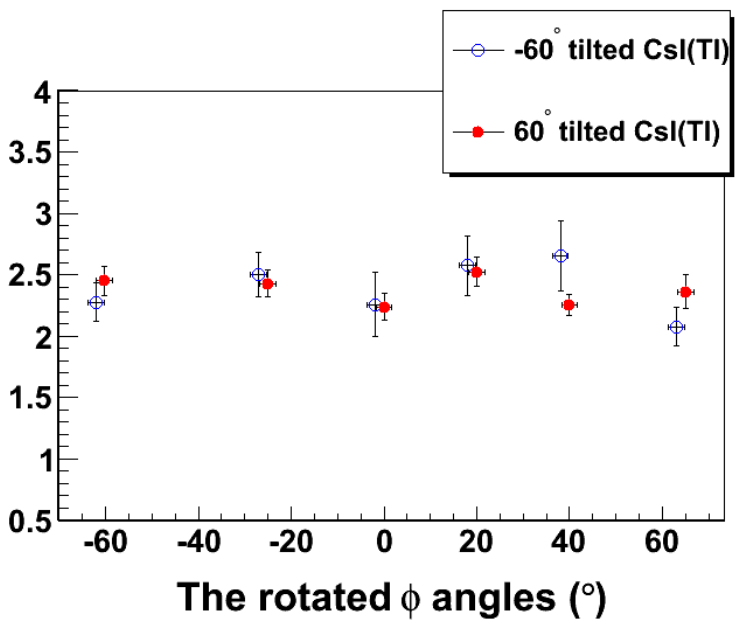

Figure 4.6: The mean of E_{meas} correlated with neutrons tagged by each neutron detector. The difference between them is about 10 % at maximum. The red points are data for 60° tilted CsI(Tl) and the blue points are data for -60° tilted CsI(Tl) .

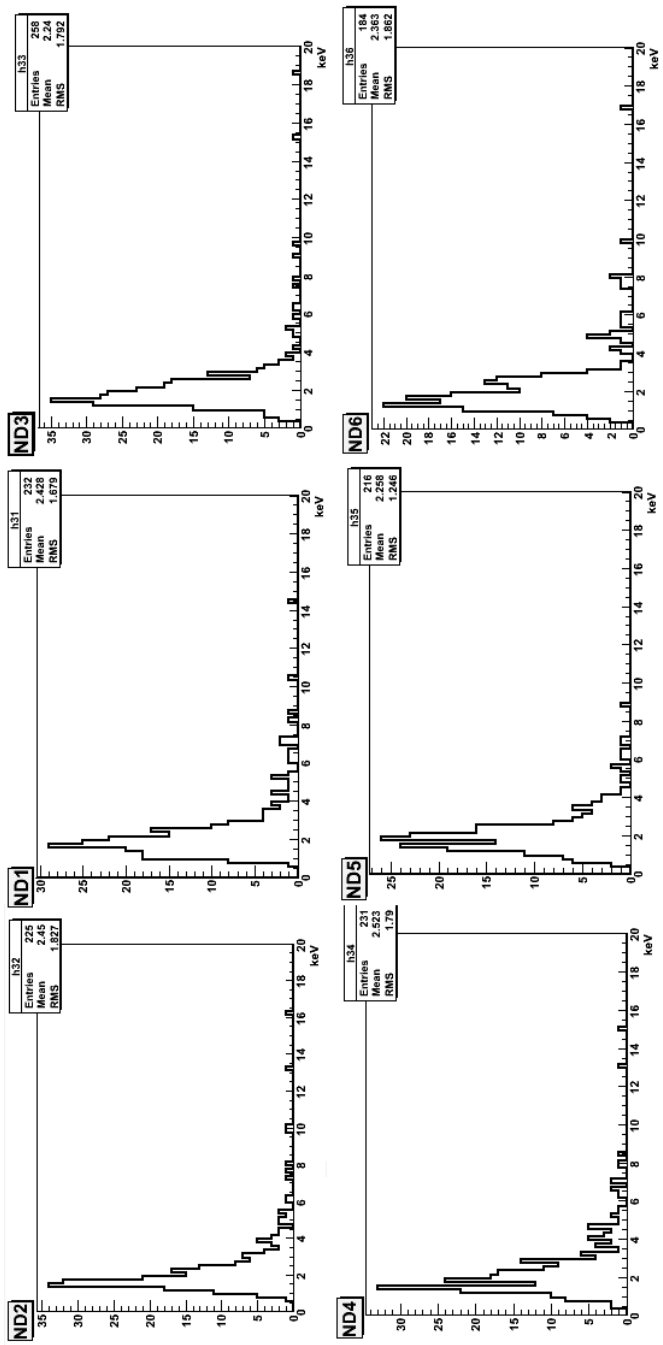

Figure 4.7: The E_{meas} spectra correlated with neutrons measured in each neutron detector in the case of Fig. 4.5(a).

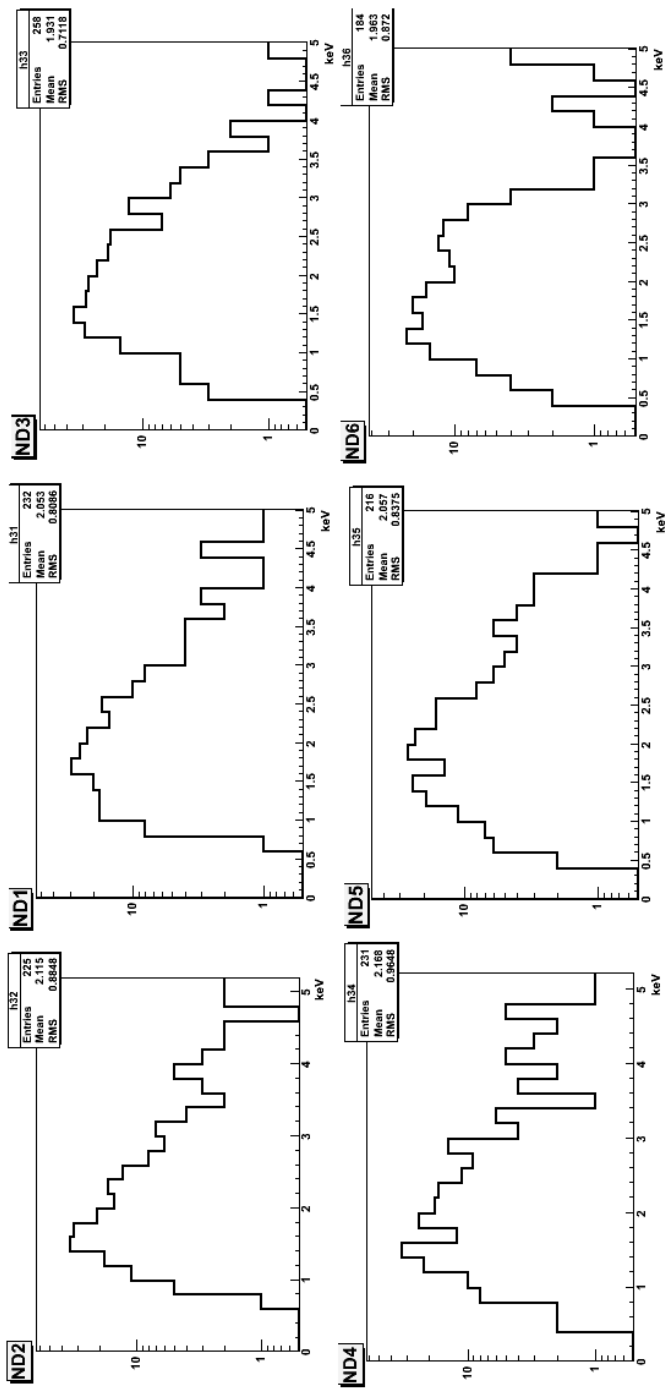

Figure 4.8: The E_{meas} spectra correlated with neutrons measured in each neutron detector in the case of Fig. 4.5(a) in the log scale.

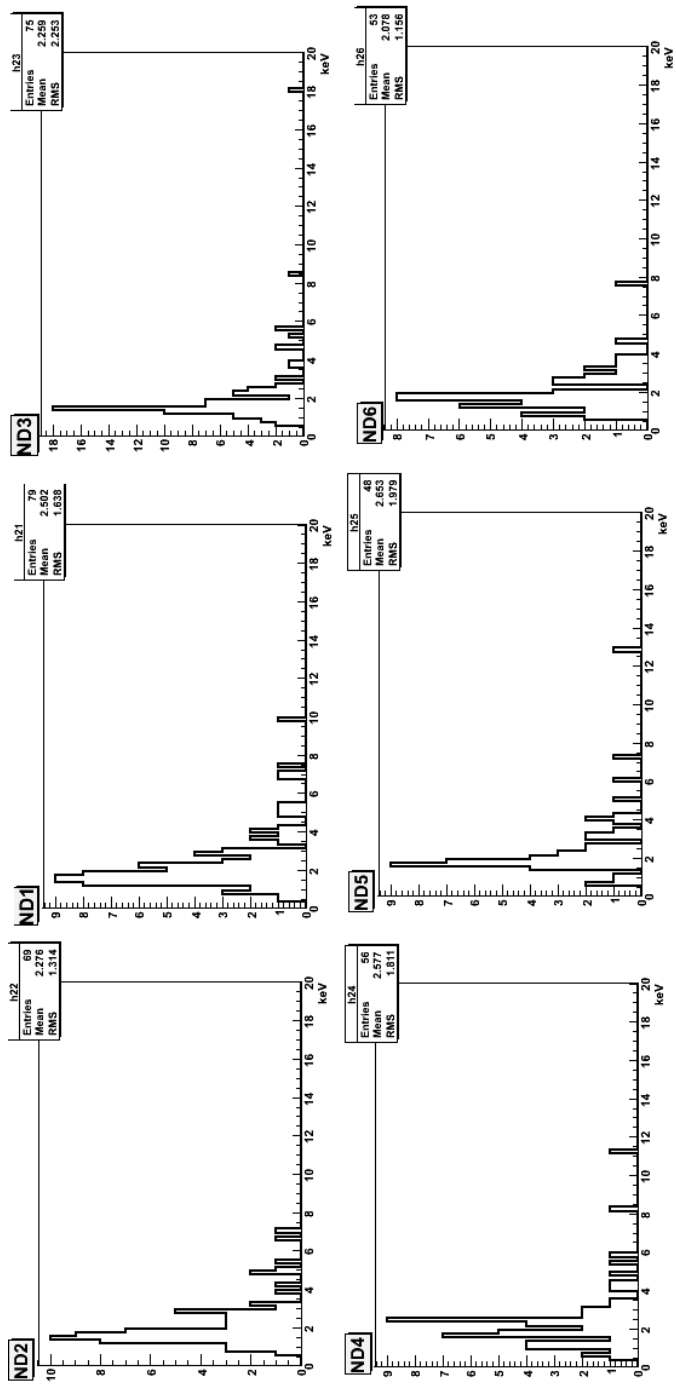

Figure 4.9: The E_{meas} spectra correlated with neutrons measured in each neutron detector in the case of Fig. 4.5(b) .

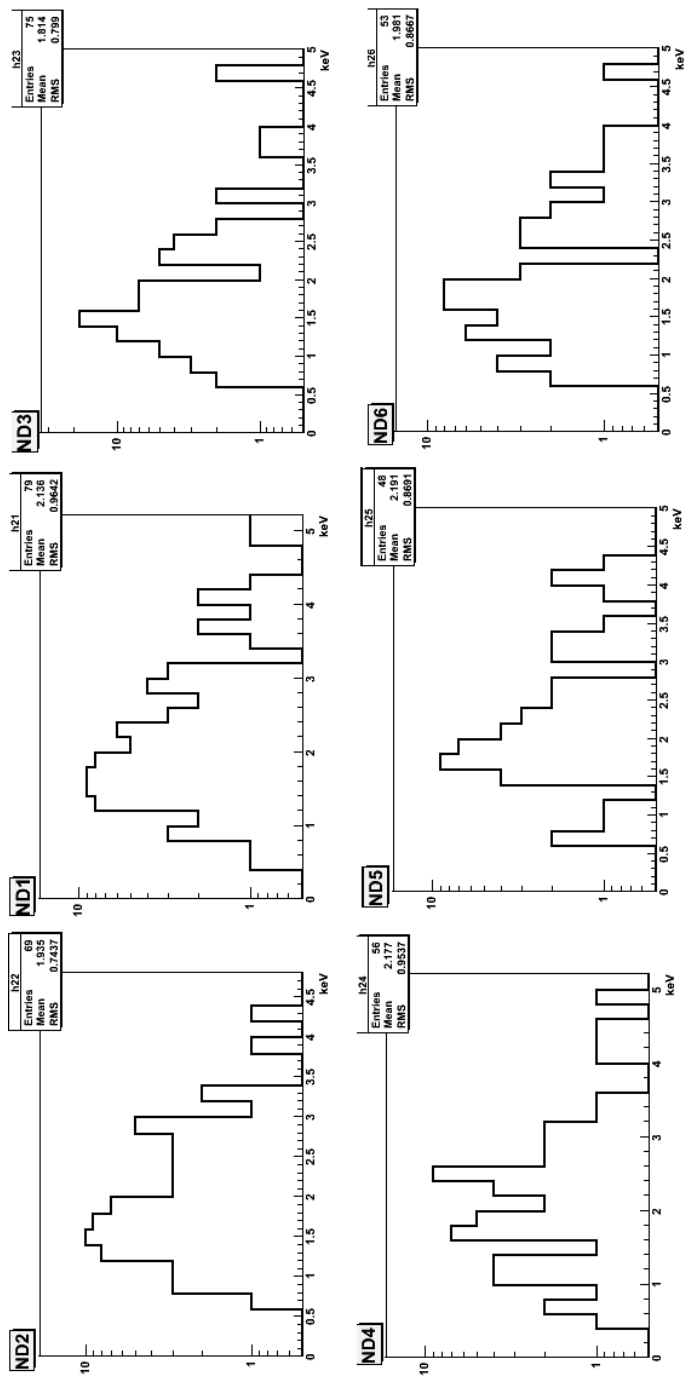

Figure 4.10: The E_{meas} spectra correlated with neutrons measured in each neutron detector in the case of Fig. 4.5(b) in the log scale.

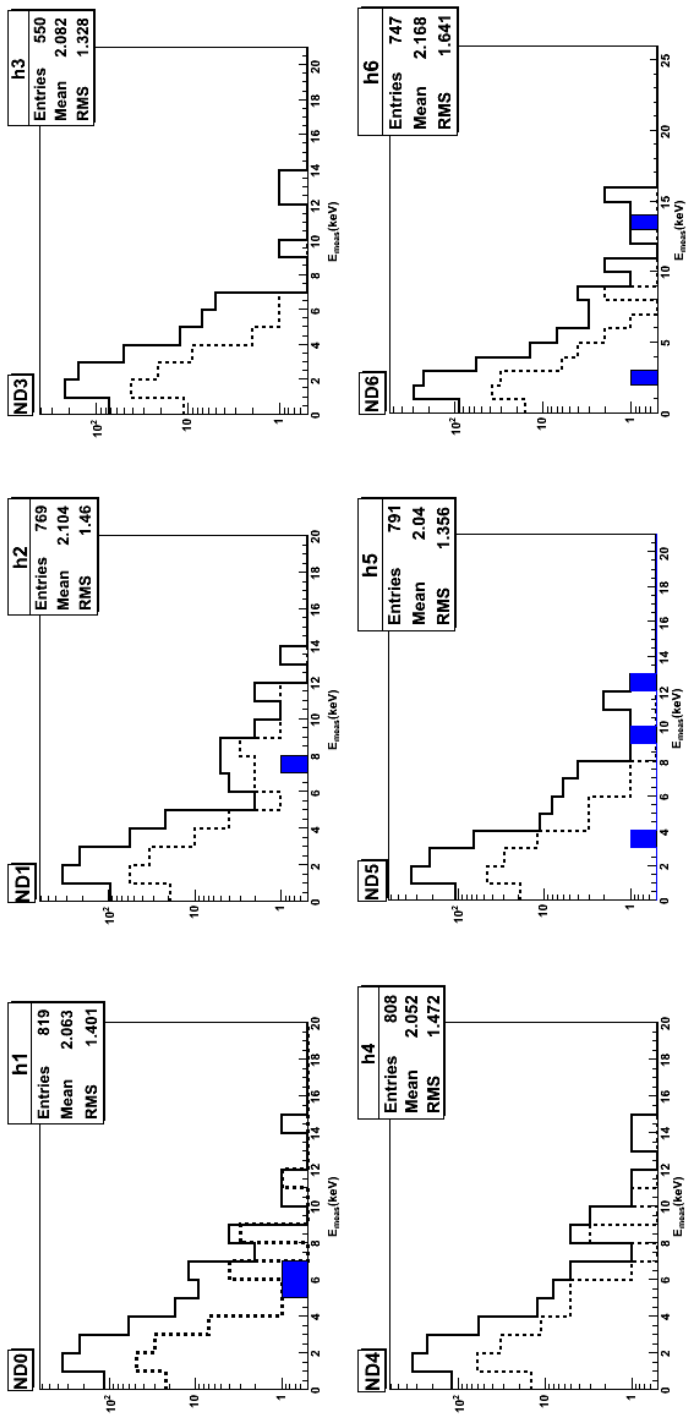

Figure 4.11: The reproduced E_{meas} spectra in the case of Fig. 4.5(a), the monocrystalline CsI and 60° setup.

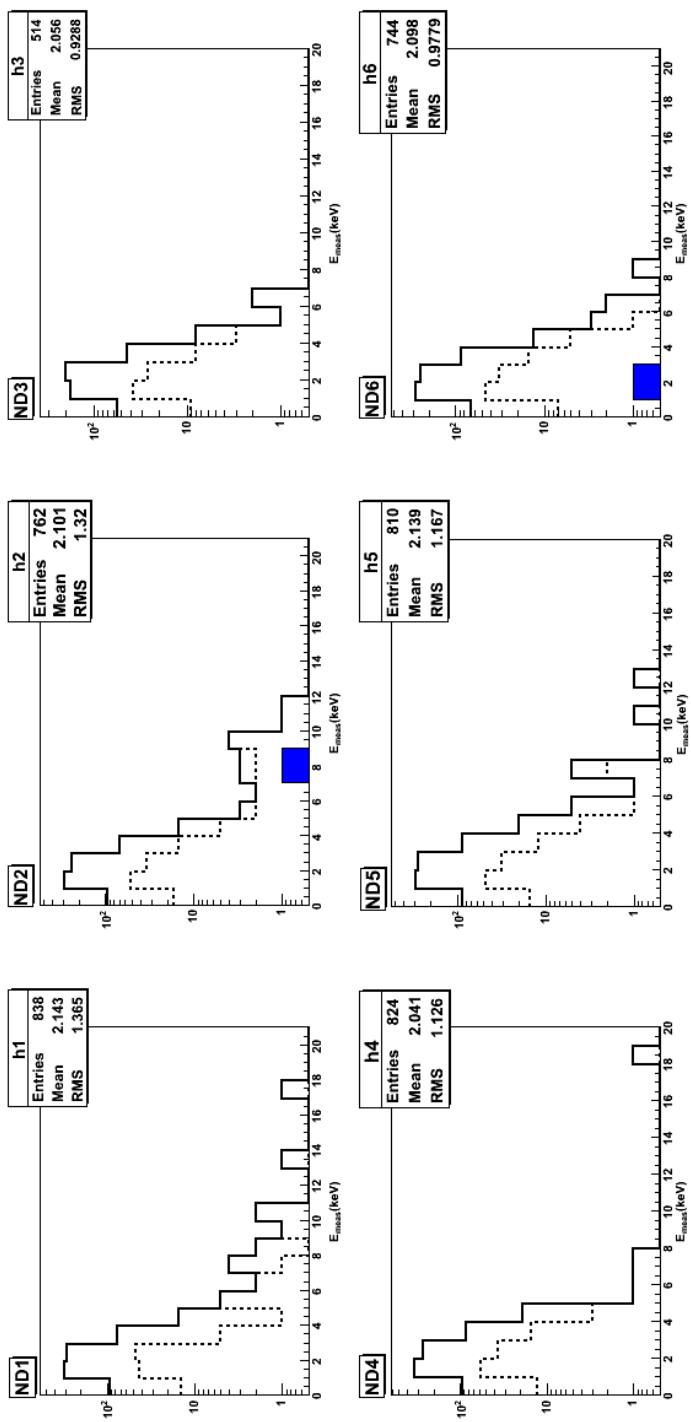

Figure 4.12: The reproduced E_{meas} spectra in the case of Fig. 4.5(a), the amorphous CsI and 60° setup.

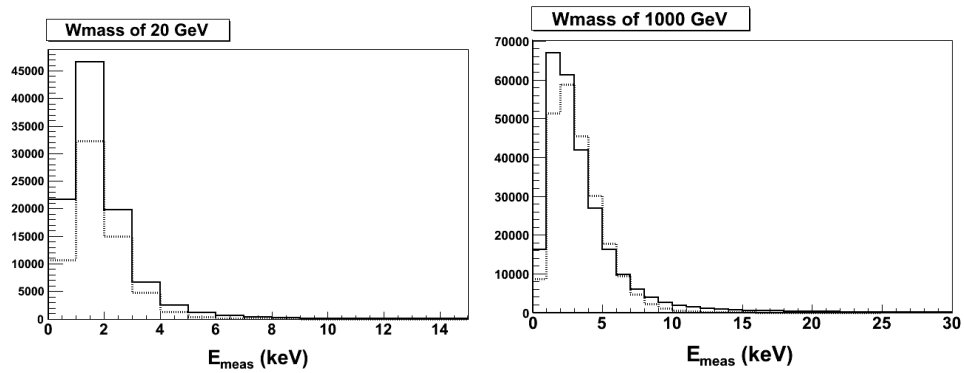

Figure 4.13: The expected E_{meas} distributions induced by WIMP–Cs SI scatterings with (the solid line) or without the channeling effect (the dashed line)

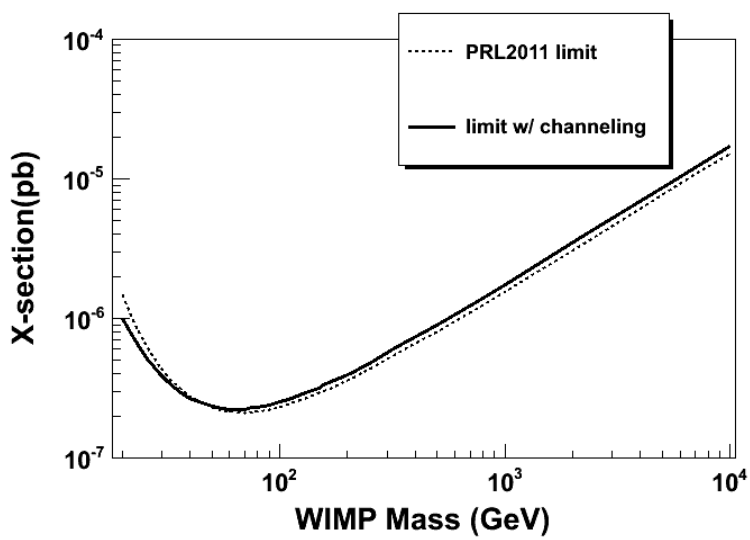

Figure 4.14: The comparison of the cross-section limits for the WIMP-nucleus SI scattering with or without channeling effect. PRL2011 limit curve is the recent publication in KIMS [40].

5 Conclusion

This study starts from claim by DAMA, that KIMS detector loses some nuclear recoil events subject to the channeling effect and their pulse shape discrimination (PSD) cut. The first goal of this study was to investigate how large the channeling fraction is in the CsI(Tl) crystal and what is the PSD value of those events. To find them, we have studied the channeling and blocking effect for recoil ions, the scintillation process from the energy deposition in the material to the emission of the scintillation, and several simulation programs to reproduce the channeling effect on the CsI(Tl) crystal by recoil ions. We also constructed an experimental apparatus to measure the channeling and blocking effect. Finally, we reproduce an E_{meas} spectra which fits the data well with consideration of the channeling effect. We estimate that the channeling effect in the CsI(Tl) crystal is under $\sim$ 3 %, which is unlike DAMA's claim, but in favor of N. Bozorgnia *et al.* [2]. We also quantify the channeling fraction in our experimental data. The results are $\sim$ 5 % for three different recoil energies, however, the multiple scattering and inelastic scattering events are also expected by $\sim$ 2 % in the simulation, so we should reduce this uncertainty in the future with higher statistics. In this study, we also notice that the nonproportionality of the scintillation yield for the low energy gamma and the possible PSD difference between the Compton electrons and gamma responses. These also should be investigated further to reduce the uncertainty for the quenching factor and PSD measurement.

By applying the reproduced E_{meas} in the simulation, we modify the expected E_{meas} spectrum induced by WIMP-nucleus scattering and estimate the modified cross-section limit. However, the channeling effect on the WIMP search produces no significant change. But from this study, we can understand CsI(Tl) scintillator as a detector for the WIMP search, and expect that

with further investigations, we can find a clue to explain the conflict between results in the WIMP search experiments with same or different detectors.

Bibliography

[1] D. S. Gemmell. Channeling and related effects in the motivation of charged particles through crystals. Rev. Mod. Phys. 46, 129, 1974.

[2] N. Bozorgnia *et al.* Channeling in direct dark matter detection iii : channeling fraction in csi crystals. JCAP 11, 029, 2010.

[3] M. D. Ziegler J. F. Ziegler, J. P. Biersack. Srim-the stopping power and range if ions in matter (website and textbook). http://www.srim.org, 2008.

[4] M. T. Robinson. Marlowe 15b. http://rsicc.ornl.gov/Default.aspx .

[5] DAMA collaboration R. Bernabei *et al.* Possible implications of the channeling effect in NaI(Tl) crystals. Eur. Phys. J. C53, 2, 205, 2008.

[6] KIMS collaboration J. H. Lee *et al.* Simulation and measurement of quenching and channeling effects in CsI(Tl) for dark matter search. IEEE Trans. nucl. sci. DOI: 10.1109/TNS.2012.2189019 , 2012.

[7] F. Zwicky. Republication of: The redshift of extragalactic nebulae. General Relativity and Gravitation 41, 207, 2008 English version of Helv. Phys. Acta 6, 110 (1933).

[8] V. C. Rubin K. W. Ford. Jr. Rotation of the andromeda nebula from a spectroscopic survey of emission regions. Astrophys. J159, 379, 1970.

[9] A. H. Broeils K. G. Begeman and R. H. Sanders. Extended rotation curves of spiral galaxies – dark halos and modified dynamics. Mon. Not. Roy. Astron. Soc. 249, 523, 1991.

[10] M. J. Jee *et al.* Discovery of a ringlike dark matter structure in the core of the galaxy cluster Cl 0024+17. Astrophys. J661, 728, 2007.

[11] M. Bradač. Dark matter : Revealing the inivisible with 2 cosmic supercolliders the "bullet cluster" 1E0657-56 and MACSJ0025-1222. Nucl. Phys. B(Proc. Suppl.)194, 17, 2009.

[12] H. S. Lee. *Dark Matter Search with CsI(Tl) Crystals.* PhD thesis, Seoul Natioanl University, 2007.

[13] S. C. Kim. *Dark Matter Search with 100 kg of CsI(Tl) Crystals.* PhD thesis, Seoul Natioanl University, 2011.

[14] Wilkinson Microwave Anisotropy Probe. http://map.gsfc.nasa.gov/.

[15] J. D. Lewin and P. F. Smith. Review of mathematics, numerical factors, and corrections for dark matter experiments based on elastic nuclear recoil. Astropart. Phys.6, 87, 1996.

[16] Moqbil S. Alenazi and Paolo Gondolo. Directional recoil rates for WIMP direct detection. Phys. Rev. D77,043532, 2008.

[17] Abhijit Bandyopadhyay and Debasish Majumdar. Diurnal and annual variations of directional detection rates of dark matter. Astrophys. J746,107, 2012.

[18] the XENON100 collaboration E. Aprile *et al.* Dark matter results from 100 live days of XENON100 data. Phys. Rev. Lett.107, 131302, 2011.

[19] The CDMS II collaboration Z. Ahmed *et al.* Dark matter search results from the CDMS II experiment. Science 327, 1619, 2010.

[20] DAMA/LIBRA collaboration R. Bernabei *et al.* New results from DAMA/LIBRA. Eur. Phys. J. C67,39, 2010.

[21] CoGeNT collaboration C. E. Aalseth *et al.* Search for an annual modulation in a p-type point contact germanium dark matter detector. Phys. Rev. Lett.107,141301, 2011.

[22] EDELWEISS collaboration E. Armengaud *et al.* First results of the EDELWEISS-II WIMP search using a 4-kg array of cryogenic germanium detectors with interleaved electrodes. Phys. Lett. B702,329, 2011.

[23] G. Angloher *et al.* Results from 730 kg days of the CRESST-II dark matter search. Eur. Phys. J. C72,1971, 2012.

[24] E. Won *et al.* A test of CsI(Tl) crystal for the dark matter search. Nucl. Phys. B(Proc. Suppl.) 78, 449, 1999.

[25] H. J. Kim et al. Test of CsI(Tl) crystals for the dark matter search. Nucl. Instrum. Meth. A 457, 471, 2001.

[26] H. S. Lee et al. First limit on wimp cross section with low background CsI(Tl) crystal detector. Phys. Lett. B 633, 201, 2006.

[27] T. Y. Kim et al. Study of the internal background of CsI(Tl) crystal detectors for dark matter search. Nucl. Instrum. Meth. A 500, 337, 2003.

[28] H. S. Lee et al. Development of low-background CsI(Tl) crystals for wimp search. Nucl. Instrum. Meth. A 571, 644, 2007.

[29] Y. D. Kim et al. Measurements of cesium radioisotopes in cesium compounds. J. Kor. Phys. Soc. 40, 520, 2002.

[30] Y. D. Kim et al. Inhibition of ^{137}cs contamination in cesium iodide. Nucl. Instrum. Meth. A 552, 456, 2005.

[31] R. Bernabei et al. Search for wimp annual modulation signature: results from dama/nai-3 and dama/nai-4 and the global combined analysis. Phys. Lett. B 480, 23, 2000.

[32] KIMS collaboration H. S. Lee *et al.* Limits on interactions between Weakly Interacting Massive Particles and nucleaons obtained with CsI(Tl) crystal detectors. Phys. Rev. Lett. 99, 091301, 2007.

[33] WCU center for high energy physics. `http://q2c.snu.ac.kr`.

[34] KIMS collaboration J. H. Choi *et al. in preparation.*

[35] M. J. Lee et al. Radon environment in the korea invisible mass search experiment and its measurement. J. Kor. Phys. Soc. 53, 4, 713, 2011.

[36] Y. F. Zhu *et al.* Measurement of the intrinsic radiopurity of 137cs/235u/238u/232th in csi(tl) crystal scintillators. Nucl. Instrum. Meth. A 557, 490, 2006.

[37] KIMS collaboration S. C. Kim *et al.* Low energy fast events from radon progenies at the surface of a CsI(Tl) scintillator. Astropart. Phys. 35, 781, 2012.

[38] A. Caldwell et al. Bat - the bayesian analysis toolkit. Comp. Phys. Comm 180, 2197, 2009.

[39] Rene Brun et al. Root - an object-oriented data analysis framework. http://root.cern.ch.

[40] KIMS collaboration S. C. Kim *et al.* New limits on interactions between weakly interacting massive particles and nucleons obtained with CsI(Tl) crystal detectors. Phys. Rev. Lett. 108,181301, 2012.

[41] Geant4. http://geant4.cern.ch.

[42] KIMS collaboration J. K. Lee *et al. in preparation.*

[43] KIMS collaboration S. S. Myung *et al. accepted for the publication.*

[44] N. Bozorgnia *et al.* Channeling in direct dark matter detection i : channeling fraction in nai crystals. JCAP 11, 019, 2010.

[45] H. J. Kim S. K. Kim and Y. D. Kim. Scintillator-based detectors for dark matter searches i. New J. Phys. 12, 075003, 2010.

[46] Z. Wang *et al.* Computer simulation of electron thermalization in csi and csi(tl). J. Appl. Phys. 110, 064903 , 2011.

[47] V. Nagirnyi *et al.* Peculiarities of the triplet relaxed excited-state structure and luminescence of a csi:tl crystal. J. Phys. : Condens. Matter 7, 3637, 1995.

[48] R. T. Williams *et al.* Excitation density, diffusion-drift, and proportionality in scintillators. Phys. Status Solidi B 248, 426, 2011.

[49] V. Yakovlev *et al.* Time-resolved optical spectroscopy of csi(tl) crystals by pulsed electron beam irradiation. J. Luminescnece 129, 790, 2009.

[50] L. Trefilova *et al.* Recombination luminescence of csi(tl) under electron pulse irradiation. Rad. Meas. 45, 328, 2010.

[51] S. A. Chernov *et al.* Photo- and thermo-stimulated luminescence of csi-tl crystal after uv light irradiation at 80 k. Rad. Eff. and Def. in Solids 143, 345 , 1998.

[52] Piotr A. Rodnyi. *Physical processes in inorganic scintillators.* CRC Press LLC, 1997.

[53] J. H. Lee. Measurement of photoluminescence with CsI(Tl) crystal for dark matter search, Master thesis, 2006.

[54] KIMS collaboration S. H. Lee *et al.* Measurement of photoluminescence with CsI(Tl) crystal for dark matter search. *in preparation.*

[55] T. Tsujimoto *et al.* Hydrostatic pressure effects on the free and self-trapped exciton states in csi. Phys. Rev. B 54, 16579 , 1996.

[56] R. B. Murray and A. Meyer. Scintillation response of activated inorgarnic crystals to various charged particles. Phys. Rev., 122, 3, 815, 1961.

[57] J. B. Birks. *The theory and practice of scintillation counting.* Peragamon press, 1964.

[58] R. Gwin and R. B. Murray. Scintillation process in CsI(Tl) . i. comparison with activator saturation model. Phys. Rev., 131, 2, 501, 1963.

[59] estar. http://physics.nist.gov/PhysRefData/Star/Text/ESTAR.html.

[60] R. Behrisch. *Topics in applied physics - Sputtering by particle bombardment I.* Springer - Verlag, 1981.

[61] M. T. Robinson. The binary collision approximation : Background and introduction. Rad. Eff. and Def. in Solids130, 1, 3, 2010.

[62] A. Hitachi. Properties of liquid xenon scintillation for dark matter searches. Astropart. Phys.24, 247, 2005.

[63] V. I. Tretyak. Semi-empirical calculation of quenching factors for ions in scintillators. Astropart. Phys.33, 40, 2010.

[64] A. V. Sharko and A. A. Botaki. Debye temperature of alkali halide crystals. Russ. Phys. J. 14, 3, 360, 1973.

[65] Y. Marcus. The cohesive energy of molten salts and its density. J. Chem. Thermodynamics, 42, 66, 2010.

[66] Halite-NaCl. WolfWikis.

[67] G. R. Piercy *et al.* Experimental evidence for the increase of heavy ion ranges by channeling in crystalline structure. Phys. Rev. Lett.10, 399, 1963.

[68] G. Hobler *et al.* Boron channeling implantations in silicon : Modeling of electronic stopping and damage accumulation. J. Appl. Phys.77, 3697, 1995.

[69] G. Hobler. Critical angles and low energy limits to ion channeling in silicon. Rad. Eff. and Def. in Solids139, 21, 1996.

[70] S. M. Hogg *et al.* Channeling of low energy heavy ions : Er in si111. Appl. Phys. Lett80, 4363, 2002.

[71] TEXONO collaboration Y. F. Zhu *et al.* Measurement of the intrinsic radiopurity of ^{137}cs/^{235}u/^{238}u/^{232}th in csi(tl) crystal scintillators. Nucl. Instrum. Meth. A557, 490, 2006.

[72] KIMS collaboration T. Y. Kim *et al.* Study of the internal background of csi(tl) crystal detectors for dark matter search. Nucl. Instrum. Meth. A500, 337, 2003.

[73] TEXONO collaboration M. Z. Wang *et al.* Nuclear recoil measurement in csi(tl) crystal for cold dark matter detection. Phys. Lett. B536, 203, 2002.

[74] S. Pécourt *et al.* Calibration of a csi(tl) crystal with nuclear recoils and pulse shape measurements for dark matter detection. Astropart. Phys.11, 457, 1999.

[75] V. A. Kudryavtsev *et al.* Csi(tl) for wimp dark matter searches. Nucl. Instrum. Meth. A456, 272, 2001.

[76] KIMS collaboration H. Park *et al.* Neutron beam test of csi crystal for dark matter search. Nucl. Instrum. Meth. A491, 460, 2002.

[77] H. Chagani *et al.* Measurement of the quenching factor of na recoils in nai(tl). JINST 3, P06003, 2008.

[78] D. R. Tovey *et al.* Measurement of scintillation efficiencies and pulse-shapes for nuclear recoils in nai(tl) and caf_2(eu) at low energies for dark matter experiments. Phys. Lett. B433, 150, 1998.

[79] G. Gerbier *et al.* Pulse shape discrimination and dark matter search with nai(tl) scintillator. Astropart. Phys.11, 287, 1999.

[80] N. J. C. Spooner *et al.* The scintillation efficiency of sodium and iodine recoils in a nai(tl) detector for dark matter searches. Phys. Lett. B321, 156, 1994.

[81] W. Mengesha *et al.* Light yield nonproportionality of CsI(Tl) , csi(na), and yap. IEEE Trans. nucl. sci. 45, 456, 1998.

[82] KIMS collaboration K. W. Kim *et al. in preparation.*

[83] Hamamatsu. http://www.hamamatsu.com/.

[84] Scintillator brochuers. http://www.detectors.saint-gobain.com/Liquid-Scintillator.aspx.